

5-1-1997


Coastal Circulations Driven by River Outflow

Shuliang Zhang

Nova Southeastern University Oceanographic Center, shuliang_zhang@yahoo.com

This document is a product of extensive research conducted at the Nova Southeastern University [Halmos College of Natural Sciences and Oceanography](#). For more information on research and degree programs at the NSU Halmos College of Natural Sciences and Oceanography, please click [here](#).

Follow this and additional works at: http://nsuworks.nova.edu/occ_stuetd

 Part of the [Marine Biology Commons](#), and the [Oceanography and Atmospheric Sciences and Meteorology Commons](#)

Share Feedback About This Item

NSUWorks Citation

Shuliang Zhang. 1997. *Coastal Circulations Driven by River Outflow*. Doctoral dissertation. Nova Southeastern University. Retrieved from NSUWorks, Oceanographic Center. (45)
http://nsuworks.nova.edu/occ_stuetd/45.

This Dissertation is brought to you by the HCNSO Student Work at NSUWorks. It has been accepted for inclusion in Theses and Dissertations by an authorized administrator of NSUWorks. For more information, please contact nsuworks@nova.edu.

COASTAL CIRCULATIONS DRIVEN BY RIVER
OUTFLOW

BY
SHULIANG ZHANG

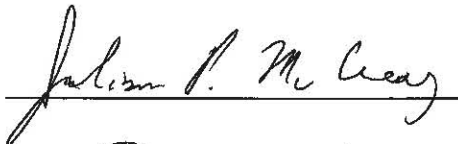
A DISSERTATION SUBMITTED IN PARTIAL FULFILLMENT OF THE
REQUIREMENTS FOR THE DEGREE OF
DOCTOR OF PHILOSOPHY
IN
OCEANOGRAPHY

NOVA SOUTHEASTERN UNIVERSITY


May, 1997

DOCTORAL DISSERTATION
OF
SHULIANG ZHANG


APPROVED
BY
DISSERTATION COMMITTEE:


Julian P. McCreary, Jr., Chairman


Dr. Richard E. Dodge


Dr. Barry A. Klinger


Dr. Donald B. Olson


Dr. Claes G. H. Rooth


Dr. Russell L. Snyder

NOVA SOUTHEASTERN UNIVERSITY

May, 1997

Table of Contents

Table of Contents	iii
List of Tables	v
List of Figures	vi
Acknowledgements	viii
Vita	ix
Publications	ix
Abstract	x
CHAPTER 1: INTRODUCTION	1
1.1 Observational background	1
1.2 Theoretical background	6
1.2.1 Linear, constant-density, $1\frac{1}{2}$ -layer models	6
1.2.2 Nonlinear, constant-density, $1\frac{1}{2}$ -layer models	9
1.2.3 General Circulation Models	10
1.3 Present research	10
CHAPTER 2: THE OCEAN MODELS	12
2.1 Governing equations	12
2.1.1 Nonlinear, $1\frac{1}{2}$ -layer model	12
2.1.2 Linearized, $1\frac{1}{2}$ -layer model	16
2.1.3 Nonlinear, $2\frac{1}{2}$ -layer model	17
2.2 Basin and boundary conditions	18
2.3 Numerical methods and parameter choices	19
CHAPTER 3: GEOSTROPHIC ADJUSTMENT	23
3.1 Solutions to the linearized, $1\frac{1}{2}$ -layer model	23
3.1.1 Numerical results	23
3.1.2 Analytical results	24
3.1.3 Comparison with constant-density model	27
3.2 Solutions to the nonlinear, $1\frac{1}{2}$ -layer model	28
3.2.1 Numerical results	28
3.2.2 Analytic results	28
3.2.3 Comparison with constant-density model	31

3.3	Solutions with a slanted front	32
3.3.1	Analytical solution	32
3.3.2	Comparison with the variable-density, $1\frac{1}{2}$ -layer model	33
CHAPTER 4: SOLUTIONS TO THE $1\frac{1}{2}$-LAYER MODEL		38
4.1	Low- R_o solutions	38
4.1.1	Typical solutions	38
4.1.2	Coastal mode and gyre mode	44
4.1.3	Analytic solutions	54
4.1.4	Parameter variation (L and c curves)	63
4.1.5	Inferences from the slanted-front solution	66
4.2	High- R_o solutions	67
4.2.1	Typical solutions	67
4.2.2	Dynamics	67
4.2.3	Jet angle	72
4.3	Solutions with entrainment	78
CHAPTER 5: SOLUTIONS TO THE $2\frac{1}{2}$-LAYER MODEL		86
5.1	Effect of lower-layer inflow	87
5.2	Effect of a background current	98
5.3	Effect of wind forcing	101
CHAPTER 6: SUMMARY AND DISCUSSION		119
APPENDIX A: SOLUTION WITH A SLANTED FRONT		123
APPENDIX B: VERTICAL MODES		125

List of Tables

Table		Page
1	A list of parameter values used in all runs unless specified otherwise	22
2	A list of table for the parameter values used in Figure 18	82

List of Figures

Figure	Page
1 Typical salinity distributions along the Delaware coast	3
2 Observed surface salinity distribution during September and January, 1986, near the Changjiang River mouth	5
3 Sediment distribution in the Gulf of Bohai in the East China Sea	8
4 A schematic diagram of the variable-density, $1\frac{1}{2}$ -layer model	14
5 Solutions of y -independent, geostrophic adjustment for the linear, $1\frac{1}{2}$ -layer model	26
6 Solutions of y -independent, geostrophic adjustment for the nonlinear, $1\frac{1}{2}$ -layer model	30
7a Comparison of solutions of y -independent, geostrophic adjustment for the slanted-front model with those for the nonlinear, variable-density model	35
7b Comparison of solutions of y -independent, geostrophic adjustment for the slanted-front model with those for the nonlinear, variable-density model	37
8 A typical low- R_o solution for the nonlinear, $1\frac{1}{2}$ -layer model	41
9 Latitude-time plots of the coastal depth-integrated pressure $\mathcal{P}_1(0, y)$ and salinity $S_1(0, y)$ for the solution in Figure 8	43
10 Solutions to the linear, variable-density, $1\frac{1}{2}$ -layer model	46
11a Solutions illustrating the coastal and gyre modes	50
11b Solutions obtained by the quasi-geostrophic approximation	53
12 Schematic diagram of the analytic solution driven by river outflow	56
13 Offshore structures of outflow-driven solutions for the analytic, linear and nonlinear models, and for an analytic solution resulting from geostrophic adjustment of a y -independent coastal front	61
14 Plume width L and nose propagation speed c as a function of non-dimensional parameters ϕ for different values of γ	65
15 A sequence of high- R_o solutions with different values of M_r in the nonlinear, $1\frac{1}{2}$ -layer model	69

Figure	Page
16 A sequence of high- R_o solutions with different values of H_1 in the nonlinear, $1\frac{1}{2}$ -layer model	71
17 High-transport solutions to the nonlinear, $1\frac{1}{2}$ -layer model when the momentum-advection terms are dropped	74
18 Comparison of jet angle obtained analytically from equation (63), α_a , with the angle obtained in the corresponding numerical model, α_n	77
19 High- R_o solutions when Y_{\pm} are used for the outflow structures	80
20 Solutions to the nonlinear, $1\frac{1}{2}$ -layer model with entrainment	84
21 Solution to the nonlinear, $2\frac{1}{2}$ -layer model with lower-layer inflow	89
22a Solution to the linear, $2\frac{1}{2}$ -layer model with lower-layer inflow	91
22b Across-shore structure of alongshore velocities in the downstream region in the solution to the linear, $2\frac{1}{2}$ -layer model with lower-layer inflow	95
22c Across-shore structure of alongshore velocities in the upstream region in the solution to the linear, $2\frac{1}{2}$ -layer model with lower-layer inflow	97
23 Solutions to the nonlinear, $2\frac{1}{2}$ -layer model when there is a downstream background current	100
24 Some properties of solutions to the nonlinear, $2\frac{1}{2}$ -layer model when there is a downstream background current	103
25 Latitude-time plots of coastal salinity $S_1(0, y)$ in solutions to the nonlinear, $2\frac{1}{2}$ -layer model with a downstream background current	105
26 Solution to the nonlinear, $2\frac{1}{2}$ -layer model before the onset of alongshore winds	108
27 Across-shore structure of a solution to the nonlinear, $2\frac{1}{2}$ -layer model under the influence of an upwelling-favorable wind	111
28 Solution to the nonlinear, $2\frac{1}{2}$ -layer model under the influence of an upwelling-favorable wind	113
29 Across-shore structure of a solution to the nonlinear, $2\frac{1}{2}$ -layer model under the influence of a downwelling-favorable wind	116
30 Solution to the nonlinear, $2\frac{1}{2}$ -layer model under the influence of a downwelling-favorable wind	118

Acknowledgements

I am so grateful to my major professor, Julian P. McCreary, for his constant encouragement and guidance. The instillation of his rigorous attitude of scientific research will deeply affect the rest of my career. Discussions with committee members Claes Rooth and Don Olson were especially helpful. Other committee members, Barry Klinger, Russ Snyder and Dick Dodge, read earlier versions of my dissertation, and provided many suggestions for its improvement. Thanks also go to Kevin Kohler for his programming assistance.

I would like to express gratitude to all my teachers and friends in China for their help during my education, and to all my family members, especially my wife, for their encouragement, patience and understanding.

This work was sponsored by ONR Grant N00014-90-J-1054 and by NSF Grants OCE 92-03916 and OCE-95-03379 awarded to Julian P. McCreary. Initial work was carried out when Julian P. McCreary visited Satish Shetye of National Institute of Oceanography in Goa, India.

Vita

Dec. 19, 1964: Born in Shandong, P. R. China

1980–1984: B. S., Ocean University of Qingdao, Qingdao, P. R. China

1984–1986: Teaching assistant, Ocean University of Qingdao, Qingdao, P. R. China

1986–1989: M. S., Ocean University of Qingdao, Qingdao, P. R. China

1989–1990: Teaching assistant, Ocean University of Qingdao, Qingdao, P. R. China

1991–1997: Ph. D. student, Oceanographic Center, Nova Southeastern University, Dania, Florida

May, 1997: Doctor of Philosophy, Nova Southeastern University, Dania, Florida

Publications

“Numerical analysis of strong wind field over the Gulf of Bohai in the East China Sea during 40 cold front passages from 1956 through 1989” (with Faxiu Zhou). *Technical report of Corporation of Bohai Oil Mining*, 1990. (In Chinese.)

“A model for diagnosing the effect of topography on meso-scale wind” (with Faxiu Zhou), *Transactions of Oceanology and Limnology*, 1991, **22**, 487–497. (In Chinese.)

“Coastal circulation driven by river outflow in a variable-density $1\frac{1}{2}$ -layer model” (with Julian P. McCreary and Satish R. Shetye). *J. Geophys. Res.* (Accepted.)

Abstract

Variable-density, $1\frac{1}{2}$ - and $2\frac{1}{2}$ -layer models are used to examine the behavior of plumes resulting from a fresher outflow of transport M_r and salinity S_r into a pre-existing oceanic layer of initial thickness H_1 and salinity S_1^* . It is found that the plumes exhibit a variety of features depending on conditions of the outflow, the situation of the ambient ocean, and external forcing. Perhaps the most interesting feature is that the plume can flow along the upstream (to the left of the river mouth, looking seaward in the northern hemisphere) coast by itself, and the research discussed here is focused on this topic.

To illustrate how density variations associated with river plumes drive circulations, several solutions of geostrophic adjustment to an initially-imposed, y -independent density front are investigated. In these solutions, a frontally-trapped alongfront geostrophic current with the fresher water to its right (facing in the current direction) is always generated in response to the initial pressure gradient across the density front. This density-driven geostrophic current is dynamically similar to that resulting from initial disturbances in layer thickness h (equivalently, potential vorticity $q = f/h$) in constant-density models, with low salinity (density) in the variable-density model being analogous to the low q in the constant-density model.

Solutions to the $1\frac{1}{2}$ -layer model driven by river outflow are fundamentally different in low- R_o (Rossby number) and high- R_o regimes. In the low- R_o case, plumes advance along both upstream and downstream coasts. If M_r is less than a critical value M_{cr} (determined by $\Delta S = S_1^* - S_r$ and H_1), plumes are coastally-trapped and *all* the river water first flows upstream, with some of it, together with some salty water, reversing direction near the plume nose to flow along the offshore front, this return flow passes the river mouth and continues to flow along the downstream (to the right of the river mouth) coast. When $M_r > M_{cr}$, the plumes expand offshore indefinitely, and some river water must flow downstream directly.

The evolution of the river plume for the low- R_o solutions can be understood in terms of two distinct flow patterns. One is a downstream coastal current ("coastal mode") directly forced by the river transport; it is dynamically similar to the response in a linear, constant-density, $1\frac{1}{2}$ -layer model, and is responsible for the downstream motion. The other is an

anticyclonic circulation ("gyre mode") due to geostrophic adjustment of the river plume; the coastal current of this circulation is responsible for the upstream motion. Analytical solutions illustrate that geostrophic adjustment along the offshore density front generates the return flow and that Kelvin waves originating from the plume nose cause the upstream flow. They also allow the plume width L and the upstream nose speed c of the nose to be determined as a function of model parameters.

For the high- R_o solutions, river water flows directly offshore in a narrow jet. The angle in which the jet emerges from the river mouth is found to depend on several non-dimensional parameters. Inclusion of entrainment significantly inhibits the upstream plume propagation, and makes it difficult to distinguish low- R_o and high- R_o solutions.

In solutions to the $2\frac{1}{2}$ -layer model, the upper-layer circulation is not significantly different from that in their $1\frac{1}{2}$ -layer counterparts. A pre-existing downstream coastal current significantly weakens upstream plume propagation; indeed, the upstream advance can be completely stopped if the background current is strong enough. Ekman flow and along-shore currents induced by upwelling-favorable winds push the plume offshore and upstream, whereas downwelling-favorable winds result in a coastally trapped plume that is advected downstream.

CHAPTER 1

INTRODUCTION

1.1 Observational background

In the northern hemisphere, river water typically bends to the right (facing seaward) as it flows into the ocean, forming a shallow plume along the right-hand coast. (For convenience, the terms "upstream" and "downstream" are introduced to indicate directions oriented toward the left-hand and right-hand coasts, respectively.) Well-documented examples of this type of circulation are the outflows from the Delaware Bay (Figure 1; Münchow and Garvine, 1993) and the Chesapeake Bay (Boicourt, 1981). In contrast, salinity distributions offshore from the mouths of the Changjiang River (Figure 2; also known as the Yangtze River) and the Ganges River indicate that some river water flows directly offshore during the summer when the discharge is high (Beardsley *et al.*, 1983; Wang, 1988; Murty *et al.*, 1992; Shetye *et al.*, 1993). There are also indications that river water can bend to the left to flow along the upstream coast. A dramatic leftward flow of the Mississippi River outflow occurred after the major flood in 1993, with part of the plume flowing eastward along the shelf and eventually moving down the west coast of Florida (Walker *et al.*, 1994); according to the authors, the eastward flow was externally forced by abnormal westerly wind and by a northward intrusion of the Loop current. In addition, the presence of coastally trapped plumes just north of the Yangtze River mouth are suggested by salinity (Figure 8 of Beardsley *et al.*, 1983) and suspended sediment (Figure 1 of Cannon *et al.*, 1983). Similarly, a leftward bending of the Yellow River plume can be inferred from the accumulation of clay mud in the sediments to

Figure 1: Typical salinity distributions along the Delaware coast, showing surface salinity (upper panel) and a vertical section across the shelf (lower panel) at the location indicated by the arrow in the upper panel. The salinity distributions in the upper panel suggest that most of the fresher water bends to the right as it exits the Bay mouth. (After Münchow and Garvine, 1993.)

05-25-1989

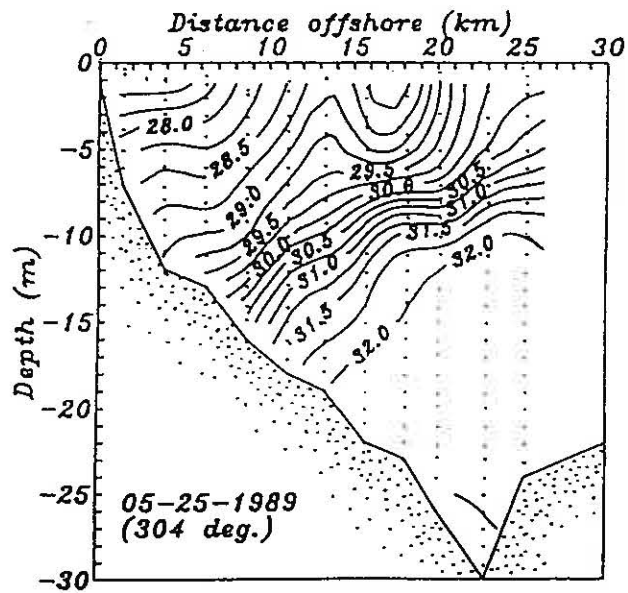
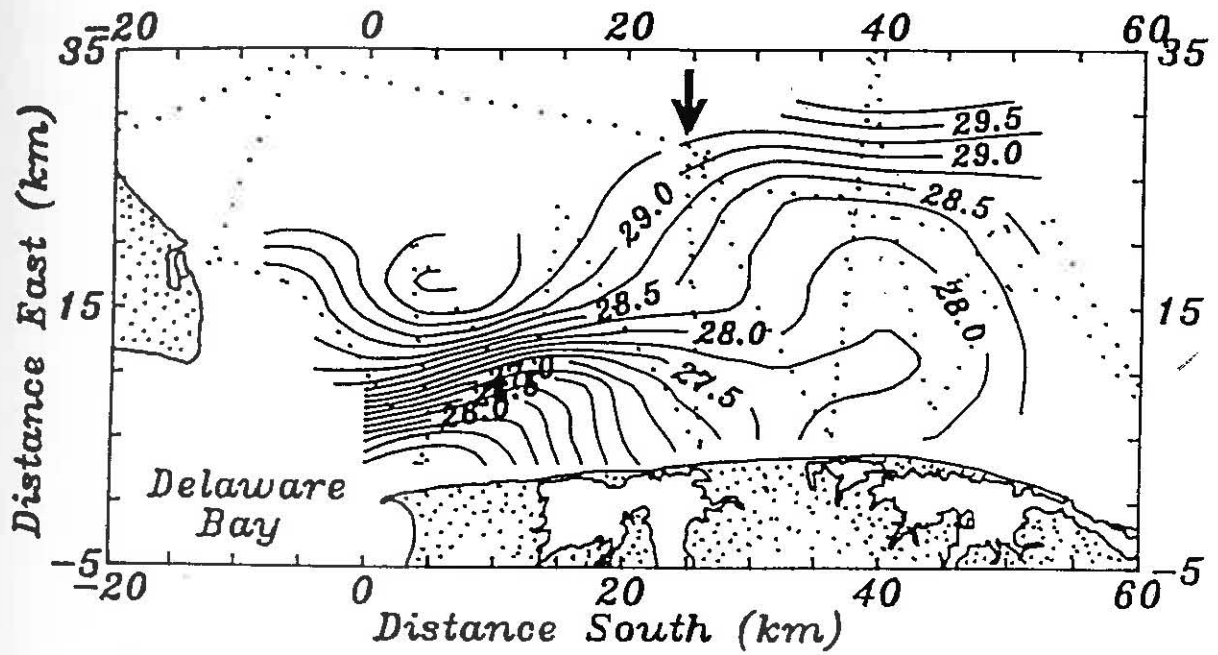
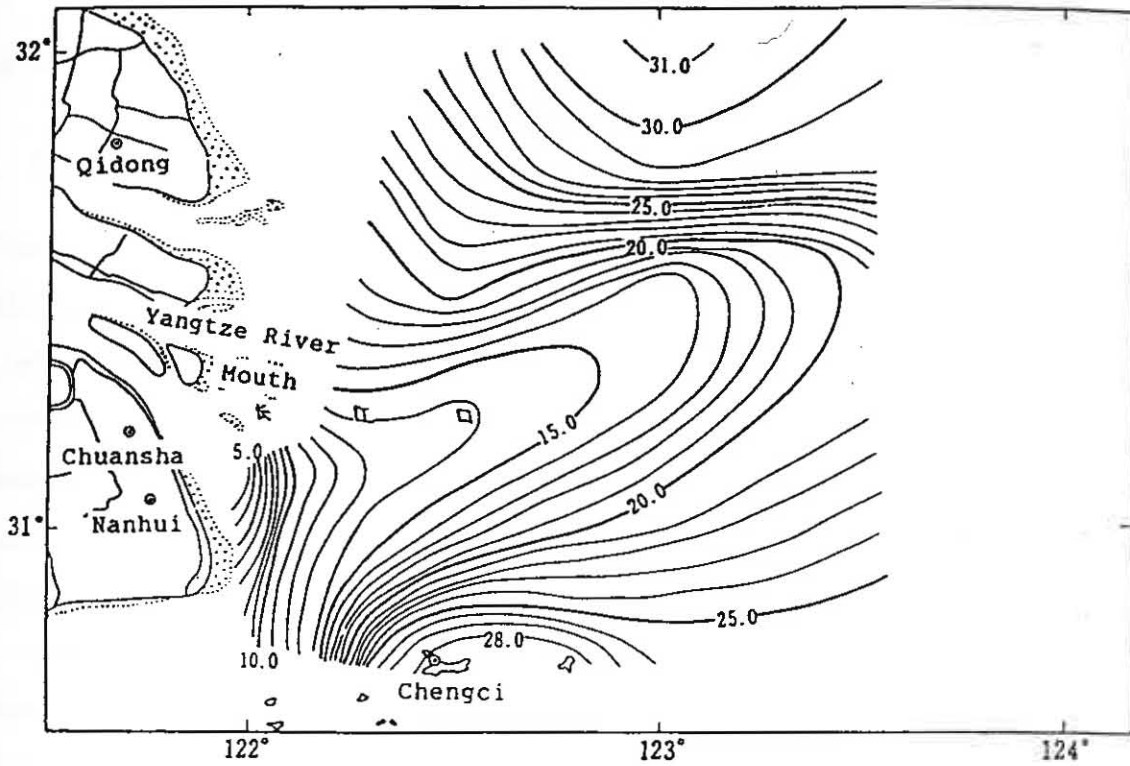
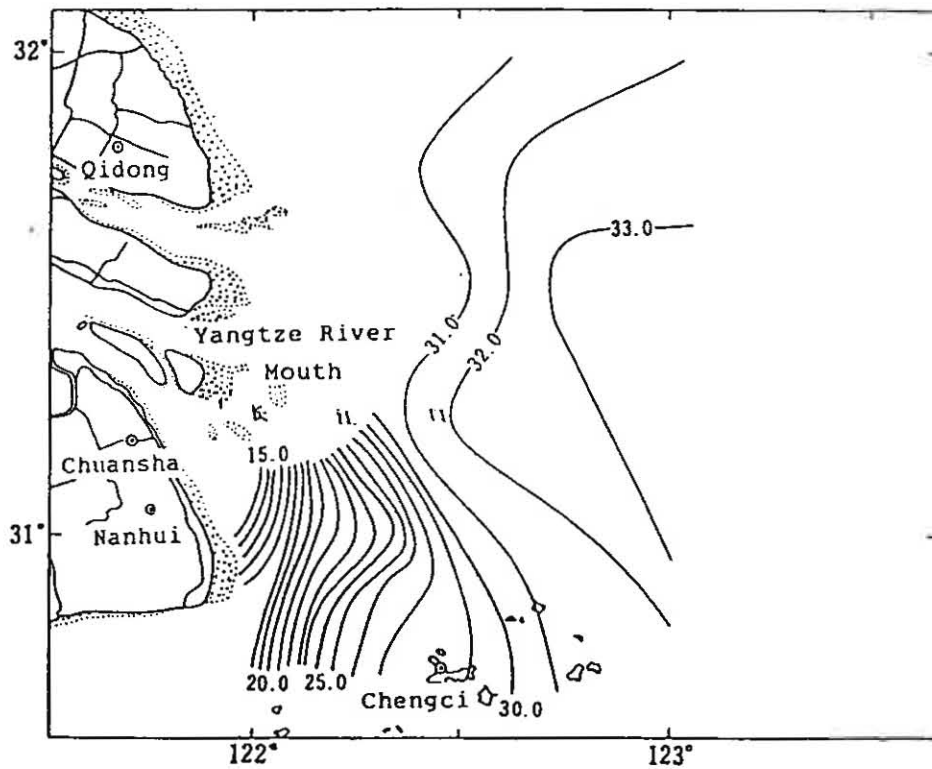


Figure 2: Observed surface salinity distribution during September (upper panel) and January (lower panel), 1986, near the Changjiang River mouth. There is a prominent low-salinity tongue extending to the northeast in the summer. The salinity distribution in the winter suggests that all the river water flows downstream in a narrow band along the coast. (After Wang, 1988.)

September 1986



January 1986



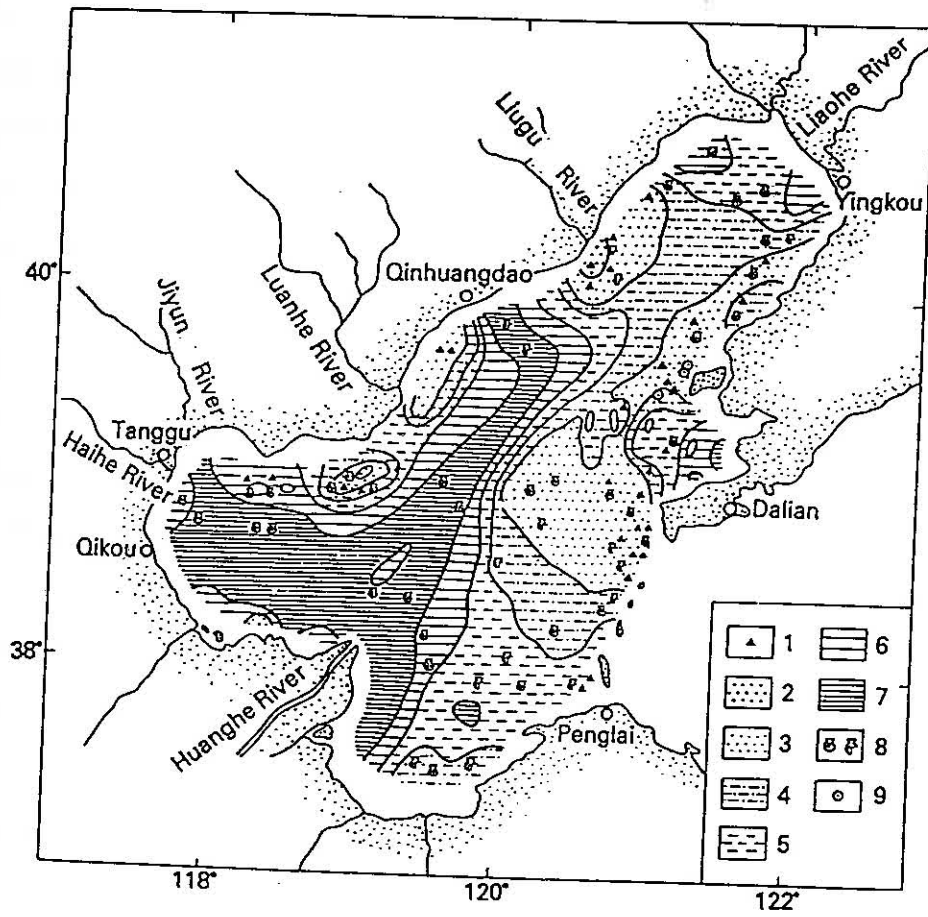
the left of the river mouth (Figure 3; Qin *et al.*, 1990).

1.2 Theoretical background

There are already a considerable number of modeling studies that consider the coastal circulations driven by river outflow. Here, results from those studies that are most relevant to this research are briefly summarized. They are arranged, as much as possible, in a hierarchy that varies from dynamically simple to sophisticated systems. There are other studies, not reviewed in the following, that examine potentially important processes not present in this research. These are, for example, models in which bottom topography and background currents are essential dynamical factors (*e.g.*, Beardsley and Hart, 1981; Zhang *et al.*, 1987), that examine effects due to external forcing by the winds (Chao, 1988b), or that require supercritical flows (Froude number $F_r > 1$), that is, currents with speeds greater than the gravity-wave speed (*e.g.*, Garvine, 1987; O'Donnell, 1990). The flows in this research are all subcritical ($F_r < 1$).

1.2.1 Linear, constant-density, $1\frac{1}{2}$ -layer models: Perhaps the simplest ocean model for studying river outflow is a linear, $1\frac{1}{2}$ -layer, constant-density system in which river water with the *same density* as that of the model's active upper layer is introduced via a side-wall boundary condition. Such a system has been considered by Minato (1983). In his solutions, a coastal current is generated in response to the outflow that flows almost entirely along the downstream coast. When the river mouth is smaller than a Rossby radius of deformation, a small amount of water first moves somewhat upstream before reversing to flow downstream. The downstream coastal current is created by the radiation of coastal Kelvin waves that are excited by the high pressure associated with the geostrophically balanced outflow. The upstream component is generated by the radiation of gravity waves, since it does not occur in a model that assumes alongshore geostrophy. Although this model is too simple to have much realism, it does reveal one basic dynamical feature of all river-outflow problems: the important role of coastal Kelvin waves in establishing the downstream coastal current. Ikeda (1984) and Kundu and McCreary (1986) obtained analogous solutions, the latter using a continuously stratified linear model.

Figure 3: Sediment distribution in the Gulf of Bohai in the East China Sea. A large patch of clay mud, originating from the Yellow (Huanghe) River mouth located at the lower left corner, suggests that the river water flow to the left. (After Qin *et al.*, 1990.)



1. gravel
2. medium sand
3. fine sand

4. coarse-silt
5. fine silty mud
6. silty clayey mud

7. clayey mu
8. shell
9. ferro-manganese nodules

1.2.2 Nonlinear, constant-density, $1\frac{1}{2}$ -layer models: Kubokawa (1991) utilized a nonlinear, quasi-geostrophic, constant-density, $1\frac{1}{2}$ -layer model to study the behavior of outflow from a sea strait. The outflow, with a total transport M_r , generally consisted of two pieces that differ in the values of potential vorticity, q . The value of q for the left-hand was $q = 0$ (relative to the potential vorticity of the ambient sea water), whereas it was $q = P < 0$ for the right-hand piece. As in the linear model just discussed, the density of the outflow was the same as that of the water in the oceanic layer.

In contrast to the linear case, Kubokawa's nonlinear solutions depended crucially on the structure of q across the sea strait and the value of M_r . When the ratio of the transport of $q = P$ water to the total transport of the outflow, φ , was less than some critical value, φ_{cr} (determined by the total transport M_r and P), a steady-state solution developed in which *all* the $q = P$ water flowed downstream in a coastal current bounded by an offshore front of finite width. When $\varphi_{cr} < \varphi < 1$, an anticyclonic gyre developed offshore from the mouth of the sea strait. When $\varphi = 1$, so that all the outflow was $q = P$ water, some water always flowed upstream regardless of the value of M_r . In fact, *all* the outflow turned to flow upstream for values of M_r small enough for the properly non-dimensionalized parameter, $-P/M_r$, to be greater than 1. [These results were duplicated in a constant-density version of our numerical model, equations (1) below, that conserved both energy and enstrophy (Arakawa, 1981).] The tendency of water with low potential vorticity to concentrate along the upstream coast was also reported in Nof (1978) and Hermann *et al.* (1989).

Kubokawa's specification of a piecewise distribution of q for the outflow greatly simplified the calculation and analysis of his solution. With this choice, the evolution of the $q = P$ water was determined by the advection of the front between the $q = P$ and $q = 0$ waters (*i.e.*, by contour dynamics method). Velocities that advect the front can be viewed as consisting of two parts. The first part is a downstream coastal current established by the radiation of coastal Kelvin wave in response to the onset of the outflow, essentially the same response as in Minato's solution. The second part is an anti-cyclonic circulation associated with the potential vorticity anomaly of the $q = P$ water. Kubokawa focused his attention on solutions without upstream propagation of $q = P$ water. He only commented on the upstream propagation in his $\varphi = 1$ solutions, stating that it was due to advection by an

“image vortex,” since in this case the solution can not separate from the coast.

1.2.3 General Circulation Models: Nonlinear, general circulation models (GCMs) have been used to study river plumes in a number of studies (Chao and Boicourt, 1986; Chao, 1988a; Chapman and Lentz, 1994; Kourafalou *et al.*, 1996). All these models are driven by an input of river water with a density less than that of the sea water. They can have either a flat bottom or a sloping shelf. The Chapman and Lentz (1994) model is unique in that the momentum-advection terms are neglected.

Solutions to the GCMs generally produce a downstream coastal current, an anticyclonic gyre near the river mouth, and also some upstream movement of river water. For example, in a typical test run of the Kourafalou *et al.* (1996) model without bottom topography, the model responded to the outflow by generating first a downstream coastal current, then an offshore expansion and upstream advection of river water, and finally unstable waves on the downstream flow.

Because of their complexity, it is difficult to understand the dynamics of the circulations in the GCM solutions. However, a comparison among the various solutions provides some information about the parameters that control aspects of the solutions. In Chapman and Lentz's (1994) solutions, for example, there is never an offshore expansion of the plume near the river mouth, suggesting that momentum advection (neglected in their model) plays a crucial role in this expansion. In addition, the upstream motion in this model is sensitive to the horizontal gradient of density, suggesting that density advection is responsible for the upstream movement.

1.3 Present research

The goal of this research is to understand the dynamics that determine the response of the coastal ocean to river outflow. In particular, under what conditions do river plumes move downstream, upstream or expand offshore? Since there is almost no work that explicitly discusses the dynamics of upstream movement, a large part of the thesis work is focused on this issue.

The ocean models used are all *variable-density*, $1\frac{1}{2}$ -layer and $2\frac{1}{2}$ -layer systems in which

density is allowed to vary horizontally within each active layer. Thus, in contrast to the constant-density layer models discussed in Sections 1.2.1 and 1.2.2, these models *can* simulate the outflow of river water that is fresher than the ocean. Such systems emerged out of efforts to include entrainment and thermodynamics in models of the surface mixed layer (Schopf and Cane, 1983; de Szoeke and Richman, 1984), and they are now being imbedded in GCMs (Chen *et al.*, 1994; Schopf and Loughe, 1995; Bleck *et al.*, 1989). Their advantage is dynamical simplicity, which allows processes at work in them to be readily diagnosed. At the same time, they are dynamically sophisticated enough to simulate realistically oceanographic phenomena that range from large-scale circulations (*e.g.*, Chen *et al.*, 1993) to small-scale frontal instabilities (Fukamachi *et al.*, 1995). In the present context, their major limitation is that, since the deep ocean is assumed inert, effects due to shelf topography are explicitly excluded. On the other hand, the processes that determine the basic properties of solutions (alongfront geostrophic adjustment and radiation of coastal waves) in this study are also present in shelf models, and therefore they will provide insights into the dynamics of these more complex systems.

The remainder of the thesis is organized as follows. Chapter 2 describes the models used. Chapter 3 reports a sequence of solutions resulting from geostrophic adjustment to an initially unbalanced density front, which are intended to reveal dynamical insight into circulations driven by horizontal density gradients. In Chapter 4, solutions and dynamics of river-outflow-driven circulations in the $1\frac{1}{2}$ -layer models are discussed. Chapter 5 provides a discussion of $2\frac{1}{2}$ -layer model solutions that examine effects caused by lower-layer inflow, background currents and wind stress. Finally, Chapter 6 provides a summary and discussion. Solutions will be compared to others mentioned above at several places in the text.

CHAPTER 2

THE OCEAN MODELS

Figure 4 provides a schematic diagram of the $1\frac{1}{2}$ -layer model. It consists of an oceanic mixed layer with initial layer thickness H_1 , salinity S_1^* and temperature T_1^* , overlying an inert deep ocean of salinity S_d and temperature T_d where the pressure gradient field vanishes. River water with salinity S_r and temperature T_r is introduced into this layer through the side wall, thereby generating motion in the layer and forming a fresher water plume. Across the front between the plume and the oceanic water, salinities and layer thicknesses vary continuously when the model includes horizontal mixing, and discontinuously when it does not (as is depicted in Figure 4). The $2\frac{1}{2}$ -layer model is an extension of the $1\frac{1}{2}$ -layer model that includes an additional active layer (the lower layer) between the upper layer and the deep ocean.

2.1 Governing equations

2.1.1 Nonlinear, $1\frac{1}{2}$ -layer model: Equations of motion for the nonlinear, $1\frac{1}{2}$ -layer model are

$$(h_1 \mathbf{v}_1)_t + \nabla \cdot (\mathbf{v}_1 h_1 \mathbf{v}_1) + f \mathbf{k} \times (h_1 \mathbf{v}_1) + h_1 \left\langle \frac{1}{\rho_1} \nabla p_1 \right\rangle = \nu \nabla^2 (h_1 \mathbf{v}_1), \quad (1a)$$

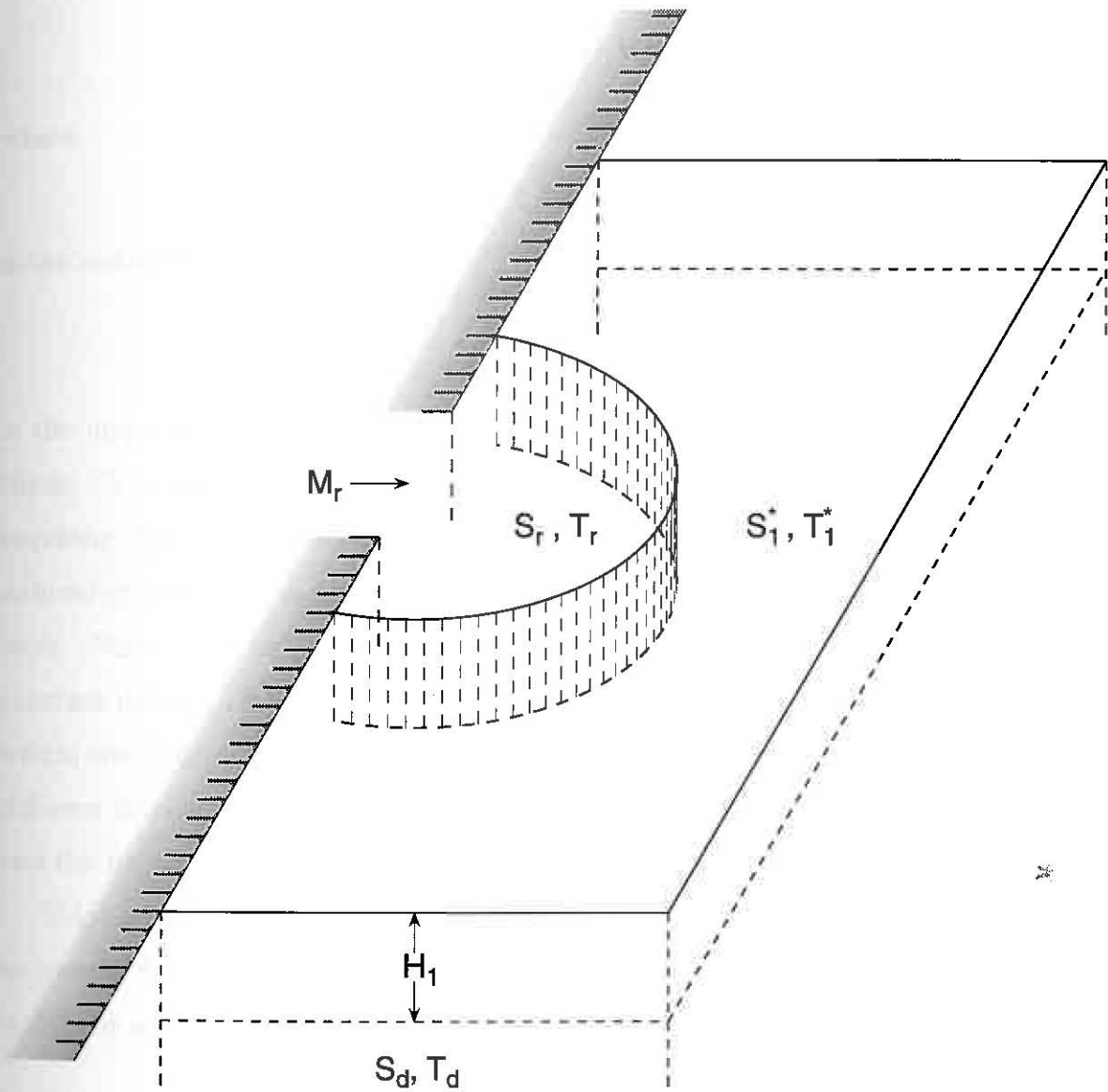
$$h_{1t} + \nabla \cdot (h_1 \mathbf{v}_1) = w_e, \quad (1b)$$

$$S_{1t} + \mathbf{v}_1 \cdot \nabla S_1 = \kappa_S \nabla^2 S_1 + \frac{1}{2}(w_e + |w_e|)(S_d - S_1)/h_1, \quad (1c)$$

$$T_{1t} + \mathbf{v}_1 \cdot \nabla T_1 = \kappa_T \nabla^2 T_1 + \frac{1}{2}(w_e + |w_e|)(T_d - T_1)/h_1, \quad (1d)$$

Figure 4: A schematic diagram of the variable-density, $1\frac{1}{2}$ -layer model. Initially, there is an oceanic mixed layer of thickness H_1 , salinity S_1^* and temperature T_1^* overlying a deep ocean of salinity S_d and temperature T_d . River water with a transport M_r , salinity S_r and temperature T_r is discharged into the upper layer to form a fresher water plume and drive the motion. The instantaneous layer thicknesses, velocities, salinities and temperatures are h_1 , v_1 , S_1 and T_1 , respectively. Density jumps across the front between the fresher and salty regions when there is no mixing (as illustrated in the figure) and varies smoothly when mixing is included.

variable-density, 1½-layer model



where h_1 , v_1 , S_1 and T_1 are instantaneous values of layer thickness, velocity, salinity and temperature. The quantities ν , κ_T and κ_S are coefficients of horizontal mixing in the momentum, temperature and salinity equations, respectively. The Coriolis parameter f is assumed to be constant.

The depth-integrated pressure gradient in the layer term in (1a) is

$$h_1 \left\langle \frac{1}{\rho_1} \nabla p_1 \right\rangle = g'_1 h_1 \nabla h_1 + \frac{1}{2} h_1^2 \nabla g'_1 = \nabla \left(\frac{1}{2} g'_1 h_1^2 \right) \equiv \nabla \mathcal{P}_1, \quad (2)$$

where

$$g'_1 = g(\rho_d - \rho_1) / \rho_d \quad (3)$$

is the reduced-gravity coefficient,

$$\rho_1(T_1, S_1) = \rho_d [1 - \alpha_T(T_1 - T_d) + \alpha_S(S_1 - S_d)] \quad (4)$$

is the upper layer density, and α_T and α_S are coefficients of expansion. Throughout the thesis, $\mathcal{P}_1 = \frac{1}{2} g'_1 h_1^2$ is referred as the depth-integrated pressure. Equation (2) results from requiring that the pressure gradient in the deep layer vanishes, a condition assumed in all reduced-gravity models, and for convenience a factor of ρ_d / ρ_1 (≈ 1) is included in the second term. Note that the second term of (2) is due to variations of layer thickness, as in a constant-density, $1\frac{1}{2}$ -layer model, whereas the third is caused by horizontal density gradients within the layer. The existence of these two terms suggests that there are two distinctively different driving mechanisms associated with river outflow: the mass input that causes ∇h_1 and the fresher water input that causes $\nabla g'_1$. This difference is explored in Section 3.1.2.

Velocity w_e parameterizes entrainment and detrainment, the processes that allow water to transfer from one layer to another. Its default value is zero. When specified otherwise, it is defined as

$$w_e = \frac{H_e - h_1}{t_e} \theta(H_e - h_1) - \frac{h_1 - H_d}{t_d} \theta(h_1 - H_d), \quad (5)$$

where θ represents a step function. Parameters H_e and H_d are prescribed critical values of layer thicknesses at which entrainment and detrainment are switched on, respectively, and t_e and t_d are the corresponding time scales of relaxation. The terms involving w_e in equation (1) are formulated in such a way that conservation of momentum, mass, salinity and heat is

ensured. Equation (5) and variations of it have been successfully used in a number of studies (e.g., McCreary and Kundu, 1989).

Due to the horizontal mixing on temperature and salinity in equations (1c) and (1d), density necessarily varies continuously across the front. For the analytic solutions obtained in Section 4.1.3, however, mixing is neglected. In these solutions, density jumps discontinuously across the front, and the model equations are those for a constant-density system in the region on either side. The system can still be regarded as a $1\frac{1}{2}$ -layer, variable-density model, since the two regions have different densities and they are both part of the upper layer.

2.1.2 Linearized, $1\frac{1}{2}$ -layer model: A nearly linear version of the above model is

$$\tilde{u}_{1t} - f\tilde{v}_1 + \Phi_x = 0, \quad (6a)$$

$$\tilde{v}_{1t} + f\tilde{u}_1 + \Phi_y = 0, \quad (6b)$$

$$\tilde{h}_{1t} + H_1(\tilde{u}_{1x} + \tilde{v}_{1y}) = 0, \quad (6c)$$

$$\tilde{g}'_{1t} + \tilde{u}_1\tilde{g}'_x + \tilde{v}_1\tilde{g}'_y = 0, \quad (6d)$$

where the depth-averaged pressure is given by

$$\Phi = g'_0\tilde{h}_1 + \frac{1}{2}H_1\tilde{g}'_1. \quad (7)$$

In these equations, variables with a tilde are deviations from a motionless background state consisting of a uniform layer of thickness H_1 , constant density ρ_0 , and hence a constant reduced-gravity coefficient $g'_0 = g(\rho_d - \rho_0)/\rho_d$. It is noteworthy to point out that the disturbed reduced-gravity $\tilde{g}'_1 = g(\rho_0 - \rho_1)/\rho_d$ is directly related to the density perturbation by a constant. Note that if $\tilde{g}'_1 \equiv 0$, (6) reduces to the set of linear equations for a constant-density layer model. The \tilde{g}'_1 term in (7) is the pressure gradient generated by density variations within the layer, the equivalent of the third term in equation (2) for the nonlinear model.

The linearization of the momentum and continuity equations make it possible to draw a parallel between circulations driven by density variation in this model and by potential-vorticity variation in a constant-density model (see Section 3.1.3). It also allows the river-outflow driven circulation to be split into two distinct parts in order to understand the dynamics. The only nonlinear terms retained in (6) are the advection terms in equation

(6d); they allow the studies of the slow evolution of river plumes, which is necessarily an advective process. Note that equation (6d) is derived by combining the inviscid version of equations (1c) and (1d) and by using (3) and (4).

2.1.3 Nonlinear, $2\frac{1}{2}$ -layer model: Equations of motion for the upper layer of the $2\frac{1}{2}$ -layer model are

$$(h_1 \mathbf{v}_1)_t + \nabla \cdot (\mathbf{v}_1 h_1 \mathbf{v}_1) + f \mathbf{k} \times (h_1 \mathbf{v}_1) + h_1 \left\langle \frac{1}{\rho_1} \nabla p_1 \right\rangle = \frac{\tau}{\rho_1} + \nu \nabla^2 (h_1 \mathbf{v}_1), \quad (8a)$$

$$h_{1t} + \nabla \cdot (h_1 \mathbf{v}_1) = w_e, \quad (8b)$$

$$S_{1t} + \mathbf{v}_1 \cdot \nabla S_1 = \kappa_S \nabla^2 S_1 + \frac{1}{2}(w_e + |w_e|)(S_2 - S_1)/h_1, \quad (8c)$$

$$T_{1t} + \mathbf{v}_1 \cdot \nabla T_1 = \kappa_T \nabla^2 T_1 + \frac{1}{2}(w_e + |w_e|)(T_2 - T_1)/h_1, \quad (8d)$$

where $\tau = \tau^x \mathbf{i} + \tau^y \mathbf{j}$ is the wind stress forcing the model and is set to zero for all the solutions except for those in Section 5.3. Equations for the lower layer are

$$(h_2 \mathbf{v}_2)_t + \nabla \cdot (\mathbf{v}_2 h_2 \mathbf{v}_2) + f \mathbf{k} \times (h_2 \mathbf{v}_2) + h_2 \left\langle \frac{1}{\rho_2} \nabla p_2 \right\rangle = \nu \nabla^2 (h_2 \mathbf{v}_2) - b h_2 \mathbf{v}_2, \quad (9a)$$

$$h_{2t} + \nabla \cdot (h_2 \mathbf{v}_2) = -w_e, \quad (9b)$$

$$S_{2t} + \mathbf{v}_2 \cdot \nabla S_2 = \kappa_S \nabla^2 S_2 + \frac{1}{2}(-w_e + |w_e|)(S_1 - S_2)/h_2, \quad (9c)$$

$$T_{2t} + \mathbf{v}_2 \cdot \nabla T_2 = \kappa_T \nabla^2 T_2 + \frac{1}{2}(-w_e + |w_e|)(T_1 - T_2)/h_2, \quad (9d)$$

where h_2 , v_2 , S_2 and T_2 are lower-layer thickness, velocity, salinity and temperature. Depth-integrated pressure gradients in the two layers are

$$\left\langle \frac{1}{\rho_1} \nabla p_1 \right\rangle = \nabla(g'_1 h_1 + g'_2 h_2) - \frac{1}{2} h_1 \nabla g'_1, \quad (10a)$$

$$\left\langle \frac{1}{\rho_2} \nabla p_2 \right\rangle = \nabla(g'_2 h_1 + g'_2 h_2) - (h_1 + \frac{1}{2} h_2) \nabla g'_2, \quad (10b)$$

where

$$g'_2 = g(\rho_d - \rho_2)/\rho_d \quad (11)$$

and

$$\rho_2 = \rho_d [1 - \alpha_T (T_2 - T_d) + \alpha_S (S_2 - S_d)] \quad (12)$$

are the reduced-gravity coefficient and density for the lower layer. The term $-bh_2\mathbf{v}_2$ is included only for solutions that include forcing by the wind (see Section 5.3).

2.2 Basin and boundary conditions

For most numerical solutions, the model basin is a north-south channel 600 km long and 150 km wide; however, the width of the channel is increased to 300 km in solutions when a large offshore plume develops. For most solutions driven by river outflow, the river mouth is centered at $y = \bar{y} = 300$ km along the western boundary and has a width W of 25 km. The origin of the coordinate system (x, y) is located at the southwestern corner of the basin, with x and y being directed toward the east and north, respectively.

Open northern and southern boundary conditions are imposed in all calculations. They are

$$u_{iy} = v_{iy} = h_{iy} = S_{iy} = T_{iy} = 0, \quad (13)$$

where subscript $i = 1, 2$ is a layer index. In addition, for the solutions in Chapter 3, linear dampers that relax fields to their background state are included within 12.5 km of those boundaries.

No-slip, closed, boundary conditions,

$$u_i = \nu v_i = \kappa_S S_{ix} = \kappa_T T_{ix} = 0, \quad (14)$$

are adopted along the eastern and western boundaries for solutions with horizontal mixing. The constraints $\nu v_i = \kappa_S S_{ix} = \kappa_T T_{ix} = 0$ along these boundaries are not applicable for the inviscid systems, so that their boundaries are slippery. *

Within the river mouth ($\bar{y} - \frac{1}{2}W < y < \bar{y} + \frac{1}{2}W$), upper-layer boundary conditions are

$$h_1 u_1 = M_r Y(y) T(t), \quad (15a)$$

$$S_1 = S_r, \quad T_1 = T_r = T_1^*, \quad (15b)$$

where M_r , S_r and T_r are the specified transport, salinity and temperature of the outflow, respectively. Note that T_r is set to T_1^* , the initial temperature of the upper layer. Unless specified otherwise, the across-stream structure of the outflow is

$$Y(y) = \frac{\pi}{2W} \sin\left(\pi \frac{y - y_1}{W}\right), \quad (16)$$

where $y_1 = \bar{y} - \frac{1}{2}W$. The time function is

$$T(t) = \begin{cases} t/\delta t, & 0 < t \leq \delta t \\ 1, & t > \delta t, \end{cases} \quad (17)$$

that is, a ramp with the time scale $\delta t = 1$ day. With this choice for δt , inertial oscillations are effectively inhibited. Where applicable, lower-layer boundary conditions within the river mouth are

$$h_2 u_2 = M_2 Y(y) T(t), \quad (18a)$$

$$\nu v_2 = \kappa_S S_{2x} = \kappa_T T_{2x} = 0. \quad (18b)$$

The lower-layer transport M_2 is not independent from M_r , and its specification is provided at the beginning of Chapter 5.

2.3 Numerical methods and parameter choices

Numerical solutions are found on a staggered grid, with h_i , S_i and T_i points located at the center of the grid boxes, and u_i and v_i points located on their meridional and zonal edges, respectively (the *C*-grid of Arakawa and Lamb, 1977). The size of the boxes is usually $\Delta x = \Delta y = 2.5$ km, which is adequate to resolve plume widths for most solutions; exceptions are for some of the solutions that produce the data points in Figure 14, which have very narrow plumes, and the grid size is reduced to 1 km for these solutions. Except mixing terms which are integrated in time using forward scheme, all other terms are integrated in time using the leapfrog scheme. The time step Δt is 3 minutes. Fields are averaged between successive time levels every 41 time steps to inhibit time-splitting instability.

Terms involving horizontal gradients are generally formulated by using the centered-difference scheme. An exception is for the advection terms in the salinity and temperature equations, where an upwind-difference scheme is used to ensure positive definiteness. Solutions that utilize centered-difference advection can develop salinity values greater than S_1^* and less than S_r ; however, their overall structure is not much changed, which indicates that the additional numerical mixing associated with the upwind scheme is not a problem.

Unless stated otherwise, parameter values are those listed in Table 1. They are either physically realistic or numerically sensible choices. For example, salinity near the mouth of

the Changjiang River varies from 5 to 25 during the summer; farther offshore, there is a mixed layer in the upper 10–20 m where salinity and temperature are about 30 and 25°C, overlying a bottom layer where they are about 33 and 15°C (Limeburner and Beardsley, 1982). The annual-mean transport of the Changjiang River is $3 \times 10^4 \text{ m}^3/\text{s}$, with a peak value of $4.5 \times 10^4 \text{ m}^3/\text{s}$ during the summer (Beardsley *et al.*, 1983). In contrast, the annual-mean discharge of the Delaware River is only $4 \times 10^2 \text{ m}^3/\text{s}$, with a peak outflow of $2 \times 10^3 \text{ m}^3/\text{s}$ (Münchow and Garvine, 1993). Our standard river transport, $M_r = 10^4 \text{ m}^3/\text{s}$, corresponds to a moderate-to-strong outflow. Note that in the $1\frac{1}{2}$ -layer model, S_d and T_d have the values of S_2^* and T_2^* , respectively.

Table 1: A list of parameter values used in all runs unless specified otherwise. The drag coefficient b is zero for all but one of the solutions in Section 5.3, where it is set to $0.5 \times 10^{-4} \text{ s}^{-1}$.

Parameter	Notation	Value
Coriolis parameter	f	$0.8 \times 10^{-4} \text{ s}^{-1}$
Coeff. of thermal expansion	α_T	$2.5 \times 10^{-4} \text{ }^\circ\text{C}^{-1}$
Coeff. of salinity expansion	α_S	0.8×10^{-3}
Deep-ocean density	ρ_d	1.024 g/cm^3
Mixing coeffs.	ν, κ_T, κ_S	$10^5 \text{ cm}^2/\text{s}$
Drag coeff.	b	0 s^{-1}
Initial layer thicknesses	H_1, H_2	10, 25 m
Initial layer temperatures	T_1^*, T_2^*	25, 15°C
Initial layer salinities	S_1^*, S_2^*	30, 35
Deep-ocean temp. ($1\frac{1}{2}$ -layer model)	T_d	15°C
Deep-ocean temp. ($2\frac{1}{2}$ -layer model)	T_d	5°C
Deep-ocean salinity	S_d	35
Outflow transport	M_r	$10^4 \text{ m}^3/\text{s}$
River temperature	T_r	25°C
River salinity	S_r	20
Thicknesses for w_e	H_e, H_d	7.5, 12.5 m
Time scales for w_e	t_e, t_d	$2\Delta t$
Wind stress	τ^x, τ^y	0, 0 dyn/cm^2

CHAPTER 3

GEOSTROPHIC ADJUSTMENT

Properties of geostrophic adjustment are investigated in this chapter. The investigation is intended to provide insights into how horizontal density gradients in the upper layer drive circulation in the river-outflow-driven solutions discussed in the next chapter. Specifically, in Sections 3.1 and 3.2, responses to an initially unbalanced, y -independent density front are obtained using both the linear and nonlinear versions of the variable-density, $1\frac{1}{2}$ -layer model, and they are compared with analogous solutions to constant-density layer models. In these solutions, the front between the fresher and salty regions is kept vertically-oriented throughout the adjustment. In Section 3.3, an analytic solution is obtained by using a combination of constant-density, $1\frac{1}{2}$ -layer and $2\frac{1}{2}$ -layer models that allows the front to slant.

3.1 Solutions to the linearized, $1\frac{1}{2}$ -layer model

Consider a situation in which initially there is a y -independent density front in a variable-density, $1\frac{1}{2}$ -layer model. The front is formed by two quiescent water masses that meet along $x = 0$. The initial layer thicknesses and temperatures for both water masses are uniformly H_1 and T_1^* , and the salinities are S_1^* and S_r ($< S_1^*$) in regions to the right ($x > 0$) and left ($x < 0$) of the front, respectively. The right-hand region is referred as the background state, so that $\rho_0 = \rho_d[1 - \alpha_T(T_1^* - T_d) + \alpha_S(S_1^* - S_d)]$. There is an unbalanced pressure gradient force across the front, and the system subsequently adjust towards equilibrium by gravity-wave radiation.

3.1.1 Numerical results: The y -independent version of equations (6a)–(6c) is numerically integrated when the parameters are those listed in Table 1. For simplicity, equation (6d) is *not* integrated, so that the density front remains steady. In addition, to minimize inertial oscillations, the salinity in the region $x < 0$ is gradually decreased to its prescribed value from S_1^* through a ramp of the form (17) instead of being suddenly imposed.

Figure 5 shows solutions at day 20, by which time the system has nearly reached a steady state. The prominent feature of these solutions is a frontally-trapped alongfront current. The maximum speed of this current is attained at the front and its value is 21 cm/s. Note that layer thickness h_1 thins and thickens towards the density front from the left and right sides, respectively, consistent with geostrophically balanced current. As a result, h_1 jumps by 4.9 m across the front, which has a width of 2.5 km due to the finite grid size.

3.1.2 Analytical results: The steady-state response can be easily solved for analytically. Conservation of potential vorticity (factored by a constant H_1) for system (6a)–(6c), that is, $(\tilde{v}_{1x} - \tilde{u}_{1y} - \frac{f}{H_1}\tilde{h}_1)_t = 0$, yields an equation in Φ alone

$$\nabla^2\Phi - R_+^{-2}\Phi = -\frac{1}{2}f^2\frac{\tilde{g}_1}{g_0} + f\tilde{q}_1^*, \quad (19)$$

where $R_+ = \sqrt{g_0' H_1 / f}$ is the Rossby radius of the background state, and the quantity $\tilde{q}_1^* = (\tilde{v}_{1x} - \tilde{u}_{1y} - \frac{f}{H_1}\tilde{h}_1)_{t=0}$ is the initial potential vorticity perturbation multiplied by H_1 . For the variable-density model, it is always zero since the initial condition is motionless and the layer thickness is uniformly H_1 .

To solve (19), the boundary conditions $\Phi = 0$ as $x \rightarrow \pm\infty$, as well as the frontal^{*} matching conditions

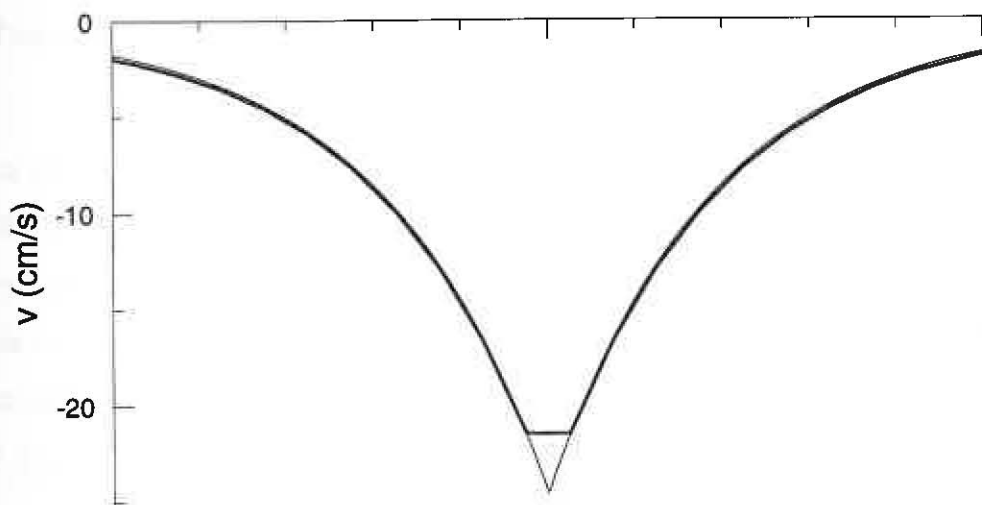
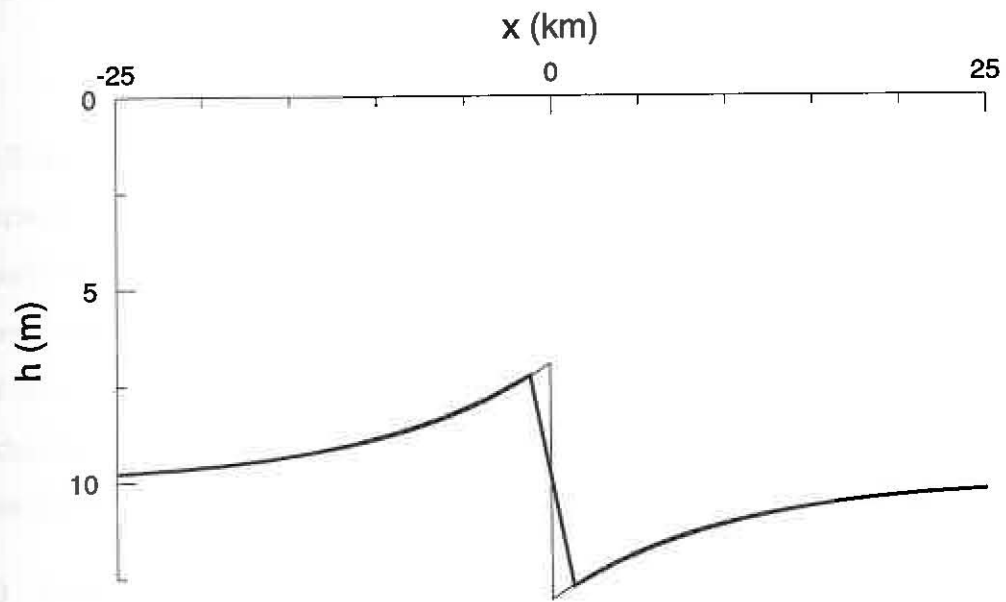
$$\Phi_- = \Phi_+, \quad (\Phi_-)_x = (\Phi_+)_x \quad @ \ x = 0, \quad (20)$$

are utilized, where subscripts “-” and “+” denote solutions in regions $x < 0$ and $x > 0$, respectively. These conditions are the linearized version of the corresponding conditions for the nonlinear case in next section. [See the discussion of (24).]

The resulting solutions are

$$\tilde{h}_- = -\frac{1}{4g_0'}\tilde{g}_1 H_1 e^{x/R_+}, \quad \tilde{h}_+ = \frac{1}{4g_0'}\tilde{g}_1 H_1 e^{-x/R_+}, \quad (21a)$$

Figure 5: Day-20 numerical (thick curves) and steady-state analytic (thin curves) solutions resulting from geostrophic adjustment of a y -independent density front in a linear, variable-density, $1\frac{1}{2}$ -layer model. The upper panel shows layer thicknesses h_1 , and the lower panel plots the corresponding alongfront velocities v_1 . For the analytic solution, the jump in layer thicknesses across the density front is 6.1 m, and the maximum speed of the current is 24.5 cm/s. For the numerical solution, the front has a width of 2.5 km due to the finite resolution of the staggered grid, the jump in h_1 is 4.9 m and the maximum speed of the current is 21 cm/s.



and the frontal current associated with (21a) is

$$\tilde{v}_- = -\frac{1}{4fR_+} \tilde{g}'_1 H_1 e^{x/R_+}, \quad \tilde{v}_+ = -\frac{1}{4fR_+} \tilde{g}'_1 H_1 e^{-x/R_+}, \quad (21b)$$

which follows from geostrophy [the steady-state balance of (6a) and (6b)]. Solution (21) demonstrates that the decay scale of the geostrophic current is R_+ . In addition, \tilde{v}_1 and \tilde{h}_1 are proportional to \tilde{g}'_1 , indicating that the density gradient is the driving force of the flow.

Figure 5 also plots $h_1 = H_1 + \tilde{h}_1$ and \tilde{v}_1 for the analytic solution. Both fields are virtually identical to their numerical counterparts everywhere except near the density front, where the maximum speed (24.5 cm/s) and the jump in h_1 (6.1 m) are slightly higher than the numerical ones, the differences being due to the finite resolution of numerical grid.

3.1.3 Comparison with constant-density model: The above solutions are similar to those in a constant-density model that result from the geostrophic adjustment to an initially imposed jump in layer thicknesses (*e.g.*, Gill, 1982). This similarity suggests that there is a dynamical connection between the driving mechanisms of density perturbation in the variable-density model and of potential-vorticity perturbation in a constant-density layer model. That connection is

$$\frac{\tilde{g}'_1}{g'_0} = -2 \frac{\tilde{q}_1^*}{f}, \quad (22)$$

which can be found by equating the two terms on the right-hand side of equation (19). The above relation ensures that the two driving forces result in the same geostrophic currents when they acts separately.

Equation (22) establishes an equivalence between low salinity (high \tilde{g}'_1) in the variable-density model and low potential vorticity in a constant-density model: each anomaly drives the same geostrophic current. In the above example, $g'_0 = 6.37 \text{ cm/s}^2$ and $\tilde{g}'_1 = 7.8 \text{ cm/s}^2$, so that $\tilde{q}_1^* = -0.6f$, which is equivalent to a perturbation in initial layer thickness of $\tilde{h}_1^* = 6 \text{ m}$. This means that the geostrophic adjustment to an initial disturbance of 6 m in layer thickness in the region $x < 0$ in a constant-density model will generate exactly the same geostrophic current as discussed above. Moreover, the transient solution for \tilde{v}_1 is also the same as in the corresponding constant-density model since equations (6a)–(6c) have exactly the same form in each system. The only difference is that layer thickness in the variable-density model

jumps across the front in order for pressure to remain continuous.

3.2 Solutions to the nonlinear, $1\frac{1}{2}$ -layer model

3.2.1 Numerical results: The y -independent, inviscid version of equations (1) is integrated, and the day-20 solution is shown in Figure 6. It is similar to the linear solution, suggesting that the nonlinearity is not a fundamental process. The maximum current (15 cm/s), and the difference between the lowest and highest h_1 (2.1 m) across the front, are both smaller than their linear counterparts. This weakening is due to internal mixing caused by the upwind scheme on salinity during the adjustment (which did not influence the linear solution since the density equation was not integrated).

3.2.2 Analytic results: In this case, the density front is allowed to move during the adjustment, and as a result, it shifts to the right by a distance ε in the steady state. To obtain the steady-state analytic solution, separate solutions are found in the fresher-water ($-\infty < x < \varepsilon$) and salty water ($\varepsilon < x < +\infty$) regions, and then they are matched across the front. The fluid conserves potential vorticity in each region, a consequence of the second term followed the first equal sign in (2) being identically zero. It follows that

$$(h_j)_{xx} - R_j^2 h_j = -R_j^2 H_1, \quad (23)$$

where $j = -$ and $+$ represent regions of fresher water and salty water, respectively, and $R_j = \sqrt{g_j H_1}/f$ are the Rossby radii in the corresponding regions. To solve (23), boundary conditions $h_j \rightarrow H_1$ as $x \rightarrow \pm\infty$, as well as frontal matching conditions

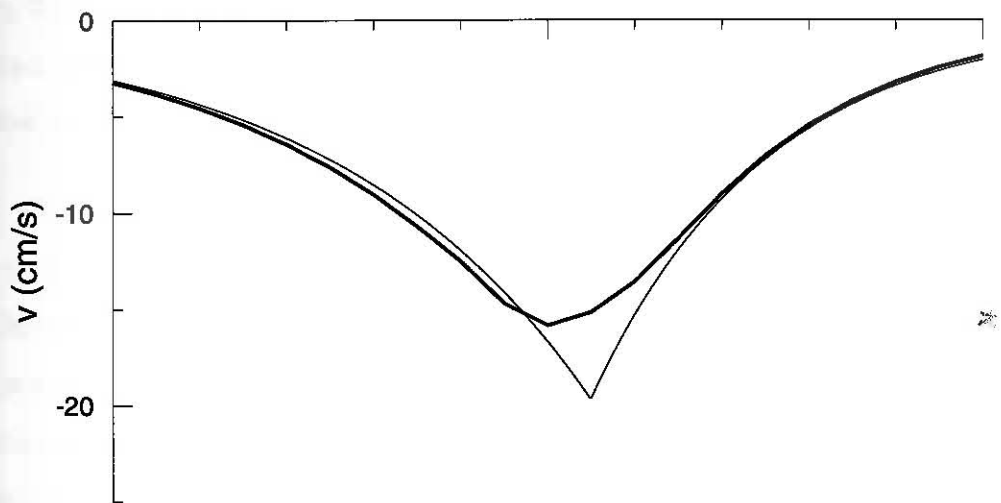
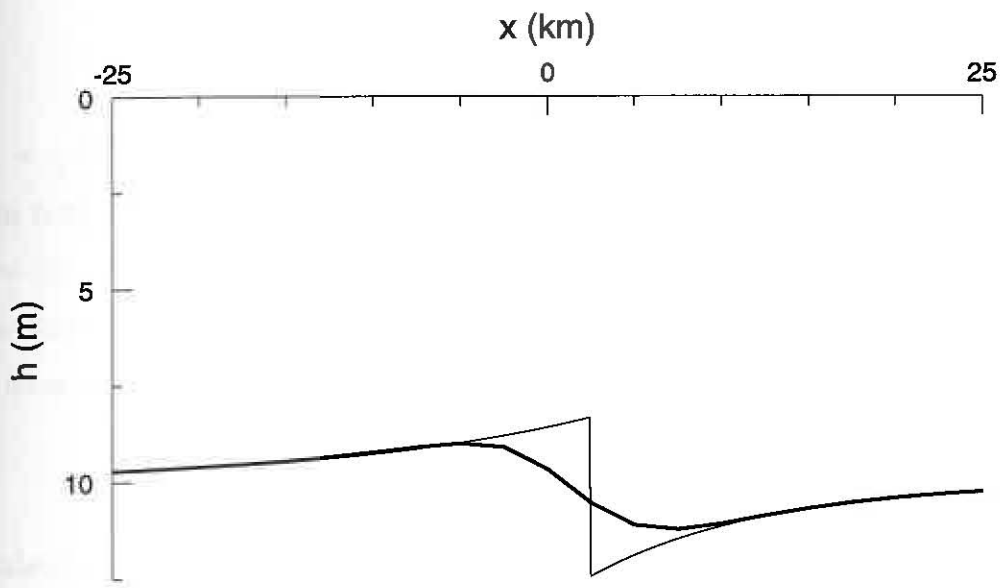
$$g'_-(h_-)_x = g'_+(h_+)_x, \quad \frac{1}{2}g'_-h_-^2 = \frac{1}{2}g'_+h_+^2 \quad @ x = \varepsilon, \quad (24)$$

are needed. The first condition in (24) results from the constraint $u_- = u_+$, which ensures that two water particles initially adjacent to each other across the front will never separate during the adjustment: Since $dv_j/dt + fu_j = 0$ is true for every water particle, it follows immediately that $v_- = v_+$ and hence $g'_-(h_-)_x = g'_+(h_+)_x$ by geostrophy. The second condition follows from energy conservation.

The resulting solutions are

$$h_- = H_1 \left[1 - \frac{1-\gamma}{2} e^{(x-\varepsilon)/R_-} \right], \quad h_+ = H_1 \left[1 + \frac{1-\gamma}{2\gamma} e^{-(x-\varepsilon)/R_+} \right], \quad (25a)$$

Figure 6: As in Figure 5, expect for nonlinear, variable-density, $1\frac{1}{2}$ -layer model. For the analytic solution, the density front in the steady state shifts to the right by a distance $\varepsilon = \frac{1}{2}(R_- - R_+) = 2.5$ km, the jump in layer thicknesses across the front is 4.1 m, and the maximum speed of the current is 19.2 cm/s. For the numerical solution, the density front is broadened due to implicit mixing on salinity by the upwind advection scheme, and there is no jump in h_1 . The maximum value of v_1 is 15 cm/s.



where $\gamma = R_+/R_- < 1$, and the corresponding alongfront currents are

$$v_- = -c_- \frac{1-\gamma}{2} e^{(x-\varepsilon)/R_-}, \quad v_+ = -c_- \frac{1-\gamma}{2} e^{-(x-\varepsilon)/R_+}, \quad (25b)$$

where $c_- = \sqrt{g'_- H_1}$ is the characteristic wave speed of the fresher water region. The amplitudes in both alongfront current v_1 and thickness perturbation $h_1 - H_1$ are proportional to $1 - \gamma = (R_- - R_+)/R_-$, which in turn is proportional to the density difference between the two waters. This property is consistent with that in the linear case. The distance ε is obtained from mass conservation for each water mass, which gives

$$\varepsilon = \frac{1}{2}(R_- - R_+). \quad (26)$$

(See Glendening, 1993, for an analogous problem in a constant-density model.) It can be proved that as $R_- \rightarrow R_+$, the nonlinear solution (25) reduces to the linear one (21).

This analytic solution is also plotted in Figure 6. Much like the linear solution, a frontally-trapped geostrophic current is established with a decay scale of R_- (15 km) and R_+ (10 km) in the fresher and salty water regions, respectively. The maximum speed at the front is 19.2 cm/s, the jump in h_1 is 4.1 m and the frontal displacement is only 2.5 km, considerably smaller than either R_- or R_+ . The corresponding numerical solution showed no significant shift, probably because of the gradual spin-up of the fresher-water region.

3.2.3 Comparison with constant-density model: Properties of the above solutions are very much like those obtained from a geostrophic adjustment to an initial disturbance in layer thickness in the nonlinear constant-density layer model of Glendening (1993). The common feature in these solutions is that geostrophic adjustment generates a frontally-trapped current that decays away from the front with a scale of the Rossby radius. Moreover, the amplitude of the current and the displacement of the front are both determined by the difference in Rossby radii between the two regions. However, the difference in Rossby radii is due to density difference in the former and due to layer thickness in the latter.

Similar to equation (22), a quantitative relation can be found that relates forcing by layer-thickness and density anomalies. Suppose initial layer thicknesses are allowed to be different, *i.e.*, to be H_- and H_+ in the fresher- and salty-water regions, respectively. Then

the solution to equation (23), with H_1 being replaced by H_j , for the alongfront velocity is

$$v_- = Ve^{(x-\varepsilon)/R_-}, \quad v_+ = Ve^{-(x-\varepsilon)/R_+}, \quad (27)$$

where

$$V = -\frac{H_-/H_+ \sqrt{g'_-/g'_+} - 1}{1 + \sqrt{H_-/H_+}} c_+, \quad (28)$$

where $c_+ = \sqrt{g'_+ H_+}$. The numerator of the fraction in equation (28) indicates that either $H_-/H_+ > 1$ in a constant-density model ($g'_-/g'_+ = 1$) or $g'_-/g'_+ > 1$ in a variable-density model with initial uniform layer thickness ($H_-/H_+ = 1$) can drive a southward geostrophic current ($V < 0$). To quantify the relation between these two forcings, simply equate the value of V when $H_-/H_+ = 1$ and that when $g'_-/g'_+ = 1$, which yields

$$\frac{1}{2} \left(\sqrt{g'_-/g'_+} - 1 \right) = \sqrt{H_-/H_+} - 1 = \sqrt{q_+/q_-} - 1, \quad (29)$$

where q_{\pm} are the corresponding potential vorticities. In the limit $g'_- - g'_+$ and $H_- - H_+$ are small, it can be easily proved that equation (29) reduces to equation (22).

3.3 Solutions with a slanted front

3.3.1 Analytical solution: In the previous solutions and throughout the rest of this thesis, the density front within the layer is kept vertically oriented. In the real ocean, however, fronts are often observed to be tilted, especially in regions where vertical mixing is not strong (Young, 1994). Using a combination of constant-density, $1\frac{1}{2}$ - and $2\frac{1}{2}$ -layer models, it is possible to obtain an analytic solution with a slanted front that otherwise corresponds to the solutions in Section 3.2.2; indeed, the initial states are identical in both cases. The derivation of this solution is described in Appendix A.

The thin curves in Figure 7a show the resulting solution. Note that the solution has the structures of a $2\frac{1}{2}$ -layer model within the frontal zone ($\varepsilon_- < x < \varepsilon_+$) and of a $1\frac{1}{2}$ -layer model elsewhere. Layer thicknesses for fresher-water and salty-water vanish at $x = \varepsilon_+ = 10.5$ km and $x = \varepsilon_- = -5.5$ km, respectively. A slanted density front tilts upward from the fresher to the salty-water region (upper panel), similar to a cold front in the atmosphere. In the fresher-water layer, an alongfront geostrophic current flows everywhere in the direction with

the salty water to the left. This current attains its maximum velocity (-86.4 cm/s) at $x = \varepsilon_+$. In the salty-water layer, the water flows in the same direction as in the fresher water layer for $x > 4.2$ km; within the frontal zone, there is a region ($\varepsilon_- < x < 4.2$ km) where the water flows in the opposite direction, and its maximum velocity (45 cm/s) is attained at $x = \varepsilon_-$.

3.3.2 Comparison with the variable-density, $1\frac{1}{2}$ -layer model: For comparison, h_1 and v_1 from the solution in the previous section are also plotted in Figure 7a (thick curves), together with the mean current for the analytic solution, $\bar{v} = (h_+v_+ + h_-v_-)/(h_+ + h_-)$ (dashed curve). The two solutions nearly overlap outside the frontal zone, and the numerical v_1 compares reasonably well with \bar{v} even inside the frontal zone. This good agreement suggests that the variable-density, $1\frac{1}{2}$ -layer model does properly represent the basic dynamics of geostrophic adjustment, despite its restriction to vertically oriented fronts.

Some properties of the slanted-front solution are missed in solutions to the variable-density, $1\frac{1}{2}$ -layer model. To see this, the latter solution is split into fresher water (h_{1-} and ρ_-) and salty water (h_{1+} and ρ_+) components such that

$$h_1 = h_{1-} + h_{1+}, \quad \rho_1 h_1 = \rho_- h_{1-} + \rho_+ h_{1+}. \quad (30)$$

Thicknesses h_{1-} (short-dashed curve) and h_{1+} (long-dashed curve) are plotted together with their counterparts for the slanted-front model (solid curves) in the upper panel of Figure 7b. The transport for each water type, $h_{1-}v_1$ (short-dashed curve) and $h_{1+}v_1$ (long-dashed curve), as well as their counterparts for the slanted-front model (solid curves), are plotted in the lower panel. The total transports of the fresher- and salty-water flows for the variable-density, $1\frac{1}{2}$ -layer solution are -2.6×10^4 m³/s and -2.1×10^4 m³/s, respectively, whereas they are -4.4×10^4 m³/s and -0.5×10^4 m³/s, respectively, for the slanted-front solution. Possible effects of the weak salty-water transport in the slanted-front solution on river-outflow-driven solutions are discussed in Section 4.1.5.

Figure 7a: Comparison of steady-state solutions (thin curves) of y -independent, geostrophic adjustment for the slanted-front model described in Appendix A with day 20 solutions (considered to be in steady state) of the nonlinear, variable-density, $1\frac{1}{2}$ -layer model from Figure 6 (thick curves). The dashed lines in the upper panel indicate the initial interfaces between the waters with densities $\rho_- < \rho_+ < \rho_d$. In the slanted-front solution, a frontal zone forms in the region $\varepsilon_- < x < \varepsilon_+$, and the front tilts upwards towards the salty water (of density ρ_+) region. Layer thicknesses h_- and h_+ vanish at $x = \varepsilon_+$ and ε_- , respectively (upper panel). In the fresher layer, the current is uniformly southward; whereas in the salty layer, it is southward except that a northward flow is generated in the region $\varepsilon_- < x < 4.2$ km (lower panel). The vertically-averaged alongshore flow $\bar{v} = (h_-v_- + h_+v_+)/ (h_- + h_+)$ within the frontal zone is also plotted (dashed curve). The two solutions nearly overlap outside the frontal zone, and the numerical v_1 compares well with \bar{v} inside the frontal zone.

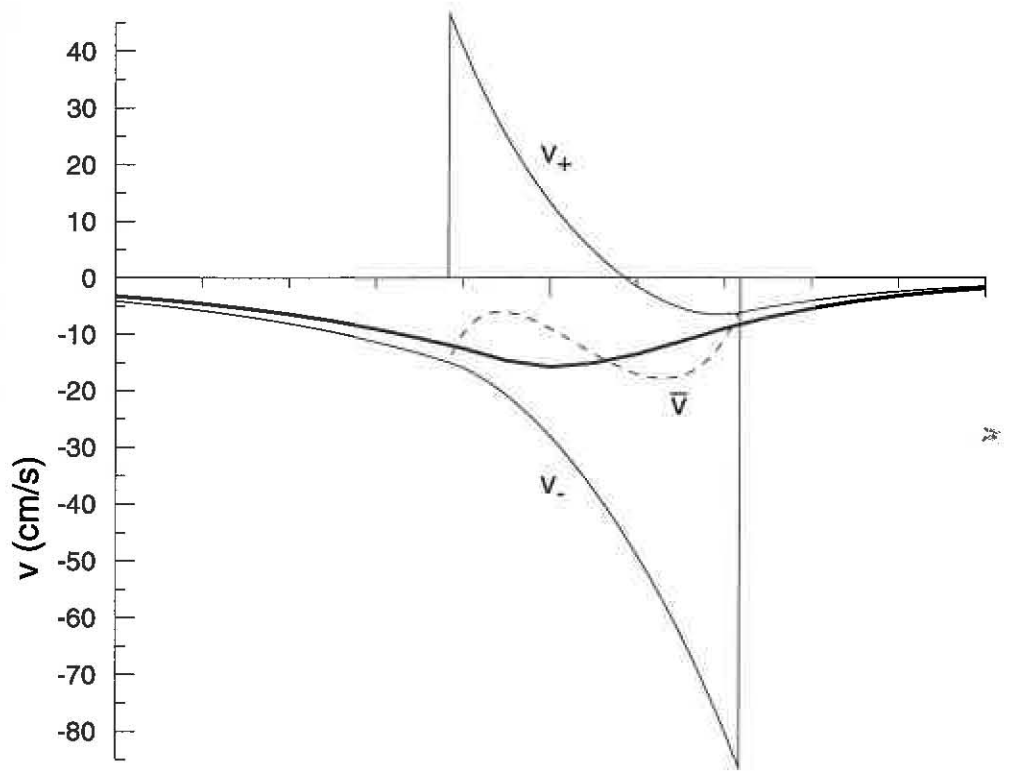
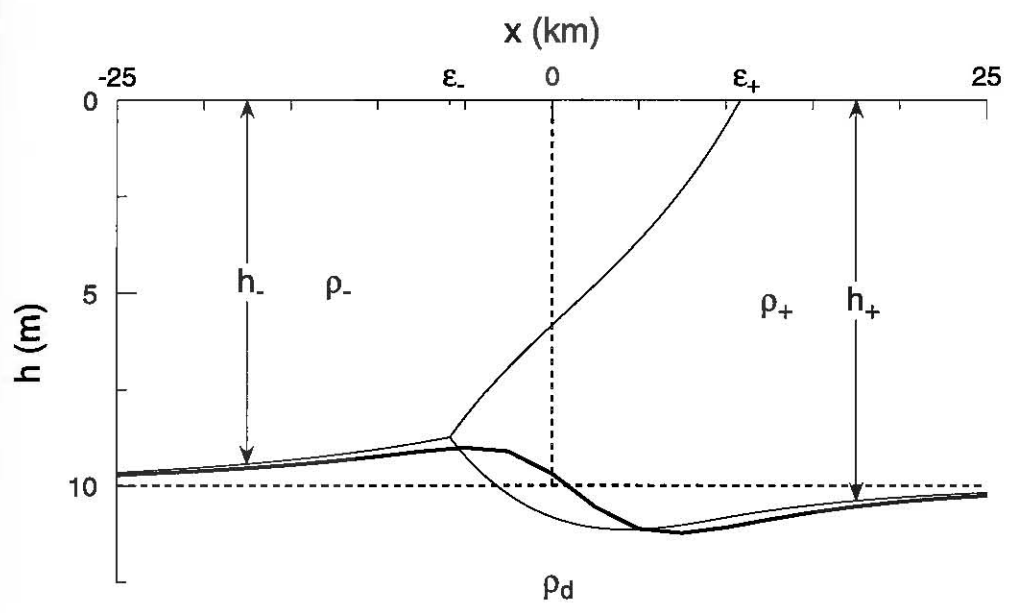
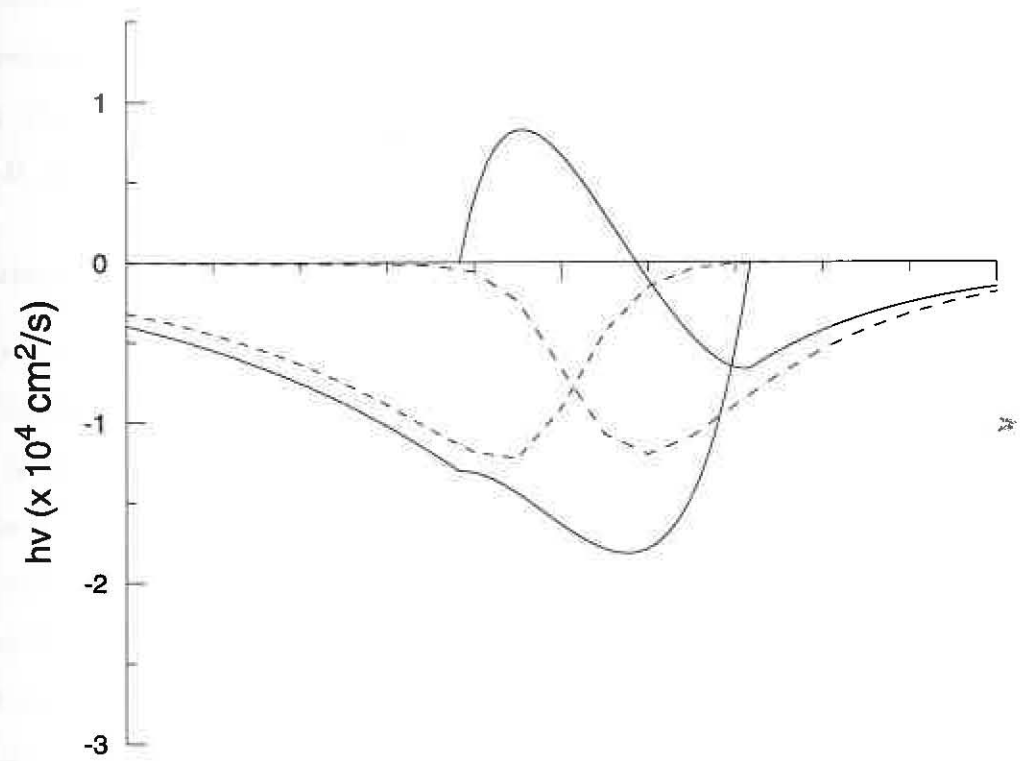
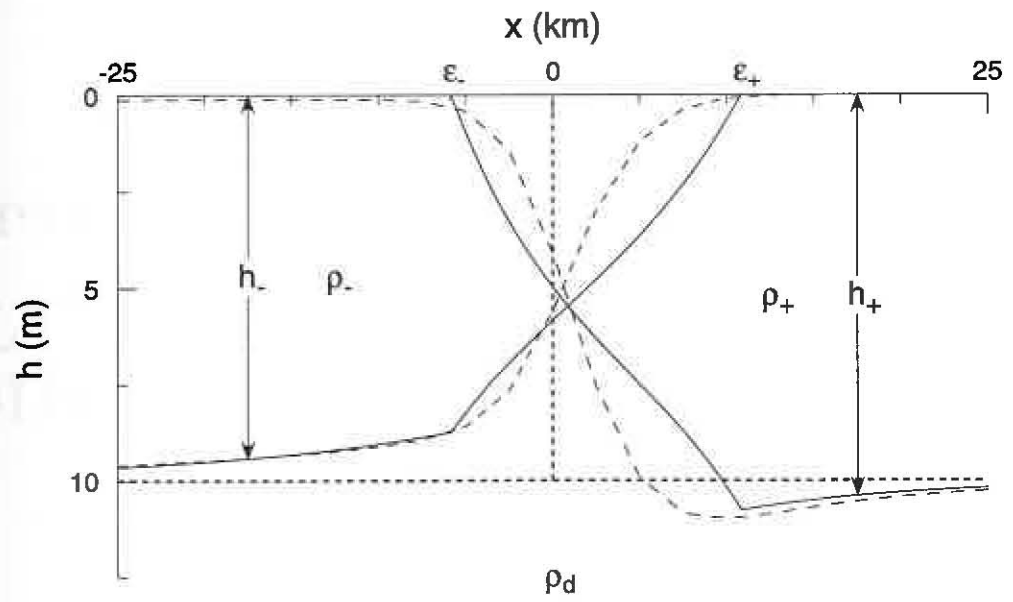


Figure 7b: Similar to Figure 7a, except contrasting the fresher- and salty-water parts of the variable-density, $1\frac{1}{2}$ -layer solution and the slanted-front solution. The upper panel shows h_{1-} (short-dashed curve) and h_{1+} (long-dashed curve) for the variable-density, $1\frac{1}{2}$ -layer solution, as well as those for the slanted-front model, h_- and h_+ (solid curves). The lower panel shows the corresponding fresher- and salty-water transports for the two solutions.



CHAPTER 4

SOLUTIONS TO THE $1\frac{1}{2}$ -LAYER MODEL

In this chapter, solutions to the $1\frac{1}{2}$ -layer model that are driven by river outflow are discussed. Sections 4.1 and 4.2 contrast solutions when the Rossby number (R_o) of the outflow [defined by $R_o = 2U/fW$, where U is the maximum velocity at the river mouth and can be estimated using equation (15a)] is low and high, respectively. Section 4.3 reports solutions when entrainment is included, and in this case the difference between the high- and low- R_o solutions tends to disappear.

4.1 Low- R_o solutions

In the low- R_o regime, a prominent feature of solutions is that the plume advances along both upstream and downstream coasts (Section 4.1.1). Using multiple time scale in Section 4.1.2, it is shown that, in the linear system, the plume motion is controlled by the slow advection process after the fast wave passed by. The total flow that advects the plume can be split into two distinct parts: a coastal mode and a gyre mode, corresponding to the direct forcing by the outflow and salinity variation, respectively. In Section 4.1.3, analytic solutions are obtained and the upstream motion is further explained. The variation of solutions with parameters is discussed in Section 4.1.4. Finally, the effect on upstream plume is inferred in Section 4.1.5 when a slanted density front between the plume and the oceanic water is allowed.

4.1.1 Typical solutions:

4.1.1.1 Nonlinear solution: A typical low- R_o ($R_o = 0.07$) solution is obtained when the parameter values listed in Table 1 are used. To illustrate the initial spin-up of the solution, the upper panel of Figure 8 plots v_1 and S_1 fields 4 days after the onset of outflow; in addition, Figure 9 shows latitude-time plot of \mathcal{P}_1 and S_1 at the coast. A Kelvin-wave front, excited at the onset, propagates along the downstream coast and nearly reaches the southern boundary after 4 days. Its propagation speed, as measured by the slope of the rise in $\mathcal{P}_1(0, y)$ in the left panel of Figure 9, is about 80 cm/s, consistent with the linear Kelvin-wave speed $\sqrt{g'_1 H_1} = 80$ m/s when g'_1 is evaluated using S_1^* and T_1^* . Behind the front, the rise in $\mathcal{P}_1(0, y)$ establishes a coastally-trapped southward, geostrophic current (upper panel of Figure 8), and its transport is the same as that of the outflow. This response is essentially the same as the one in constant-density layer models, such as the "coastal current" in Minato (1983) and Ikeda (1984), and the " K -mode" in Kubokawa (1991). The fresher-water plume itself, however, develops much more slowly at advective speeds. At day 4, only a small plume (shaded region), with a semi-closed anticyclonic gyre circulating about its edges, has formed near the river mouth.

The quasi-equilibrium response at day 40 is shown in the middle and lower panels of Figure 8. Remarkably, all the river water bends to flow along the upstream coast as it exits the river mouth. At the nose of the plume, the fresher water, together with some ambient sea water forms a return flow further offshore. This return flow circulates offshore from the river mouth, and then continues to flow southward along the downstream coast. In the upstream region, the front advances northward along the coast, at an average speed of 6.1 cm/s, as measured by the slope of the drop in S_1 on the upstream coast in the right panel of Figure 9. A region where h_1 is shallower than the initial layer thickness H_1 develops within the plume everywhere in the upstream region (shaded region in the lower panel of Figure 8). In the downstream region, the flow is uniformly to the south, and the plume is narrower and weaker than the upstream one.

Unstable waves with a wavelength of about 50 km develop on the offshore density front. The nature of this instability has not been identified, since it is not the major concern of this

Figure 8: A typical low- R_o solution for the nonlinear, variable-density, $1\frac{1}{2}$ -layer model, showing velocities \mathbf{v}_1 and salinities S_1 at day 4 (upper panel) and day 40 (middle panel) and h_1 at day 40 (lower panel). The contour interval for h_1 is 0.2 m, and regions where $h_1 < H_1$ (10 m) are shaded. Regions where $S_1 < 22.5$, $22.5 < S_1 < 25$ and $25 < S_1 < 29$ are indicated by dark, medium and light shading, respectively. All the river water first bends to the left to flow along the upstream coast. Near the plume nose, some fresher water turns around to flow, together with the some salty water, southward.

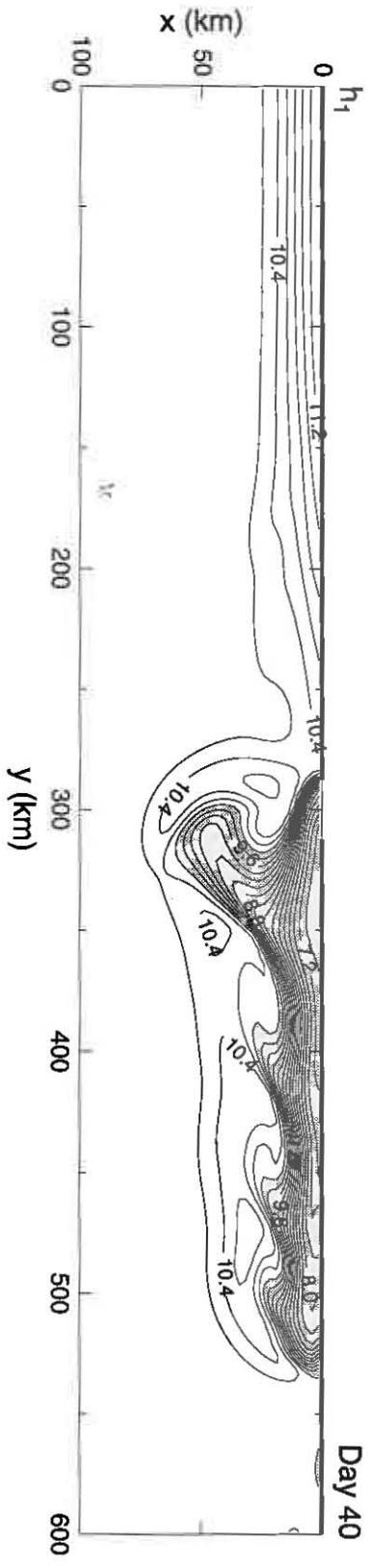
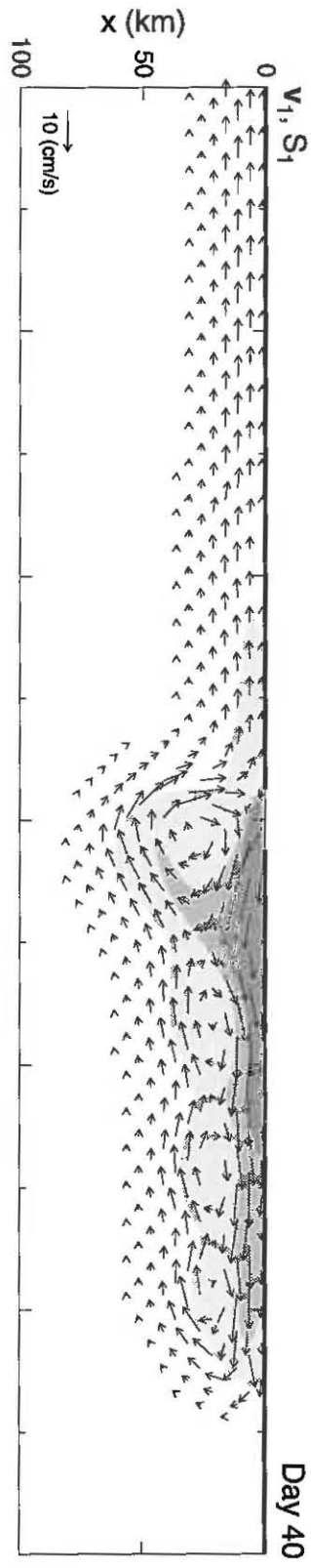
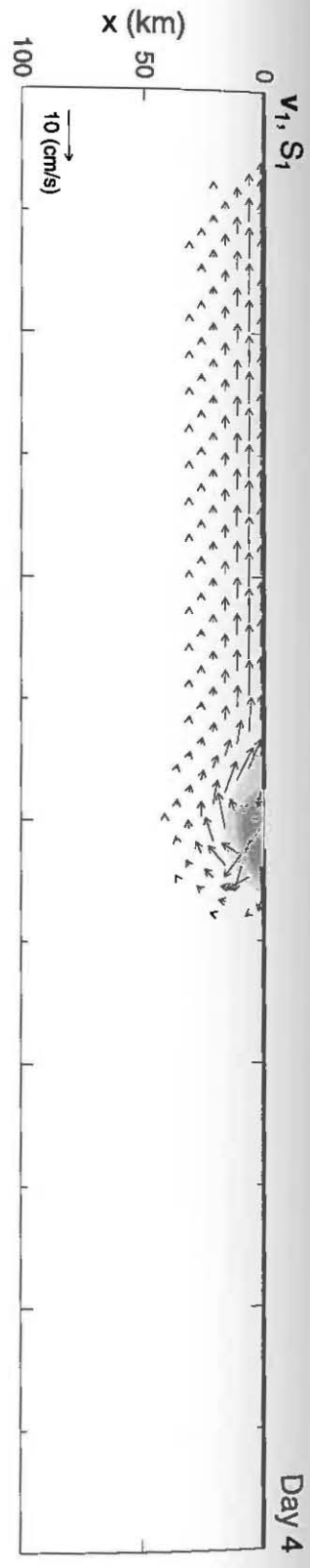
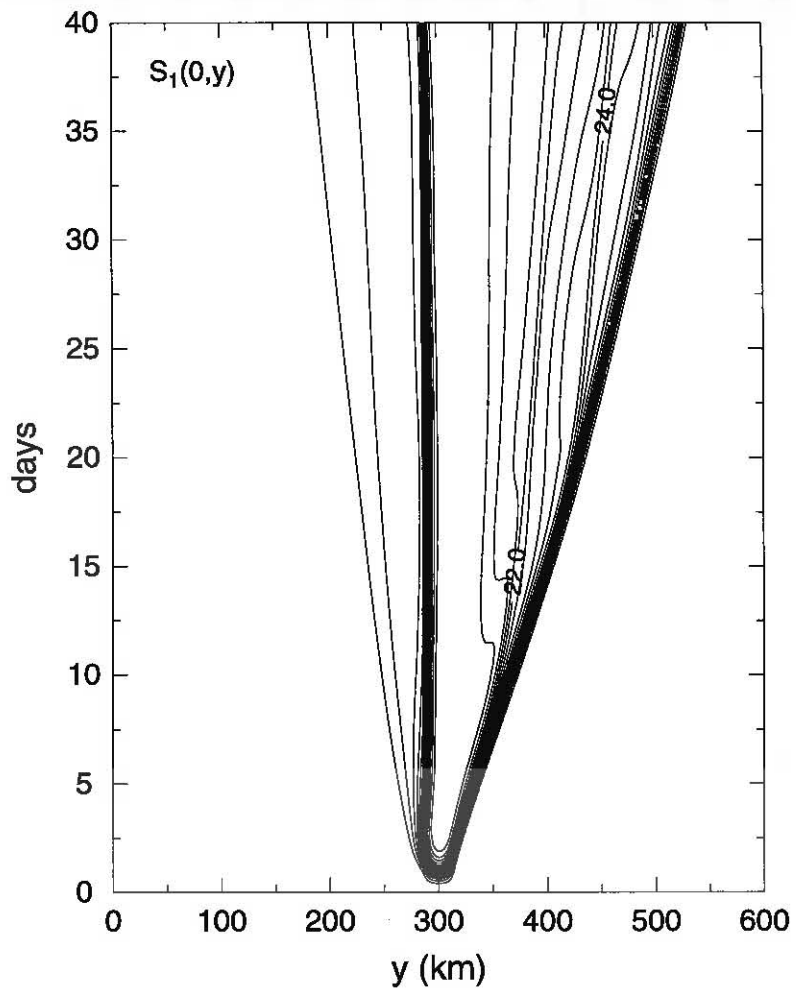
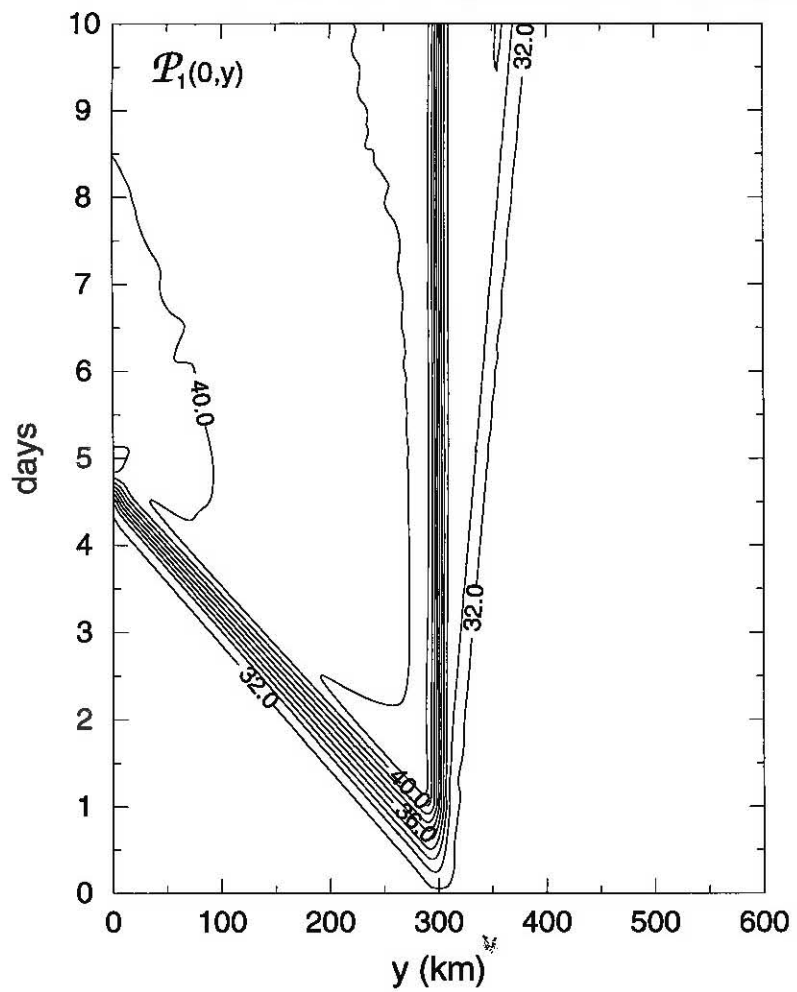


Figure 9: Latitude-time plots showing coastal depth-integrated pressure $\mathcal{P}_1(0, y)$ scaled by 10^5 (left panel), and salinity $S_1(0, y)$ (right panel) for the solution in Figure 8. Contour intervals are $10^5 \text{ cm}^3/\text{s}^2$ for \mathcal{P}_1 and 0.5 for salinity. In the downstream region, a coastal Kelvin wave propagates southward from the river mouth, generating a jump in \mathcal{P}_1 across the mouth and raising it everywhere along the downstream coast (left panel). The plume propagates northward at an average speed of 6.1 cm/s (right panel).



study; however, it is likely to be the same sort of instability discussed in Fukamachi *et al.* (1996), namely, the ageostrophic baroclinic instability. The unstable waves do not appear when the mixing coefficient ν is large enough; for instance, a value of ν equal to $5 \times 10 \text{ cm}^2/\text{s}$ is sufficient to eliminate them in this solution.

4.1.1.2 Linear solution: A solution to the linear system (6) is also obtained, and it is shown at day 40 in the upper and middle panels of Figure 10. Similar to the nonlinear solution in Figure 8, all the river water first bends to the left as it exits the river mouth, a return flow forms further offshore, h_1 shallows in the upstream plume region, and the plume advances along both coasts with the plume being narrower downstream than upstream. Note that in the upstream region the density front and its associated circulation are approximately parallel to the coast (y -independent) behind the upstream front. The primary difference from the nonlinear response is that the instability is eliminated. The strong similarity between linear and nonlinear solutions demonstrates that nonlinearities in the momentum equations are not fundamentally important for determining the plume evolution in the low- R_o regime.

4.1.2 Coastal mode and gyre mode: In this section, the fundamental processes are explored that determine plume evolution under approximation of quasi-geostrophy, which is the case for all low- R_o motion. As will be seen, the evolution of the river plume is determined by two dynamically distinct processes: a downstream coastal current (coastal mode) driven by the mass input and an anticyclonic circulation (gyre mode) driven by the variation of salinity.

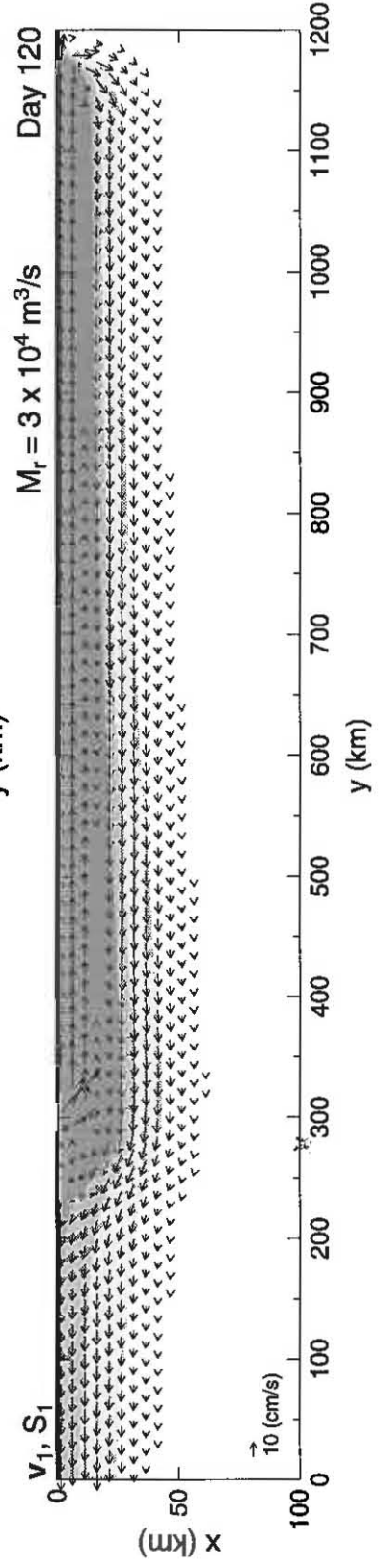
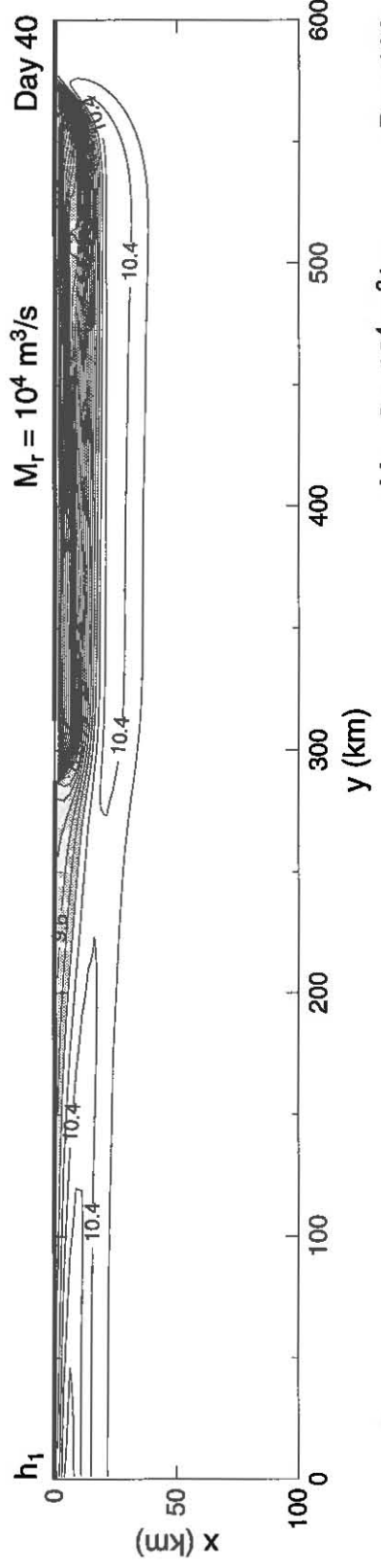
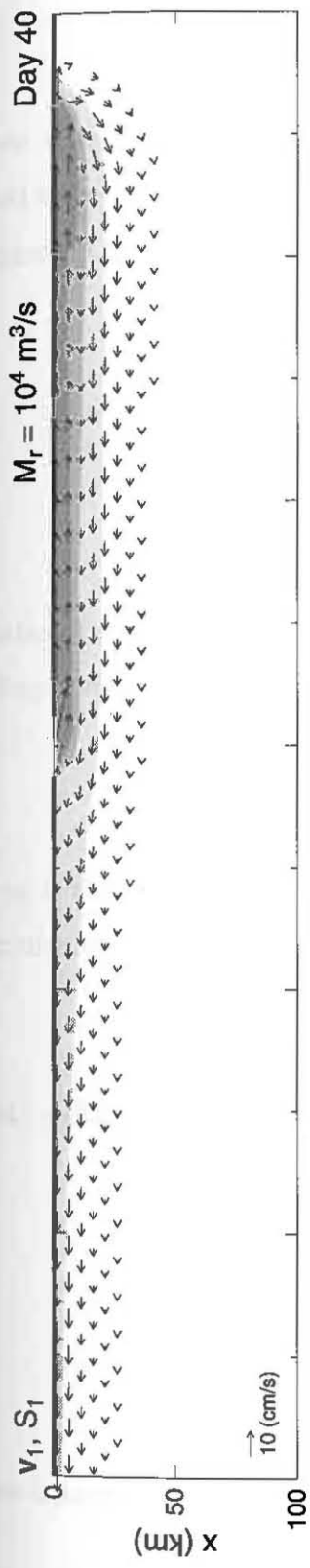
Let's begin by formally recognizing that there are two distinct time scales in system (6): $t' = O(1/f)$ associated with the geostrophic adjustment and the advection time scale $T = O(L/U)$, where L and U are characteristic scales of length and velocity. For low- R_o motion, $t'/T = R_o = U/(fL) \ll 1$, so that the advection is a much slower process than geostrophic adjustment. With this restriction, multiple time scales,

$$t' = t, \quad T \equiv R_o t, \quad (31)$$

are introduced, and fields are considered to depend explicitly on both variables,

$$q(x, y, t) = q(x, y, t'; T), \quad (32)$$

Figure 10: As in Figure 8, expect for solutions to the linear, variable-density, $1\frac{1}{2}$ -layer model. The three plots are v_1 and S_1 (upper panel) and h_1 (middle panel) at day 40 when $M_r = 10^4 \text{ m}^3/\text{s}$, and v_1 and S_1 at day 120 when $M_r = 3 \times 10^4 \text{ m}^3/\text{s}$ (lower panel). Note that, in the lower panel, the basin extends to $x = 1200 \text{ km}$. For the $M_r = 10^4 \text{ m}^3/\text{s}$ solution, the density front is nearly y -independent behind the nose in the upstream region. For the $M_r = 3 \times 10^4 \text{ m}^3/\text{s}$ solution, the plume is widest at the river mouth and becomes progressively narrower towards the nose.



where q can be any of the fields $\tilde{u}_1, \tilde{v}_1, \tilde{h}_1$ or \tilde{g}_1 . Time derivatives are then given

$$q_t = q_{t'} + R_o q_T, \quad (33)$$

by usual chain rule. An exception is that, since \tilde{g}'_1 is determined only by advection, it is assumed to be a function of only slow time so that $\tilde{g}'_{1t'} = 0$.

Expressed in terms of t' and T , equations (6) become

$$\tilde{u}_{1t'} + R_o \tilde{u}_{1T} - f \tilde{v}_1 + g'_0 \tilde{h}_{1x} + \frac{1}{2} H_1 \tilde{g}_{1x} = 0, \quad (34a)$$

$$\tilde{v}_{1t'} + R_o \tilde{v}_{1T} + f \tilde{u}_1 + g'_0 \tilde{h}_{1y} + \frac{1}{2} H_1 \tilde{g}_{1y} = 0, \quad (34b)$$

$$\tilde{h}_{1t'} + R_o \tilde{h}_{1T} + H_1 (\tilde{u}_{1x} + \tilde{v}_{1y}) = 0, \quad (34c)$$

$$R_o \tilde{g}'_{1T} + R_o (\tilde{u}_1 \tilde{g}'_{1x} + \tilde{v}_1 \tilde{g}'_{1y}) = 0. \quad (34d)$$

In equation (34d), the factor of the advection terms emerges as a result of scaling analysis. Boundary conditions are

$$\tilde{u}_1(0, y, t') = u_0(y) \theta(t), \quad (35a)$$

$$(\tilde{h}_1, \tilde{u}_1, \tilde{v}_1, \tilde{g}_1) \rightarrow (0, 0, 0, 0) \quad \text{as } x \rightarrow \infty, \quad (35b)$$

where u_0 is the offshore velocity at the river mouth.

Introducing the expansion,

$$\tilde{q}_1 = \tilde{q}_{10} + R_o \tilde{q}_{11} + O(R_o^2), \quad (36)$$

into (34) yields to lowest order

$$\tilde{u}_{10t'} - f \tilde{v}_{10} + g'_0 \tilde{h}_{10x} + \frac{1}{2} H_1 \tilde{g}_{10x} = 0, \quad (37a)$$

$$\tilde{v}_{10t'} + f \tilde{u}_{10} + g'_0 \tilde{h}_{10y} + \frac{1}{2} H_1 \tilde{g}_{10y} = 0, \quad (37b)$$

$$\tilde{h}_{10t'} + H_1 (\tilde{u}_{10x} + \tilde{v}_{10y}) = 0. \quad (37c)$$

$$\tilde{g}'_{10T} + \tilde{u}_{10} \tilde{g}'_{10x} + \tilde{v}_{10} \tilde{g}'_{10y} = 0. \quad (37d)$$

Because equations (37a)–(37c) are linear, it is possible to split \tilde{u}_{10} , \tilde{v}_{10} and \tilde{h}_{10} into two parts,

$$\tilde{q}_{10}(x, y, t'; T) = \tilde{q}_K(x, y, t'; T) + \tilde{q}_G(x, y; T), \quad (38)$$

such that variables with subscript K are those caused only by the volume transport of the outflow, and nothing to do with the salinity variations, whereas those with subscript G are caused only by the salinity difference. These two components are referred as the “coastal mode” and the “gyre mode”, respectively.

The coastal mode is determined by the equations

$$\tilde{u}_{Kt'} - f\tilde{v}_K + g_0'\tilde{h}_{Kx} = 0, \quad (39a)$$

$$\tilde{v}_{Kt'} + f\tilde{u}_K + g_0'\tilde{h}_{Ky} = 0, \quad (39b)$$

$$\tilde{h}_{Kt'} + H_1(\tilde{u}_{Kx} + \tilde{v}_{Ky}) = 0, \quad (39c)$$

subject to boundary condition

$$\tilde{u}_K(0, y, t') = u_0(y)\theta(t'). \quad (40)$$

Equations (39) and (40) describe the adjustment to a mass inflow when the density is the same as that of oceanic layer; it takes place in a time scale of $O(f^{-1})$. They are the same set of equations as for Minato's (1983) model-B and Kubokawa's (1991) K -mode. As shown in Minato's analytic results, the response of this mode features the propagation of a transient coastal Kelvin wave, and after its passage, a steady geostrophic flow is established along the downstream coast. The nonlinear, viscid version of this coastal-mode solution also appeared in the nonlinear numerical solutions discussed earlier in this chapter (upper panel of Figure 8, Figure 9). Here, a solution of the coastal mode is obtained by numerically integrating system (39) when an outflow of $M_r = 10^4 \text{ m}^3/\text{s}$ and $S_r = S_1^* = 30$ is prescribed at the river mouth, and the day 40 response is shown in the upper panel of Figure 11a which is considered $t' \rightarrow \infty$. This solution is consistent with the aforementioned studies of Minato (1983) and Kubokawa (1991).

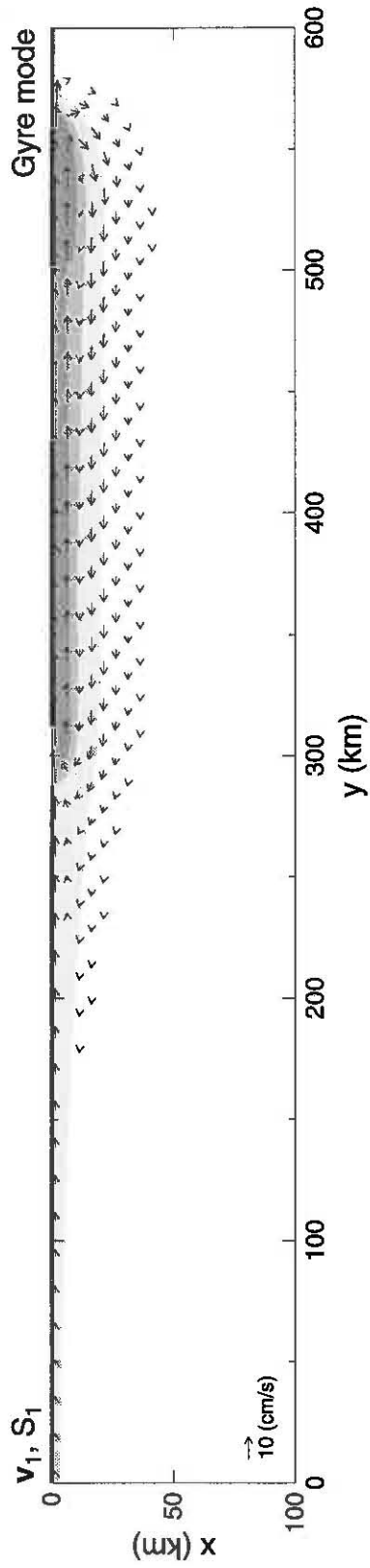
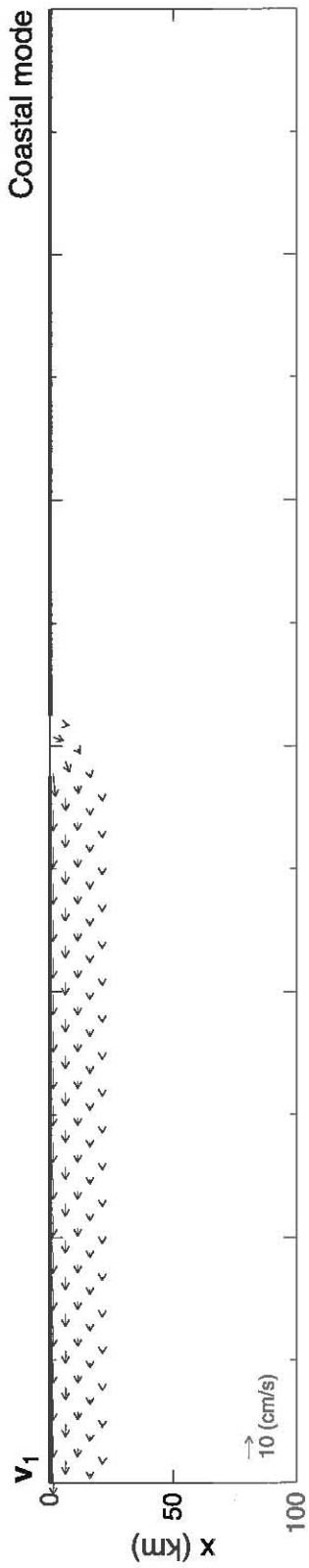
The gyre mode is governed by equations

$$-f\tilde{v}_G + \Phi_x = 0, \quad (41a)$$

$$f\tilde{u}_G + \Phi_y = 0, \quad (41b)$$

$$H_1(\tilde{u}_{Gx} + \tilde{v}_{Gy}) = 0, \quad (41c)$$

Figure 11a: As in Figure 8, except showing v_1 for the coastal mode (upper panel), v_1 and S_1 for the gyre mode (lower panel). The salinity field of day 40 solution (upper panel of Figure 10) in the linear model is used to obtain the gyre mode.



$$\tilde{g}'_{10T} + (\tilde{u}_K + \tilde{u}_G)\tilde{g}'_{10x} + (\tilde{v}_K + \tilde{v}_G)\tilde{g}'_{10y} = 0, \quad (41d)$$

subject to boundary condition

$$\tilde{u}_G = \Phi_y = 0 \quad @ \quad x = 0, \quad (42)$$

where in this case $\Phi = g'_0 \tilde{h}_G + \frac{1}{2} H_1 \tilde{g}'_{10}$. Note that even though the velocity is in geostrophic balance with the pressure, the system experiences constant evolution due to the advection of \tilde{g}'_{10} . Equation (41d) is essentially the same as the one that determines the evolution of the low-potential-vorticity water in Kubokawa's (1991) study.

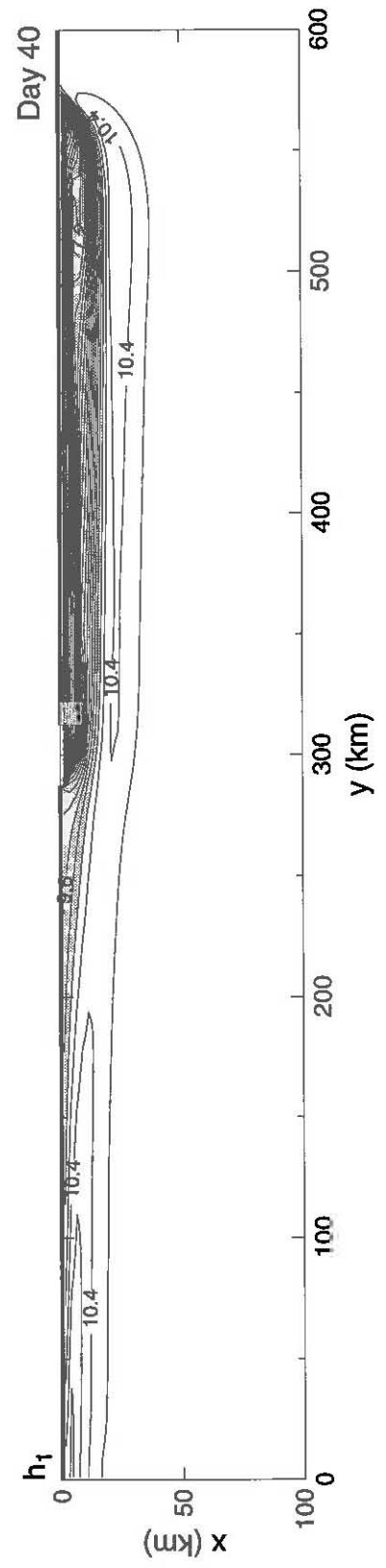
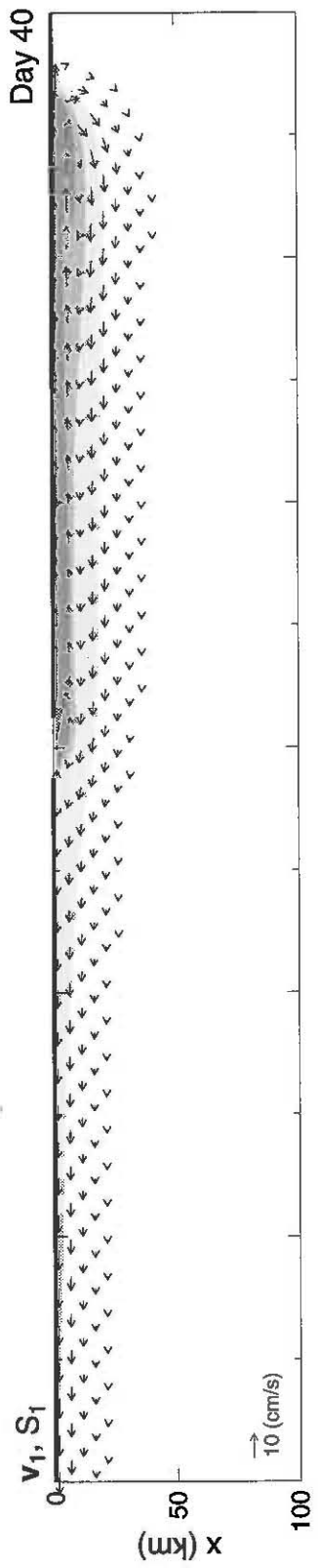
To obtain the gyre-mode solution, equation (41d) is numerically integrated forward in time with a time step of 0.5 day, which is small enough to resolve plume advection. Throughout the integration, velocities \tilde{u}_K and \tilde{v}_K are taken to be those shown in the upper panel of Figure 11a since the coastal-mode solution reaches a steady state after the passage of Kelvin wave (and hence t' is effectively ∞). Velocities \tilde{u}_G and \tilde{v}_G are determined at the beginning of each time step from equations (41a)–(41c) and boundary condition (42). The three equations yield equation (19) with $\tilde{q}_1^* = 0$, and the boundary condition is equivalent to $\Phi = 0$ which is applied at all channel boundaries. This system is then solved for Φ by a standard S.O.R. method. The lower panel of Figure 11a shows the resulting gyre-mode response at day 40.

The complete solution, that is, a superposition of the panels in Figure 11a, is shown in Figure 11b.

A comparison of this solution with the one obtained by numerically integrating equation (6) (upper and middle panel of Figure 10) shows good agreement, demonstrating that the separation of the response into coastal and gyre modes is dynamically correct and useful. Note that the coastal mode is responsible for all downstream flow along the coast, since the coastal current is directed upstream everywhere for the gyre mode (lower panel of Figure 11a). In contrast, the gyre mode is responsible for all upstream motion, since there is no northward alongshore current associated with the coastal mode (upper panel of Figure 11a).

Properties of the linear solution have a lot in common with those in Kubokawa's (1991) solution (compare our Figure 10 with his Figure 5b). This is not surprising, because the governing equations for plume evolution have similar forms in each system, being advection

Figure 11b: As in Figure 8, except showing \mathbf{v}_1 and S_1 (upper panel) and h_1 (lower panel) for the quasi-geostrophic solution at day 40. The solution is essentially the same as the linear solution in the upper two panels of Figure 10.



of salinity in this study and potential vorticity anomalies in his study [compare equation (41d) with his (2.12)]. Moreover, the coastal modes in the two models are identical, both being linear responses to the transport of the river outflow; the gyre modes are similar in the two models, with the salinity anomaly in this model being analogous to the low potential-vorticity anomaly in his model.

4.1.3 Analytic solutions: Based on the structure of the circulation in Figure 10, quasi-equilibrium solutions in the low- R_o regime can be characterized by the schematic diagram in Figure 12. In the upstream region, the plume nose continues to propagate northward at speed c with a shape that does not change in time. Behind the nose, the density front is y -independent and has reached a steady state at $x = L$. The current is northward near the coast and southward offshore along the density front. In the downstream region, the flow pattern is the same as the part with southward flow in the upstream region. (There is also a plume nose in the downstream region, but it is not considered in this thesis.) Given this simple structure, it is possible to solve for the across-shore structure of the flow in both upstream and downstream regions, and to determine L and c as a function of model parameters. The discussion begins by considering two geostrophic adjustment problems of idealized plume shapes, and then the connection is made between these solutions with the river-outflow-driven circulations.

4.1.3.1 Coastal front: Consider a similar situation to the one discussed in Section 3.2, except that the density front¹ is at $x = L$ and there is a lateral wall at $x = 0$. The solution can be obtained in the same manner, but in this case, the boundary condition $v_1(0, y) = 0$ at the wall is also imposed, which in terms of h_1 is

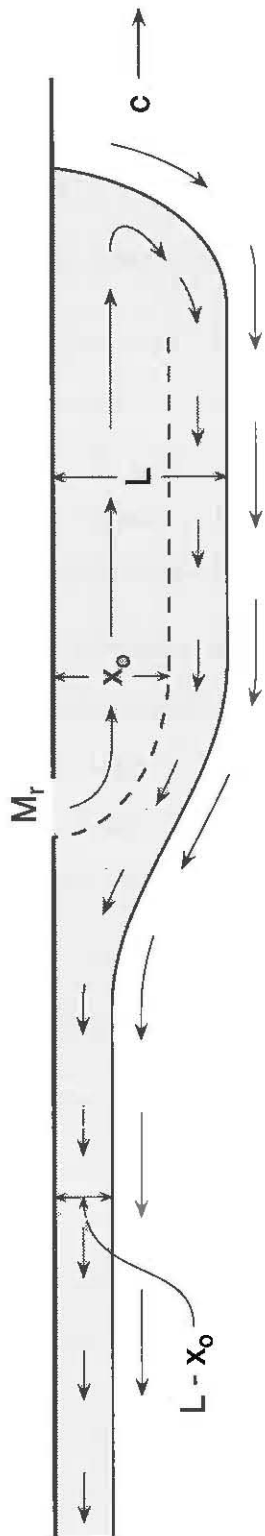
$$(h_-)_x = 0 \quad @ \quad x = 0. \quad (43)$$

This constraint follows from the momentum balance, $dv_1/dt + fu_1 = 0$, and the closed condition $u_1(0, y) = 0$. The resulting solution is

$$h_- = H_1 \left\{ 1 + \frac{1-\gamma}{2} \left[-e^{(x-L)/R_-} - e^{-L/R_-} e^{-x/R_-} \right] \right\}, \quad (44a)$$

¹Strictly speaking, mass conservation requires that the final location of the front is shifted slightly toward the salty-water region from its initial position (Glendening, 1993). For our purposes, it is not necessary to calculate this shift.

Figure 12: Schematic diagram of the analytic solution driven by river outflow. River water with a transport of M_r bends to the left as it exits the river mouth, and a coastally trapped plume advances northward at speed c . Some of the river water, together with some salty water, returns from near the plume nose to flow southward along the front, and this return flow eventually flows along the downstream coast. The thick curve indicates the plume edge, and the dashed curve designates where the current reverses direction. The solution is y -independent away from the nose and the river mouth. In the upstream region the response is solution (50) with $M = M_r$. In the downstream region it is (50) with the replacement $x \rightarrow x + x_0$. Widths L and x_0 are provided in equations (54) and (51).



24

$$h_+ = H_1 \left\{ 1 + \frac{1-\gamma}{2\gamma} [e^{-(x-L)/R_+} + e^{-2L/R_-} e^{-(x-L)/R_+}] \right\}, \quad (44b)$$

and the corresponding alongfront, geostrophic currents, v_- and v_+ , are

$$v_- = c_- \frac{1-\gamma}{2} [-e^{(x-L)/R_-} + e^{-L/R_-} e^{-x/R_-}], \quad (45a)$$

$$v_+ = c_- \frac{1-\gamma}{2} [-e^{-(x-L)/R_+} + e^{-2L/R_-} e^{-(x-L)/R_+}]. \quad (45b)$$

The first term in each of the solutions (44) and (45) corresponds to unbounded solution (25); the second term is due to the existence of the boundary, and is generated by the radiation of gravity waves from the coast. In spite of the presence of the coastal boundary, this solution has similar properties to its unbounded counterpart. In particular, a frontally trapped southward current is generated everywhere in both fresher and salty water regions.

4.1.3.2 Nose front: Now let's consider what happens when a northern end is added. At the plume nose, geostrophic adjustment generates a current that tends to draw water *away* from the coast. However, the presence of the coast does not permit normal flow, and therefore h_1 has to thin. This thinning signal radiates down the coast as a Kelvin wave, and h_1 is thinner everywhere near the coast after its passage. To a good approximation, the following boundary condition results

$$\frac{1}{2}g'_- h_-^2 = \frac{1}{2}g'_+ H_1^2 \quad @ x = 0. \quad (46)$$

Condition (46) follows from an integration of the time-independent version of alongshore component of equation (1a) along the coast when the second term is neglected, which is reasonable for low- R_o motion.

It is convenient to represent the solution as the sum of the y -independent response (44) and a free solution generated by the Kelvin wave. The free solution is

$$h'_- = \mathcal{H}e^{-x/R_-}, \quad h'_+ = \mathcal{H} \frac{1}{\gamma} e^{-L/R_-} e^{-(x-L)/R_+}, \quad (47)$$

where \mathcal{H} is its amplitude. It is a solution to the homogeneous version of equation (23) that decays as $x \rightarrow \infty$ and satisfies matching conditions (24). Application of boundary condition (46) to the superposition of h'_- from (47) and (44a) yields,

$$\mathcal{H} = -H_1(1-\gamma)\chi, \quad (48)$$

where $\chi = 1 - e^{-L/R_-}$. Equation (48) means that the Kelvin wave acts to thin the layer thickness.

The h_1 field is then

$$h_- = H_1 \left\{ 1 + \frac{1-\gamma}{2} [-e^{(x-L)/R_-} - e^{-L/R_-} e^{-x/R_-} - 2\chi e^{-x/R_-}] \right\}, \quad (49a)$$

$$h_+ = H_1 \left\{ 1 + \frac{1-\gamma}{2\gamma} [e^{-(x-L)/R_+} - e^{-2L/R_-} e^{-(x-L)/R_+} - 2\chi e^{-L/R_-} e^{-(x-L)/R_+}] \right\}, \quad (49b)$$

and, by geostrophy, the v_1 field is

$$v_- = c_- \frac{1-\gamma}{2} [-e^{(x-L)/R_-} + e^{-L/R_-} e^{-x/R_-} + 2\chi e^{-x/R_-}], \quad (50a)$$

$$v_+ = c_- \frac{1-\gamma}{2} [-e^{-(x-L)/R_+} + e^{-2L/R_-} e^{-(x-L)/R_+} + 2\chi e^{-L/R_-} e^{-(x-L)/R_+}]. \quad (50b)$$

The last terms on the right-hand sides of equations (49) and (50) are the contributions from the Kelvin-wave radiation, and they act to reverse the flow to be northward near the coast through the thinning of h_1 .

Since there is southward flow near the offshore density front, the coastal current changes its direction somewhere offshore west of the front. This location is

$$x_0 = \frac{1}{2} R_- \ln (2e^{L/R_-} - 1), \quad (51)$$

which follows from setting $v_-(x_0) = 0$ in equation (50a). According to (51), x_0 satisfies the inequality $\frac{1}{2}L \leq x_0 \leq L$, the lower and upper limits being approached as $L \rightarrow \infty$ and $L \rightarrow 0$, respectively. The total upstream transport of fresher water is therefore

$$M = \int_0^{x_0} h_- v_- dx = \frac{1}{f} [\mathcal{P}_1(x_0, y) - \mathcal{P}_1(0, y)] = \frac{1}{2f} [g'_- h_-^2(x_0, y) - g'_+ H_1^2], \quad (52)$$

where boundary condition (46) has been utilized.

4.1.3.3 Identification with river-outflow-driven circulations: To identify the above solution with the river-outflow-driven circulation depicted in Figure 12, simply sets M in equation (52) equal to the transport of river outflow M_r . An inherent assumption in making this identification is that the river outflow has the same uniform potential vorticity f/H_1 as the surrounding water. This assumption ignores both the relative vorticity of the outflow and the property that h_1 thickens southward across the river mouth. Because R_o is

small, however, potential vorticity remains close to f/H_1 , and the assumption is a reasonable one. (See the discussion at the end of Section 4.1.4.)

According to (52), M decreases to zero in the limit $L \rightarrow 0$ when the response to the density front and Kelvin wave completely overlap, and increases to a maximum value

$$M_{cr} = \frac{1}{2f} (g'_- - g'_+) H_1^2 \equiv \frac{g\alpha_S}{2f} (S_1^* - S_r) H_1^2 \quad (53)$$

as $L \rightarrow \infty$ when they are completely separate and hence $h_-(x_0, y) \rightarrow H_1$. The existence of M_{cr} shows that there is an upper limit for the outflow transport beyond which the equilibrium state shown in Figure 12 cannot be attained; in this regime, the density front must instead continue to expand offshore.

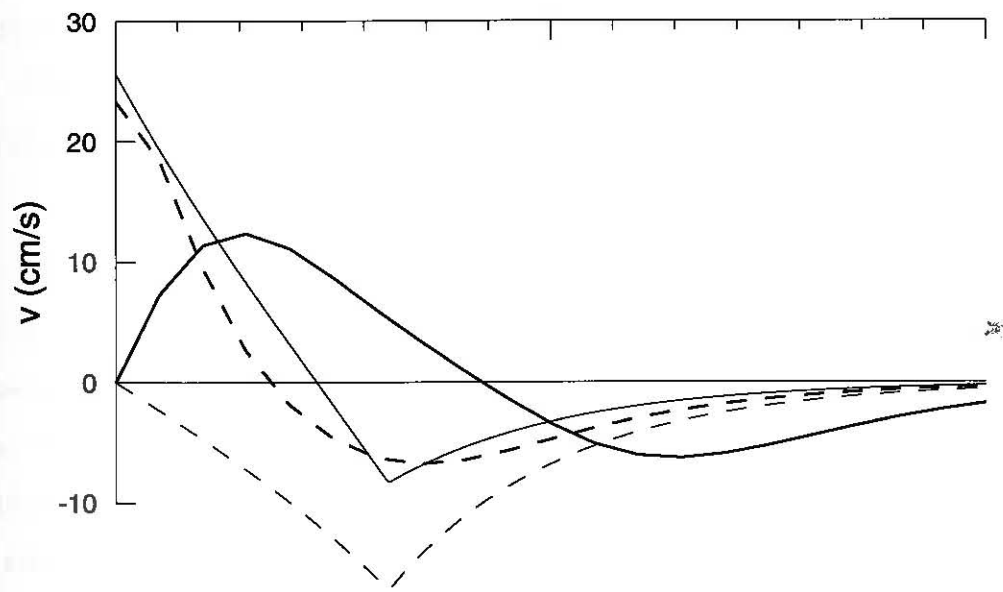
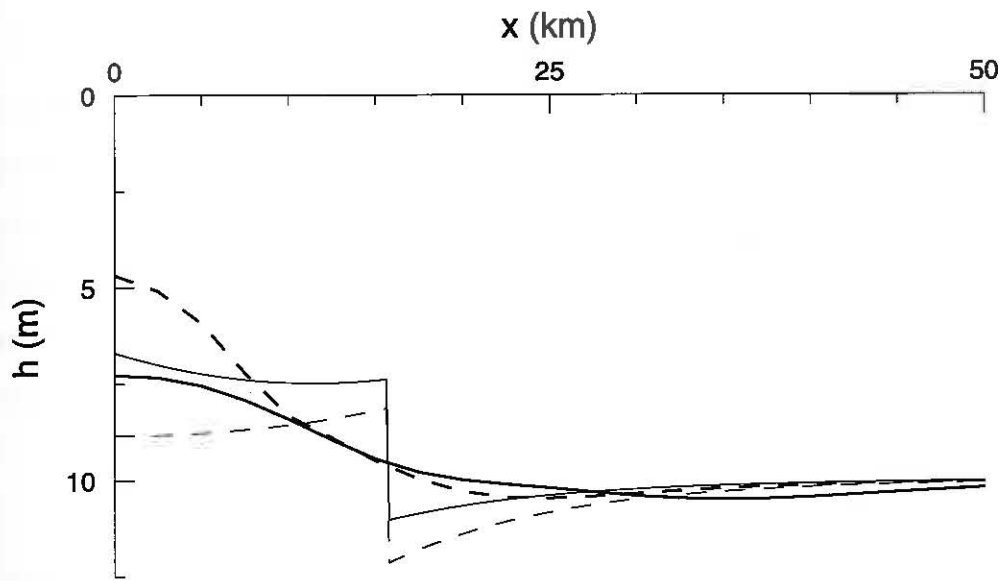
Solutions (49) and (50) are plotted in Figure 13, when parameter values are those from Table 1. A comparison with their y -independent counterparts (44) and (45), plotted in the same figure, illustrates the role of the transient Kelvin wave in thinning h_1 and reversing the flow near the coast. Also plotted in the same figure are the nonlinear and linear solutions driven by river outflow shown in Figures 8 and 10, respectively. For the linear solution, the section was taken at $y = 400$ km. For the nonlinear solution, the average for a single wavelength (from $y = 400$ km to 460 km) are adopted. The h_1 fields from the numerical solution and analytic solution agree in that they all are shallower near the coast. Differences are that: 1) there is a discontinuity across the density front for analytic solution; and 2) h_1 is thinner near the coast for the linear solution. The latter is because the linearized version of coastal condition (24), $g_0 \tilde{h}_1 + \frac{1}{2} \tilde{g}_1 H_1 = 0$, is established in the linear solution. The v_1 field of the numerical linear solution compares well everywhere with the analytic one. In contrast, the structure of the nonlinear solution is altered considerably because it includes horizontal mixing and utilizes a no-slip coastal boundary condition.

4.1.3.4 Plume width: Equation (52) can be rewritten as $h_-(x_0, y)/H_1 = \eta$ if $M = M_r$, where $\eta = \sqrt{\phi(1 - \gamma^2) + \gamma^2}$, and $\phi = M_r/M_{cr}$. With the aid of equations (49) and (51), it can then be shown that

$$\frac{L}{R_-} = \cosh^{-1} \left(\frac{1 - \gamma}{1 - \eta} \right) + \ln \left(\frac{1 - \gamma}{1 - \eta} \right), \quad (54)$$

Figure 13: As in Figures 5 and 6, expect showing the acrossfront h_1 and v_1 fields in the upstream region for analytic (thin curves), nonlinear (thick curves) and linear (thick-dashed curves) solutions driven by a river outflow. For the linear solution, the section is taken at day 40 and at $y = 400$ km; for the nonlinear solution, the fields are taken at day 40 and are averaged over one wavelength (from $y = 400$ km to 460 km) of the unstable wave (see Figure 8). Also shown is the analytic solution (44) and (45), the y -independent solution that results from geostrophic adjustment to a density front at $x = L$ (thin dashed curve). This solution represents the response in the analytic river model before the Kelvin wave arrives from the nose region, and has southward flow throughout the entire region. A comparison of this solution with the corresponding river-outflow-driven solution (thin curves) shows that the Kelvin wave thins the layer and reverses the flow to the northward near the coastal wall.

25



where the first term on the right-hand side is x_0/R_- and the second is $(L - x_0)/R_-$. Note that L/R_- depends only on two independent non-dimensional variables, ϕ and γ .

4.1.3.5 Nose propagation speed c : To obtain an expression for the nose propagation speed c , imagine a rectangular box in a reference frame moving with the nose with its northern edge ahead of the nose, southern edge in the y -independent region behind it, western edge at $x = 0$, and eastern edge at the far channel wall (essentially $x = \infty$). Since there is no change in the amount of fresher water within this box, an integration of the h_1 equation in the moving reference frame over the fresh-water region yields

$$\int_0^L h_- v_- dx - c \int_0^L h_- dx = 0, \quad (55)$$

Likewise, applying the same argument to the salty water yields

$$\int_L^\infty h_+ v_+ dx = -c \left[\int_0^L H_1 dx + \int_L^\infty (H_1 - h_1) dx \right]. \quad (56)$$

Equation (56) points toward the importance of the southward transport of salty water in the plume dynamics. Because of this flow, salty water is continuously depleted from the upstream region, and mass conservation then requires that the plume propagates northward to replace this loss. With the relation $\int_0^L h_- v_- dx = (g_-'/2f) [h_-(L, y) - \gamma H_1] [h_-(L, y) + \gamma H_1]$ and solution (49), direct calculation of c from (55) gives

$$\frac{c}{\Delta c} = \frac{\chi^2 [\gamma + \frac{1}{4}\chi^2(1 - \gamma)]}{2L/R_- - (1 - \gamma)\chi(2 + \chi)}, \quad (57)$$

where $\Delta c = \sqrt{g_- H_1} - \sqrt{g_+ H_1}$. Like L/R_- , $c/\Delta c$ also depends only on ϕ and γ .

At this point, the analytic solution in the upstream region is completed. From its derivation, it is clear that two key processes are involved in upstream plume propagation: geostrophic adjustment across the density front drives the return flow, and Kelvin-wave adjustment causes upstream flow near the coast. Another property illustrated by the analytic solution is that the plume width L increases monotonically with M_r until it reaches a critical value M_{cr} beyond which a steady-state solution is no longer possible.

4.1.3.6 Downstream solution: To find solutions in the downstream region, the coastal condition $\mathcal{P}_1(0, y') = \mathcal{P}_1(0, y) + fM_r$ is utilized, where y' and y denote any location

just downstream and upstream of the river mouth, respectively, which follows from the property that the outflow adjusts to geostrophic balance. In addition, the relation $\mathcal{P}_1(x_0, y) = \mathcal{P}_1(0, y) + fM_r$ follows from geostrophy and the fact that the upstream transport between the coast and $x = x_0$ is M_r . Therefore,

$$\mathcal{P}_1(0, y') = \mathcal{P}_1(x_0, y). \quad (58)$$

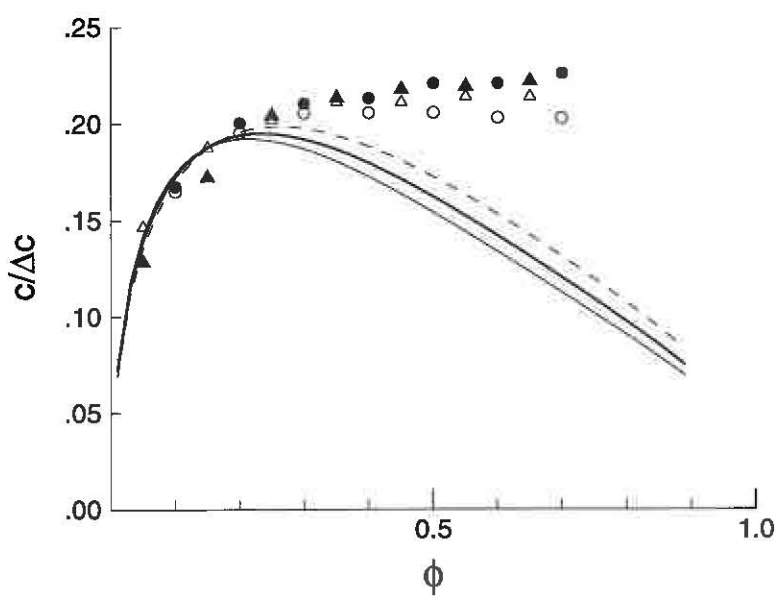
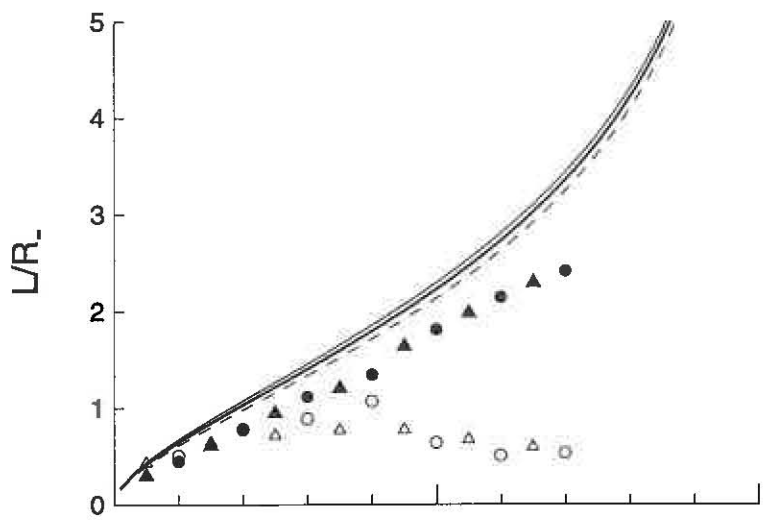
It follows that the flow field in the downstream region is identical to the upstream solution from $x = x_0$ to infinity; hence, simply replacing x in equations (49) and (50) by $x_0 + x$ gives the solution in the downstream region.

A comparison of numerical solutions with analytic ones in this region shows considerable difference. This is because the plume width is much narrower ($L - x_0 = 3.5$ km) than its upstream counterpart, and hence it is difficult for the numerical solutions to resolve.

4.1.4 Parameter variation (L and c curves): Figure 14 plots L/R_- (upper panel) and $c/\Delta c$ (lower panel) versus ϕ for $\gamma = 0.59, 0.67$ and 0.79 (thin, thick and dashed curves, respectively) as calculated from equations (54) and (57), which correspond to salinities $S_r = 15, 20$ and 25 , respectively. The dependence of both L/R_- and $c/\Delta c$ on γ is weak in this parameter range. The L/R_- curves increase monotonically from zero to ∞ as ϕ varies from 0 to 1, and (54) is no longer meaningful for $\phi > 1$ because in that case $\eta > 1$. (In Kubokawa's, 1991, study, a similar criterion exists that divides the solutions into a steady and non-steady modes.) The $c/\Delta c$ curves first increase with ϕ but eventually decrease to 0 because $L/R_- \rightarrow \infty$ as $\phi \rightarrow 1$.

Figure 14 also plots data points of L/R_- and $c/\Delta c$ determined from solutions to the linear (solid symbols) and nonlinear (open symbols) numerical models when $\gamma = 0.67$. (Data points for other values of γ are close to those shown, differing in a manner consistent with the shifts in the analytic curves.) The plotted points are obtained from two sequences of solutions in which M_r is varied and H_1 is either 10 m (circles) or 7.5 m (triangles). Width L is defined by the offshore location of the $(S_r + S_1^*)/2$ salinity contour. For the linear solutions, L is measured by the width of the y -independent region that forms behind the nose when $\phi \lesssim 0.4$ (upper panel of Figure 10); it is the maximum frontal width just upstream from the river

Figure 14: Plots of L/R_- (upper panel) and $c/\Delta c$ (lower panel) versus ϕ . The three curves are determined from the analytic expressions (54) and (57) where $\gamma = 0.59, 0.67$ and 0.79 (thin, thick and dashed curves, respectively), which correspond to salinities $S_r = 15, 20$ and 25 , respectively. Data points are obtained from two sequences of the linear (solid symbols) and nonlinear (open symbols) solutions in which M_r is varied and H_1 is 10 m (circles) for one and 7.5 m (triangles) for the other when $\gamma = 0.67$. In the L/R_- plot, data points from the linear solutions closely follow the analytic curve, but those from the nonlinear solutions deviate markedly for $\phi \gtrsim 0.2$ since then the river water first flows offshore. In the $c/\Delta c$ plot, data points lie above the analytic curves for $\phi \gtrsim 0.4$ because the fronts are narrower near the nose than predicted analytically.



mouth when $\phi \gtrsim 0.4$ (lower panel of Figure 10). For the nonlinear solutions with unstable waves, L is the average value over an integral number of wavelengths in a region between the nose and the river mouth. Speeds c are determined from $y-t$ plots (like right panel of Figure 9) of $S_1(0, y)$, by measuring the slope of the upstream isohalines during the first 10 days of the integration. For the linear solutions this slope remains unchanged throughout the integration, but for the nonlinear solutions it decreases slightly because S_1 rises at the coast due to horizontal mixing.

Data points of L/R_* from the linear solutions compare well with the analytic curves, confirming that the two models share a common dynamics. In contrast, points from the nonlinear solutions compare well only for $\phi \lesssim 0.2$. They differ markedly at higher ϕ values because the structure of the nonlinear response changes completely, with all the river water first flowing directly offshore (see Figure 15 below). Data points of $c/\Delta c$ from the nonlinear solutions compare well with the analytic curve for $\phi \lesssim 0.2$, but they are somewhat smaller for the linear solution in this parameter range. For larger values of ϕ , $c/\Delta c$ points from both the nonlinear and linear solutions lie above the analytic curve because the frontal width near the plume nose does not continue to increase (lower panels of Figure 10).

It has been assumed in the analytic model that the river water has uniform potential vorticity f/H_1 . However, the boundary condition at the river mouth (15) for the numerical model does not necessarily satisfy this requirement. Nevertheless, the analytic solutions compare well with the numerical ones, suggesting that the solutions are not sensitive to the potential vorticity anomaly in low- R_* regime. To confirm this statement, $Y(y)$ in equation (16) is replaced by either of the linear ramp functions, $Y_{\pm} = [1 \pm 2(y - \bar{y})/W]/W$, therefore the potential vorticity associated with this shear is also changed. The results, however, are not changed significantly. The reason for this insensitivity is that the potential-vorticity anomaly (relative to its undisturbed background value f/H_1) due to the shear flow at the river mouth is overwhelmed by the equivalent potential-vorticity anomaly due to the density effect as indicated by equation (22). For example, the shear flow contributes to a potential-vorticity anomaly of $(2M_r/HW^2 f)(f/H_1)$, which yields $0.04(f/H_1)$ when the parameters in Table 1 are used. In contrast, the contribution from the density effect is $(\tilde{q}_1^*/f)(f/H_1) = 0.6(f/H_1)$.

4.1.5 Inferences from the slanted-front solution: In the preceding low- R_o solution, the dominant feature is that river water flows predominantly along the upstream coast. As demonstrated by our analytical solution, the upstream speed is related to the southward return flow of the salty water, which is generated by geostrophic adjustment across the front [see equation (56)]. As discussed in Section 3.3, the southward salty-water flow is much less when the density front is allowed to slant. This difference may suggest that the plume will propagate upstream much more slowly in a system that allows slanted fronts. Unfortunately, the y -independent slanted-front in Section 3.3 can not be extended to include a nose front (because it is unclear how to impose the coastal boundary condition), and so this possibility can not be checked.

4.2 High- R_o solutions

4.2.1 Typical solutions: Figure 15 shows day-40 solutions to the nonlinear numerical model for the outflow transports $M_r = 3, 5$ and $8 \times 10^4 \text{ m}^3/\text{s}$, which correspond to Rossby numbers $R_o = 0.21, 0.33$ and 0.53 , respectively. A common feature in these solutions is that the river water flows directly offshore from the river mouth in a narrow jet, with anticyclonic and cyclonic eddies developing on its southern and northern sides. Note that the angle at which the jet leaves the river mouth is sensitive to M_r , with the jet bending more to the south as M_r is increased. The transition from a coastally trapped to an offshore-jet response is visible in Figure 14 in that the data points for the nonlinear solutions begin to deviate abruptly from the linear ones when $\phi \gtrsim 0.4$ (also compare the structures of the solutions in Figure 8 and the upper panel of Figure 15 for which $\phi = 0.2$ and 0.6 , respectively).

Similar changes occur when M_r is fixed at $10^4 \text{ m}^3/\text{s}$ and either H_1 or $\Delta S = S_1^* - S_r$ is decreased, since a decrease in these variables raises ϕ and R_o (in the case of H_1). Figure 16 shows a sequence of solutions when $H_1 = 5.5, 4,$ and 3 m for which $R_o = 0.13, 0.18,$ and 0.23 . With these choices, the structures of the solutions, including the jet angles, are similar to those in the corresponding panels of Figure 15.

4.2.2 Dynamics: It is hypothesized that the formation of the offshore jet is due to the momentum-advection terms since it does not develop in the low- R_o solutions. To demonstrate

Figure 15: As in Figure 8, except showing v_1 and S_1 of the high- R_o solutions to the nonlinear model when $M_r = 3 \times 10^4 \text{ m}^3/\text{s}$ (upper panel), $5 \times 10^4 \text{ m}^3/\text{s}$ (middle panel) and $8 \times 10^4 \text{ m}^3/\text{s}$ (lower panel), which correspond to $R_o = 0.21, 0.33$ and 0.53 , respectively. To illustrate the downstream flow field better, the river mouth is shifted northward to $\bar{y} = 400 \text{ km}$. The solutions differ from the low- R_o solution in Figure 8 in that all the river water first flows directly offshore from the river mouth, with only a portion eventually recirculating to form an upstream plume. The offshore jet bends more to the south as M_r increases.

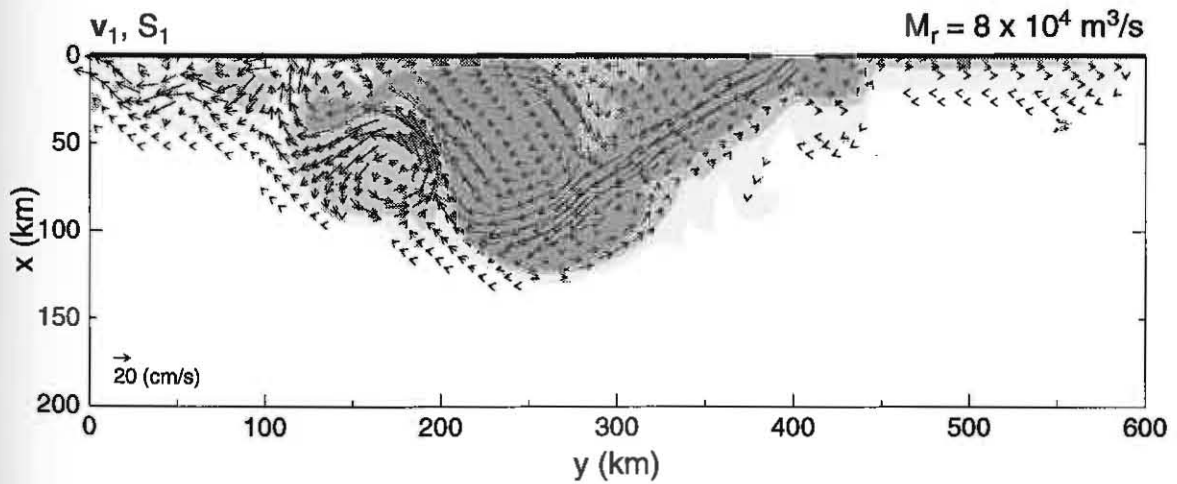
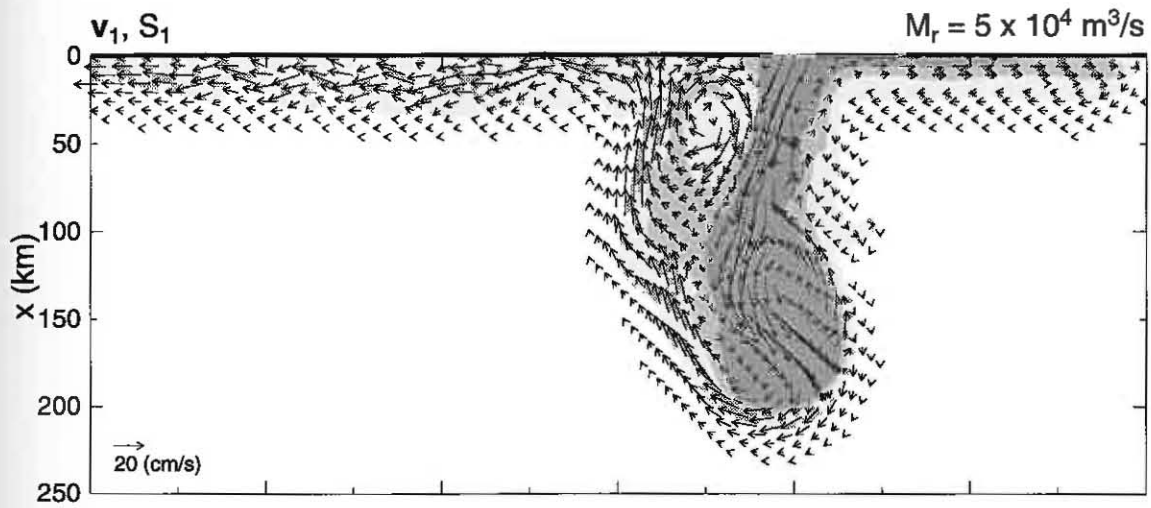
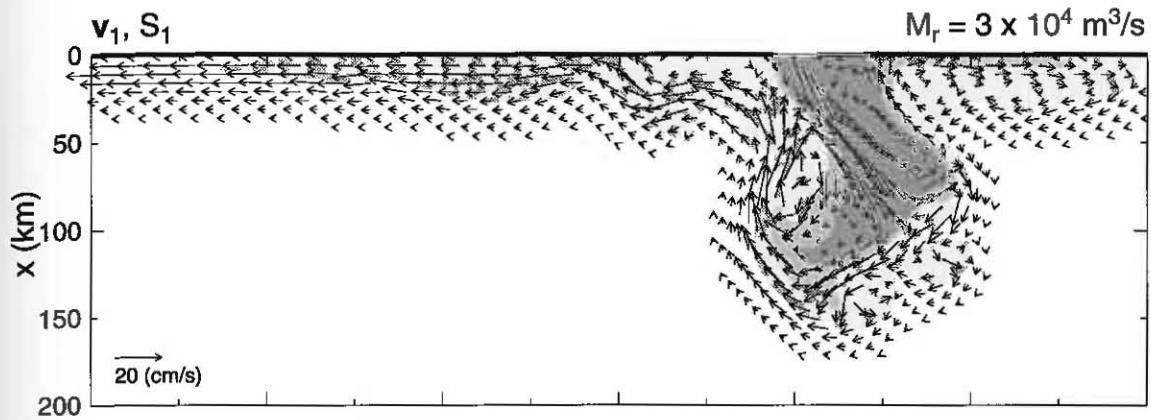
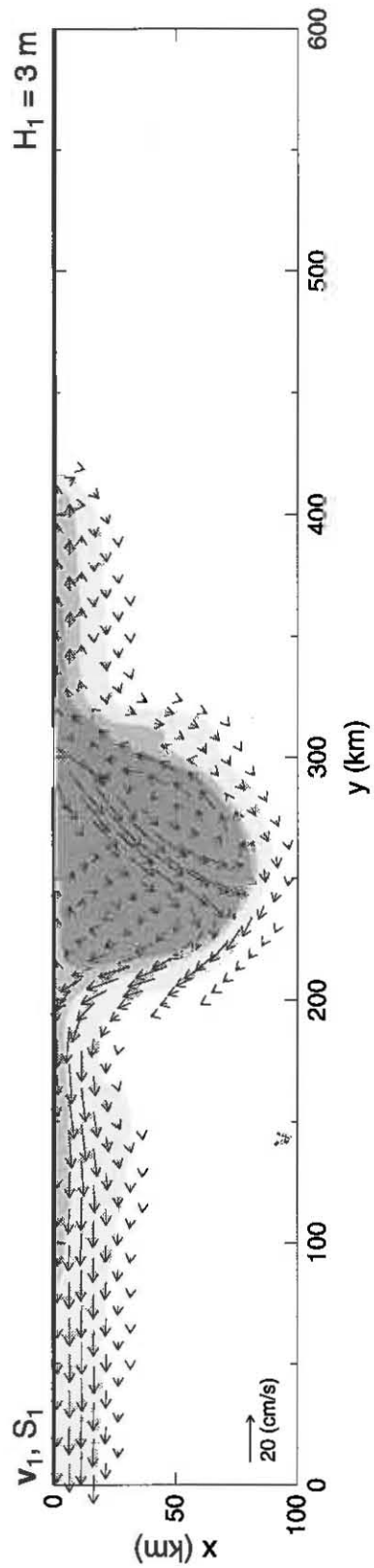
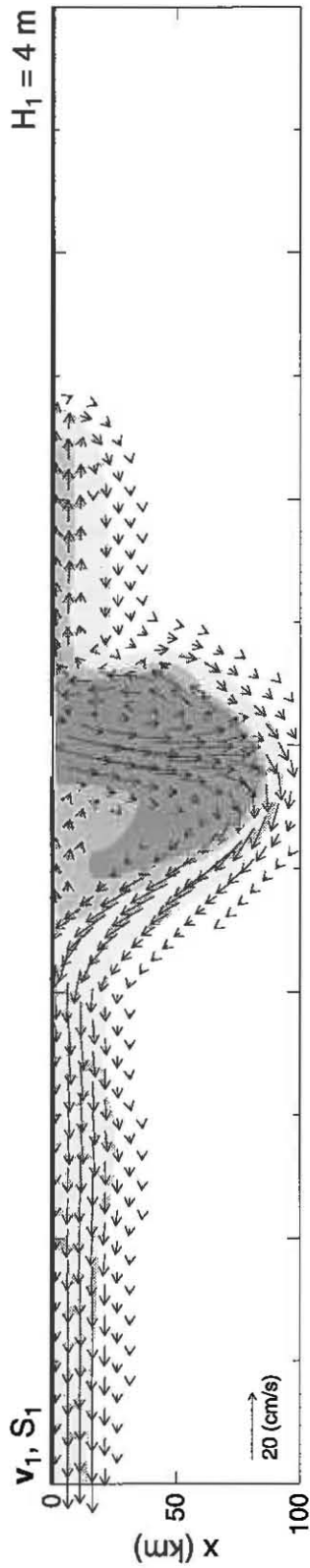
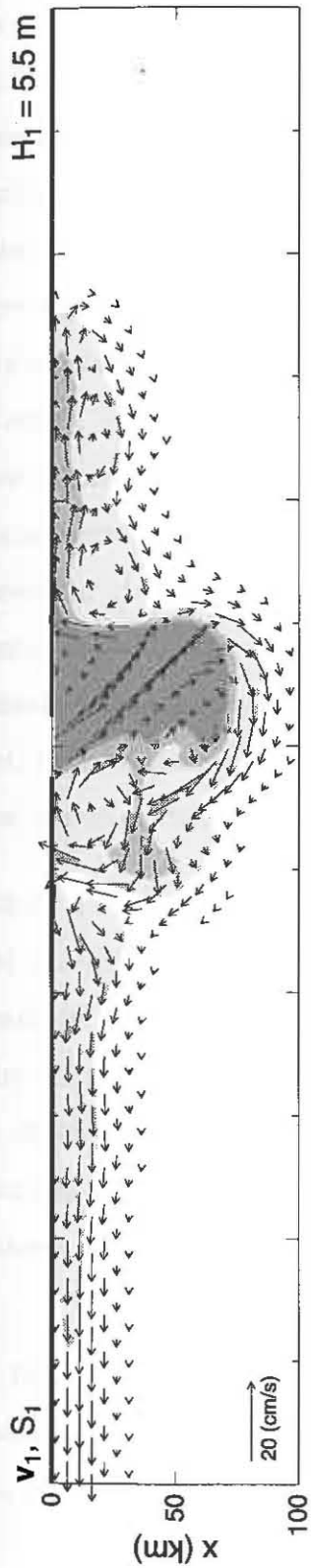


Figure 16: As in Figure 8, except showing v_1 and S_1 of the high- R_o solutions to the nonlinear model when $H_1 = 5.5$ m (upper panel), 4 m (middle panel) and 3 m (lower panel), which correspond to $R_o = 0.13$, 0.18 and 0.23, respectively. The offshore jet bends more to the south as H_1 decreases.



this point, Figure 17 shows a solution to the nonlinear model with the momentum-advection terms dropped (which essentially sets $R_o = 0$) for $M_r = 5 \times 10^4 \text{ m}^3/\text{s}$, corresponding to $\phi = 1.02$. In contrast to the solution in the middle panel of Figure 15, the river outflow does not flow directly offshore, but rather extends along both upstream and downstream coasts. It is concluded that momentum advection is essential for the formation of an offshore jet. This solution is similar to those in Figure 10, but unlike those solutions it continues to expand offshore indefinitely since $\phi > 1$.

Kubokawa's (1991) high-transport solutions with $\Delta q < 0$ (his Figure 5a) and Chapman and Lentz's (1994) solutions (their Figure 3) respond like the one in Figure 17, with the outflow advancing rapidly along both coasts and expanding slowly offshore. In the Chapman and Lentz (1994) solutions, however, the offshore expansion eventually ceases due to the presence of a bottom boundary layer. In addition, most of the outflow flows directly downstream, a difference that likely results from their value of ϕ (which is estimated to be considerably greater than 5) being much larger than ours ($\phi = 1$ for $M_r = 5 \times 10^4 \text{ m}^3/\text{s}$). Indeed, in a solution similar to Figure 15 but with $\Delta S = 2$ (so that $\phi = 5$), 88 % of the outflow bends southward to flow along the downstream coast.

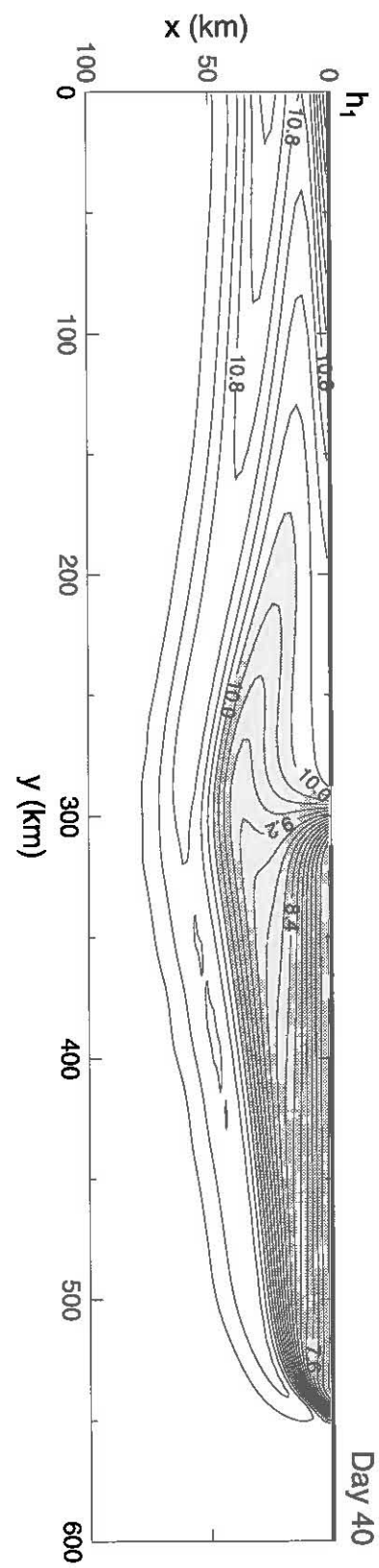
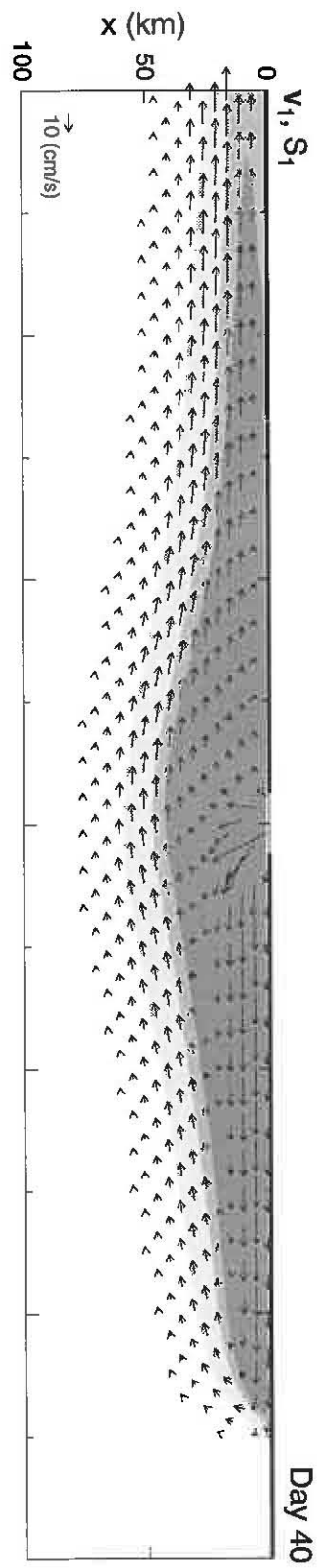
4.2.3 Jet angle: An interesting feature of above high- R_o solutions is that they all formed an offshore jet which enters the ocean at different angles α . In the following, an approximate expression for estimating α in terms of model parameters is developed.

The underlying hypothesis of the estimate is that α has the same direction as the maximum offshore velocity at the river mouth. For the $Y(y)$ profile given in (16), the location of maximum offshore velocity is close to the midpoint of the river mouth. The offshore component there is

$$u_m(0, \bar{y}) = \frac{\pi M_r}{2H_1 W}, \quad (59)$$

which follows from equation (15a) and the assumption that h_1 is uniformly H_1 . To obtain the alongshore component, it is assumed that near the river mouth the solution is like the low- R_o solution, and so can be split into a coastal mode and a gyre mode. The downstream

Figure 17: As in middle and lower panels of Figure 8, except showing the solution to the nonlinear model when the momentum advection terms are neglected and $M_r = 5 \times 10^4$ m³/s. The solution is similar in structure to the one in the lower panel of Figure 10, except that it continues to expand offshore indefinitely. In contrast to the corresponding nonlinear solution in the middle panel of Figure 15, there is no offshore jet.



component due to the coastal mode is,

$$v_c(0, \bar{y}) = \frac{1}{R_+} \int_{y_2}^{\bar{y}} \frac{M_r Y(y')}{H_1 W} dy', \quad (60)$$

where $y_2 = \bar{y} + W/2$. Equation (60) follows from equation (39) by assuming alongshore geostrophy subject to boundary condition (40). The upstream component due to the gyre mode can be directly obtained from (50) by setting $x = 0$, yielding

$$v_g = c_-(1 - \gamma)\chi. \quad (61)$$

Recall from the low- R_o solution that χ is a function of L and R_- , and hence depends on the upstream transport of fresher water. For the high- R_o solutions, however, *all* the river water does not flow upstream, as can be seen in Figure 15. At this point, then, χ is regarded as an unspecified constant to be determined.

Based on these three velocity components,

$$\alpha = -\tan^{-1} \frac{(v_g + v_c)}{u_m}. \quad (62)$$

Carrying out the integral in (60), and use (59) and (61), yields

$$\alpha = \tan^{-1} \left[\frac{W}{\pi R_+} \left(1 - \frac{4\gamma\chi}{(1 + \gamma)\phi} \right) \right]. \quad (63)$$

Note that variables in equation (63) other than χ are precisely determined in terms of model parameters.

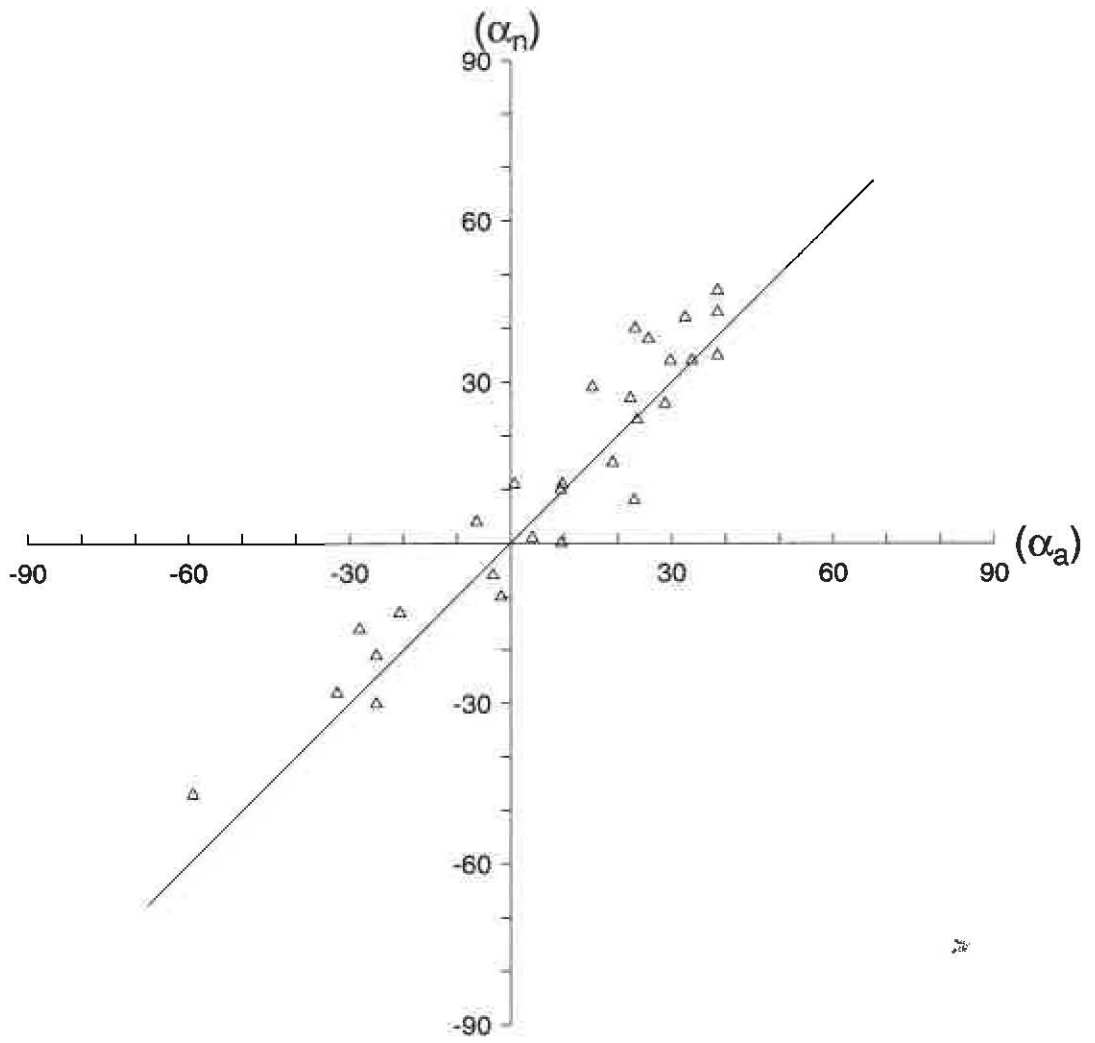
A property of the high- R_o solutions is that less river water goes upstream as R_o increases, indicating that χ should be a decreasing function of R_o . For simplicity, this decrease is represented by the linear function

$$\chi = \begin{cases} 1 - R_o/\delta & \text{if } R_o \leq \delta \\ 0 & \text{otherwise,} \end{cases} \quad (64)$$

for which χ varies from 0 to 1. Parameter δ is determined by making the best fit with numerical results, which gives $\delta = 1.5$.

Figure 18 compares values of α obtained from the numerical runs α_n with the corresponding value from equation (63) α_a . Data points (α_n, α_a) from 28 randomly chosen runs are

Figure 18: Comparison of the jet angle estimated from equation (63), α_a , with the angle measured from the corresponding numerical model, α_n . Each triangle symbol “ Δ ” represents a data point from one of the solution listed in Table 2. The points tend to cluster about the line $\alpha_a = \alpha_n$, indicating the agreement between α_a and α_n .



included in the figure. The parameters used to obtain these runs are listed in Table 2, and they cover a wide range of values for H_1 , S_r and M_r . The fact that the points tend to fall on the line $\alpha_n = \alpha_a$ indicates the good agreement between the numerical and analytic values. Linear regression shows that the correlation coefficient between α_n and α_a is 0.95 and the standard deviation is 8° .

In contrast to their low- R_o counterparts (see the end of Section 4.1.4), the high- R_o solutions are moderately sensitive to the current shear ζ at the river mouth. For example, when $Y(y)$ is replaced by Y_+ , solution (upper panel of Figure 19) differs from the one in the middle panel of Figure 15 in that the jet angle near the river mouth is shifted slightly to the left and less fresher water flows upstream. When $Y(y)$ is replaced by Y_- (lower panel of Figure 19), the plume does not expand as far offshore as for the one with $Y(y)$, and more fresher water flows upstream. This sensitivity to the structure of $Y(y)$ happens because ζ is larger in the high- R_o solution, and consequently, its effect on the outflow potential vorticity is no longer negligible.

4.3 Solutions with entrainment

An important process involved in upstream propagation is the thinning of h_1 within the plume. Since mixed-layer processes affect h_1 , they can therefore be expected to affect plume propagation. To investigate this possibility, Figure 20 shows two solutions when entrainment is included in the nonlinear model. Note that detrainment is not allowed in this case by setting H_d to be a very large value in equation (5). The upper and middle panels show the solution when $H_e = H_1 = 10$ m and $t_e = 1$ day, which assumes that the oceanic mixed layer can "recover" from the introduction of fresher water within a day or so. As for the $w_e = 0$ solution in Figure 8, the solution develops an upstream plume, but it propagates much more slowly northward. One reason for this slowing is that w_e thickens h_1 within the plume considerably (compare h_1 panels in Figures 8 and 20), thereby weakening the upstream coastal current. Another reason is that w_e increases the density of the plume by entraining salty and colder water into the upper layer (compare the shaded areas in the upper panels of Figures 8 and 20), which also weakens upstream geostrophic flow by increasing the

Figure 19: Similar to the middle panel of Figure 15, except that Y_+ (upper panel) and Y_- (lower panel), defined at the end of Section 3, are used as the outflow profiles.

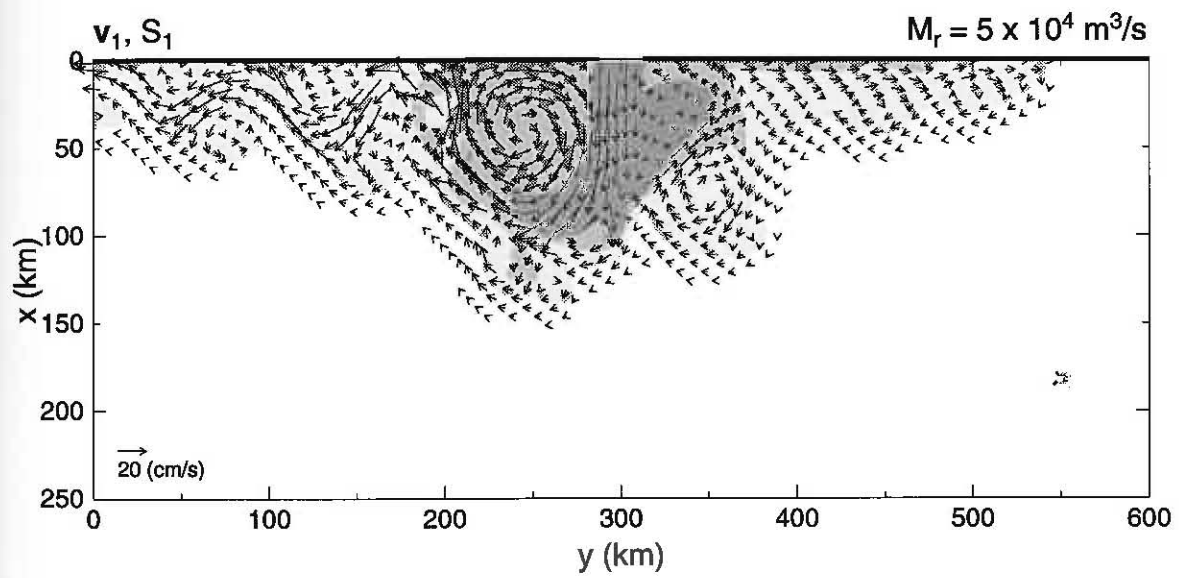
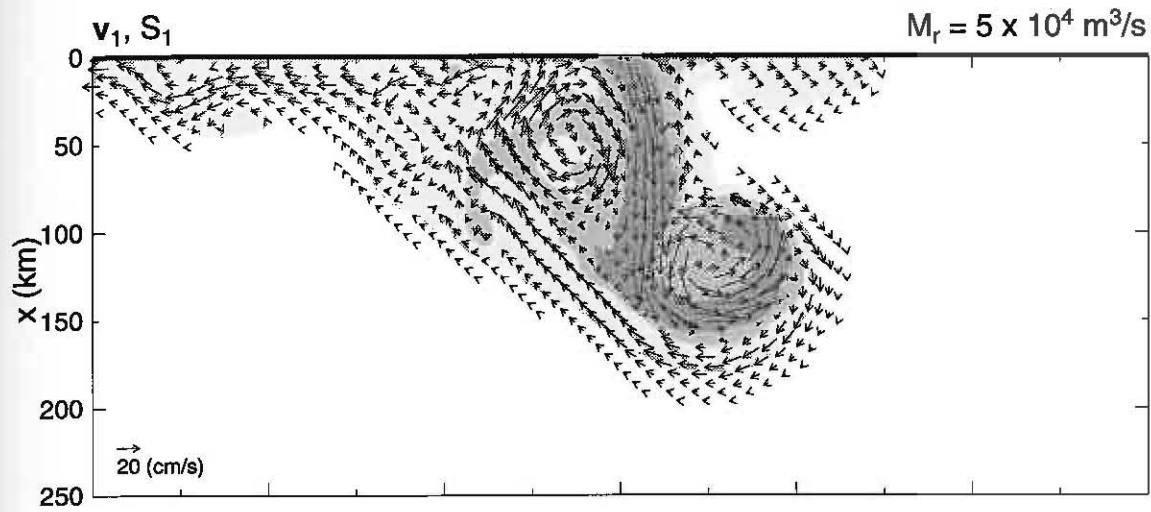
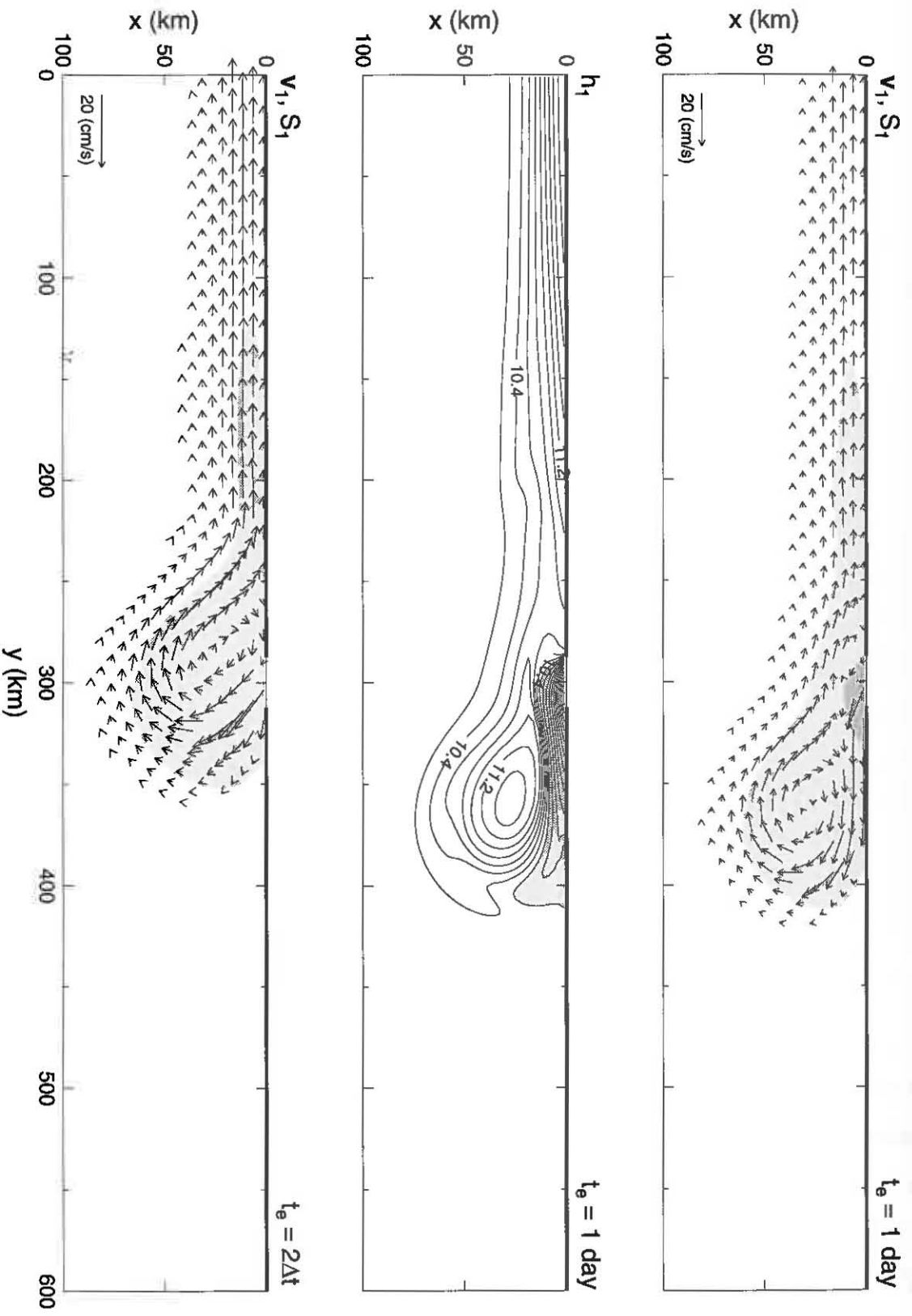


Table 2: A list of table for the parameter values used in Figure 18. A total of 28 runs were chosen in which M_r , H_1 and S_r are specified for each run. Then the non-dimensional variables R_o and ϕ are determined in terms of these model parameters.

No.	M_r (a)	H_1 (m)	ΔS	R_o	ϕ	α_n (deg)	α_a (deg)
1	5	10	10	0.33	1.0	10	9
2	4	10	10	0.28	0.8	4	-6
3	3	10	10	0.21	0.6	-28	-32
4	2	10	10	0.14	0.4	-47	-59
5	2	10	5	0.15	0.8	-16	-28
6	3	10	5	0.21	1.2	11	1
7	4	10	5	0.26	1.6	29	15
8	5	10	5	0.31	2.0	40	23
9	5	10	15	0.35	0.7	-10	-2
10	4	10	15	0.28	0.5	-30	-25
11	8	10	10	0.53	1.6	42	32
12	2.5	5	10	0.33	2.0	38	26
13	10	20	10	0.33	0.5	-21	-25
14	7	10	10	0.50	1.4	34	30
15	6	10	10	0.42	1.2	27	22
16	4	5	20	0.85	1.6	47	39
17	3	5	15	0.55	1.6	34	34
18	2	5	10	0.36	1.6	23	24
19	1	5	5	0.18	1.6	11	10
20	2.5	5	20	0.44	1.0	8	23
21	1.8	5	15	0.32	1.0	0	9
22	1.2	5	10	0.23	1.0	-6	-3
23	0.6	5	5	0.12	1.0	-13	-21
24	0.9	5	5	0.16	1.4	1	4
25	1.8	5	10	0.32	1.4	15	19
26	2.6	5	15	0.47	1.4	26	29
27	3.5	5	20	0.67	1.4	35	39
28	4.4	5	25	1.0	1.4	43	39

Figure 20: As in Figure 8, except for solutions to the nonlinear, variable-density, $1\frac{1}{2}$ -layer model that include entrainment when $t_e = 1$ day (upper and middle panels) and when $t_e = 2\Delta t$ (lower panel). The value of H_e is the same as H_1 in this case. Detrainment is not allowed by specifying H_d to be a very large value in equation (5). The shading in the middle panel indicates where $h_1 \lesssim H_1$, and hence where $w_e \neq 0$. In the $t_e = 1$ day solution, the plume advances northward more slowly and salinity is higher than in the corresponding $w_e = 0$ solution (Figure 8). In the $t_e = 2\Delta t$ solution, there is almost no northward plume propagation.



upper-layer density. When $t_e = 2\Delta t$ (lower panel), h_1 can never become much less than H_1 , and the upstream propagation is almost eliminated.

Solutions (not shown) with larger M_r (say $M_r = 3 \times 10^4 \text{ m}^3/\text{s}$ and $5 \times 10^4 \text{ m}^3/\text{s}$), and therefore larger R_o , possess similar features with those in Figure 20. The jets that exist in the corresponding $w_e = 0$ solutions are absent here, suggesting that the entrainment process makes it difficult or impossible to distinguish low- and high- R_o solutions.

CHAPTER 5

SOLUTIONS TO THE $2\frac{1}{2}$ -LAYER MODEL

The intention in this chapter is to simulate river-outflow-driven circulations as realistically as possible. For this purpose, the $2\frac{1}{2}$ -layer model is utilized, since circulations and water properties in many estuaries, as well as the adjacent coastal ocean, often exhibit a two-layer structure, with fresher water flowing into the ocean in the upper layer and saline water being drawn into the estuary in the lower layer. The strength of lower-layer inflow is determined by mixing processes within the estuary. Suppose that fresh water ($S = 0$) enters the estuary at its upstream end, and continues to flow downstream towards the estuary mouth in the upper layer. During its path, saline water can be entrained into the upper layer due to vertical mixing, so that the downstream transport and salinity of the upper layer increases towards the river mouth. To compensate for the loss of saline water in the lower layer, an inflow of transport M_2 at the estuary mouth must occur. Observational evidence demonstrating the flow of shelf water into estuaries can be found in several studies, (*e.g.*, Pape and Garvine, 1982, Norcross and Stanley, 1967, and Bumpus, 1973). Suppose further that the system has reached a steady state in which both mass and salt are conserved within the estuary. Then, since the water drawn into the estuary is entrained into the upper layer and eventually flows back into the ocean in the upper layer, there is no net salt transport across the river mouth, that is,

$$S_2^* M_2 + S_r M_r = 0. \quad (65)$$

A verification of equation (65) is reported in Garvine (1991) for the case of Delaware Bay mouth, where he estimates a seaward salt flux is roughly balanced by a landward salt flux. It follows from equation (65) that the transport of the inflow is

$$M_2 = -\frac{S_r}{S_2^*} M_r. \quad (66)$$

Equation (66) is used as the boundary condition for the lower layer throughout this chapter.

First, in Section 5.1, the effect of lower-layer inflow is considered. Then, in Section 5.2, solutions are discussed when an alongshore background current is present. Finally, in Section 5.3 solutions are presented when an alongshore wind forces the system.

5.1 Effect of lower-layer inflow

Figure 21 shows the solution to the $2\frac{1}{2}$ -layer model 40 days after the onset of outflow and inflow at the river mouth in the upper and lower layers, respectively. The parameter values used are those listed in Table 1, which imply that M_2 is 57% of the outflow. In the upper layer (upper panel), the solutions are quite similar to the corresponding $1\frac{1}{2}$ -layer solution in Figure 8: All the river water first bends to flow along the upstream coast, with some of it reversing direction at the plume nose to form a return flow along the offshore density front that eventually flows along the downstream coast. In addition, the nose slowly advances northward at a speed of about 6.4 cm/s, leaving behind a region where the upper layer becomes shallower than H_1 (not shown). In the lower layer (middle panel), the flow is generally directed opposite to the upper-layer flow, and the water that is drawn into the estuary is all from the downstream region. Contours of $h_1 + h_2$ (bottom panel) are geostrophic streamlines for \mathbf{v}_2 , and hence this field illustrates this lower-layer flow pattern even more clearly than the arrow plot does.

The linear version of this solution is shown in Figure 22a. The primary features in the linear solution are the same as in the nonlinear one, except for the absence of unstable waves. In addition, the offshore scale of the downstream current is narrower in comparison to its nonlinear counterpart, apparently due to the absence of horizontal mixing. Fields in the upper layer (upper panel) are very similar to their $1\frac{1}{2}$ -layer counterparts (upper panel of

Figure 21: A solution to the nonlinear, $2\frac{1}{2}$ -layer model when lower-layer flow into the river mouth is included, showing velocities \mathbf{v}_1 and salinities S_1 (upper panel), \mathbf{v}_2 (middle panel) and $h_1 + h_2$ (lower panel) at day 40. Contour interval for $h_1 + h_2$ is 0.1 m. Regions where $S_1 < 22.5$, $22.5 < S_1 < 25$ and $25 < S_1 < 29$ are indicated by dark, medium and light shading, respectively. A prominent feature of this solution is that the flow in the lower layer is generally in the opposite direction to the upper layer flow.

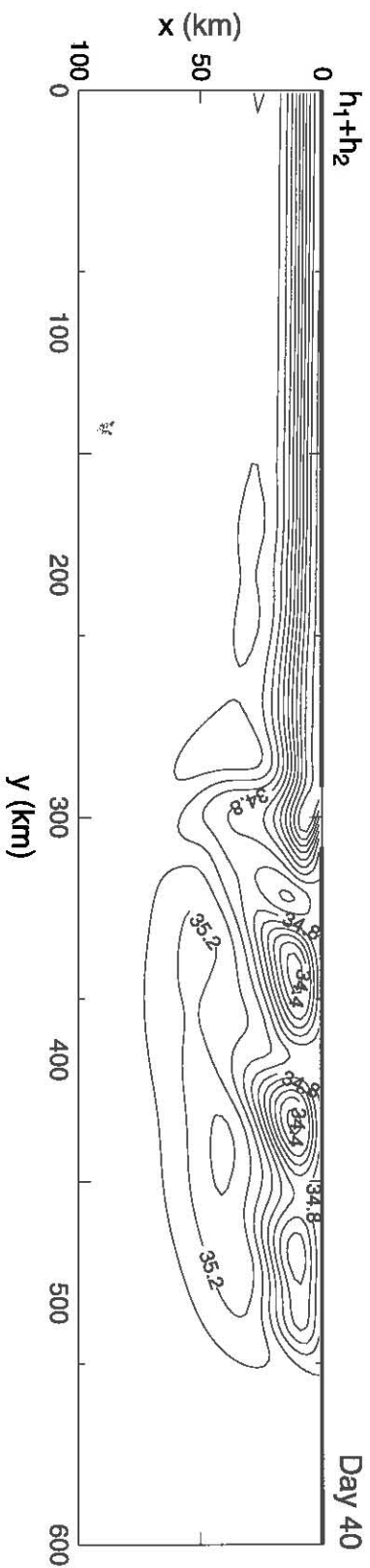
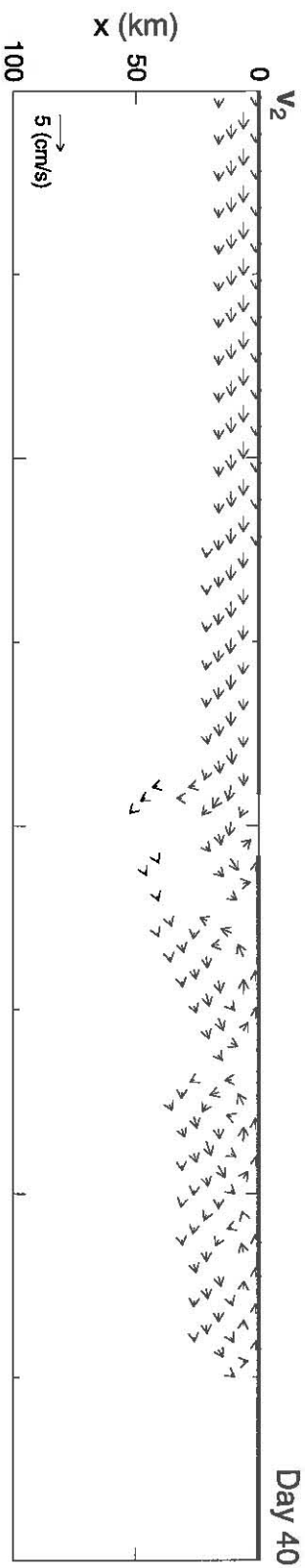
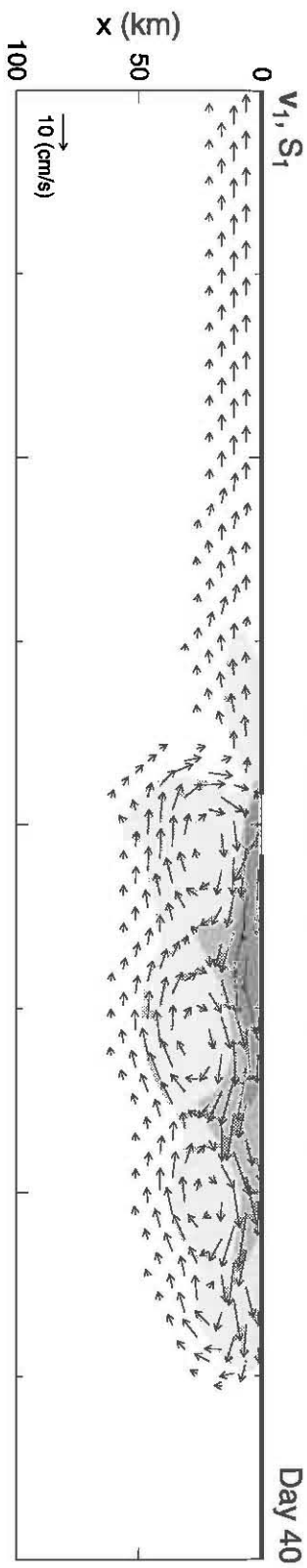


Figure 22a: As in Figure 21, except for the solution to the linear, $2\frac{1}{2}$ -layer model. Like its $1\frac{1}{2}$ -layer counterpart shown in the upper and middle panels of Figure 10, the instability is absent, and the plume is y -independent behind the nose in the upstream region.

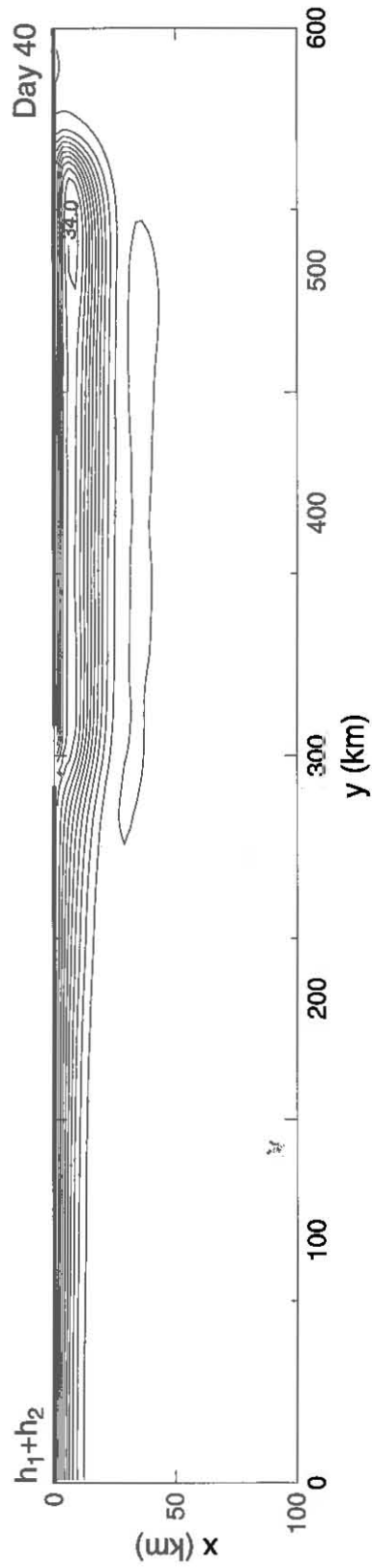
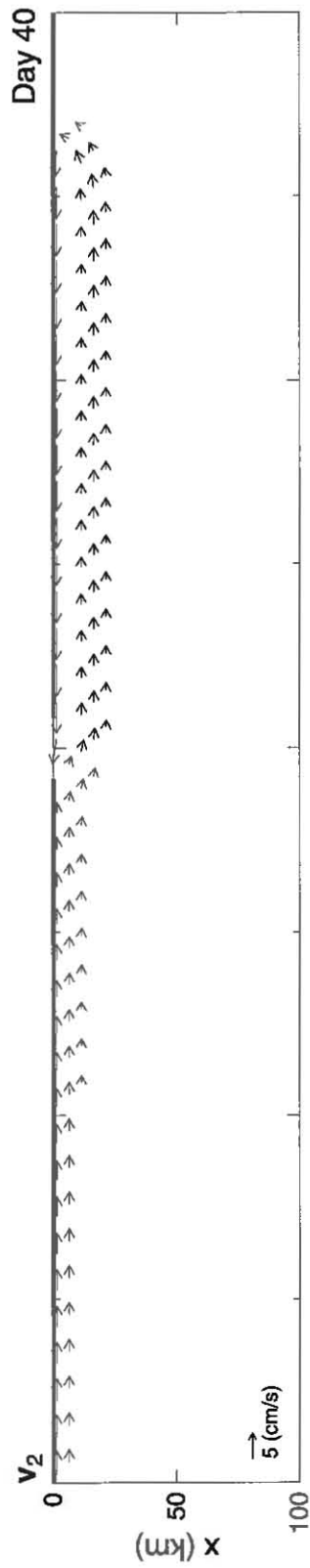
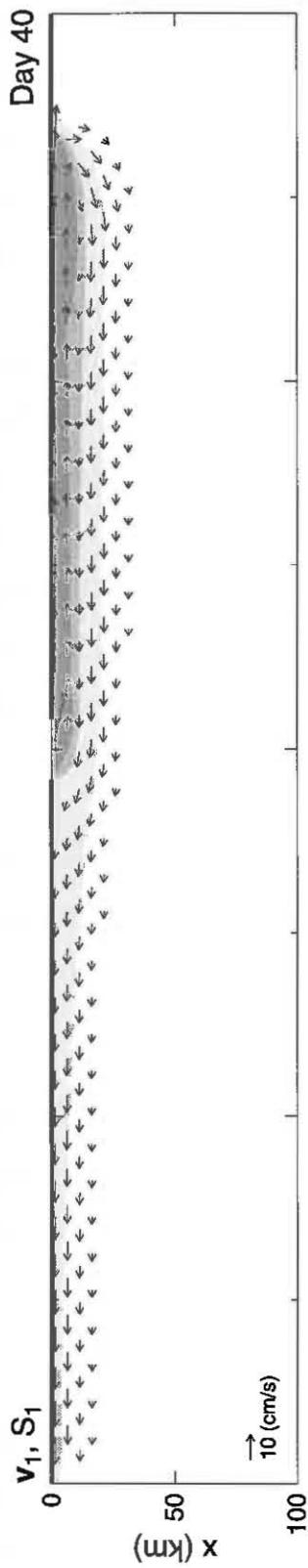


Figure 10), suggesting that upper layer solution is not sensitive to either the existence of an active lower layer or the inflow at the river mouth.

The dynamics of the northward downstream coastal current in the lower layer are similar to those of the upper-layer “fast” response, and involve the radiation of Kelvin waves along the downstream coast (Sections 4.1.1 and 4.1.2). In this case, however, the spin-up involves the radiation of *both* baroclinic modes of the $2\frac{1}{2}$ -layer system. (See Appendix B for a review of the vertical modes in a $2\frac{1}{2}$ -layer model.) To demonstrate this point, consider the response of a linear, $2\frac{1}{2}$ -layer system to an upper-layer mass outflow M_r into the ocean and a lower-layer inflow $M_2 = -0.57M_r$ directly underneath. As a result, coastal currents in both layers will be established via the radiation of Kelvin waves, which generate the values of coastal pressures along the downstream coast, $p_1(0)$ and $p_2(0)$. By geostrophy, these two pressures are $p_1(0) \simeq fM_r/H_1$ and $p_2(0) \simeq -0.57fM_r/H_2$.

Since the system is linear, the total response can be represented by the sum of responses for its two baroclinic modes

$$\begin{pmatrix} p_1 \\ p_2 \end{pmatrix} = p^1\psi_1 + p^2\psi_2, \quad (67)$$

where ψ_1 and ψ_2 are the structure functions for each mode, given in equation (B5) of Appendix B, and p^1 and p^2 are their corresponding amplitudes. The solution along the downstream coast is found by solving the equation

$$p_{xx}^n - \frac{f^2}{c_n^2}p^n = -\frac{f^2}{c_n^2}p^n(t=0), \quad n = 1, 2 \quad (68)$$

subject to boundary conditions $p^n = p^n(0)$ at $x = 0$ and $p^n = 0$ as $x \rightarrow \infty$ when $p_x^n(t=0) = 0$. Equation (68) results from conservation of potential vorticity of the system (B7).

The solution is the free wave that decays away from the coast,

$$p^n = p^n(0)e^{-(f/c_n)x}, \quad (69)$$

where $p^n(0)$ can be obtained from $p_i(0)$ via equation (67). The velocity fields for each mode are obtained from (69) by geostrophy, and the velocities in each layer are calculated from equation (67) with p replaced by v .

The two panels of Figure 22b show the upper-layer (upper panel) and lower-layer (lower panel) currents in the downstream region ($y = 50$ km) as obtained from the numerical model

(thick curves) and from the sum of responses for each mode (short-dashed curves). The two curves for each layer compare reasonably well with each other, suggesting that the numerical solution can be accurately represented as a superposition of mode responses. Differences between the two types of solutions happen because the former includes a component driven by the plume which is missed in the latter. The contributions of each mode (long-dashed curve for mode 1 and thin-solid curve for mode 2) are also plotted in each panel, showing that the response of mode 2 dominates the total response. In particular, mode-2 northward flow overwhelms mode-1 southward flow in the lower layer, so that the total current is directed northward.

Lower-layer northward flow along the downstream coast is also present in other models. For example, in Chao and Boicourt's (1986) solution, there is northward flow near the bottom along the downstream coast that is stronger near the river mouth and weaker downstream (their Figure 10). They interpreted this flow to be the result of the radiation of a first-mode baroclinic Kelvin wave (which is equivalent to our second-mode Kelvin wave when the bottom of layer 2 is the sea floor).

Similarly, the circulation in the upstream region can be interpreted as the sum of responses for each vertical mode. In this case, the circulation is considered to be driven by an initial upper-layer patch of high pressure associated with the plume, that is, $p_1 = p_r$ and $p_2 = 0$ at $t = 0$. According to (67), initial pressures corresponding to each mode are then $p^1(t = 0) = 0.67p_r$ and $p^2(t = 0) = 0.33p_r$. The steady-state pressure field for each mode can then be found from equation (68) subject to boundary conditions $p^n = 0$ at $x = 0$ and as $x \rightarrow \infty$. Equation (68) is solved numerically within a finite domain extending from $x = 0$ to $x = 150$ km, the eastern boundary being far enough offshore to represent infinity provided the forcing is coastally confined.

The resulting solution is shown in Figure 22c when p_r is obtained from a river-outflow-driven solution to the linearized version of equation (10a). Specifically, p_r is determined from the day-40 salinity field along 400 km in that solution. In this case, the numerical and modal solutions are extremely close, suggesting that the numerical response in the upstream region can be viewed as being driven primarily by the *upper-layer* pressure field due to the input of fresher water. Again, the mode-2 response dominates mode-1 response in the lower-layer

Figure 22b: Across-shore structure of alongshore velocities in the downstream region, showing upper- and lower-layer flows in the top and bottom panels, respectively. Each panel plots four curves: the day-40 solution to the linear, $2\frac{1}{2}$ -layer model with lower-layer inflow along a section at $y = 50$ km (thick-solid curve), the superposition of the responses of both baroclinic modes (short-dashed curve), the contributions to v_1 from mode 1 (long-dashed curve) and mode 2 (thin-solid curve). In the bottom panel, the mode-2 response dominates the total response, accounting for the existence of a northward coastal current in the lower layer.

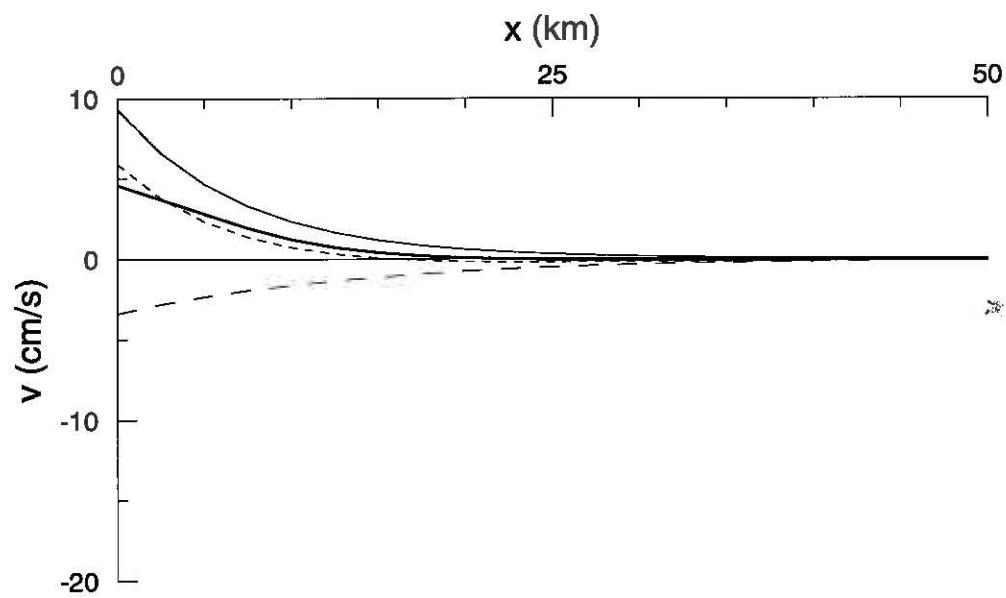
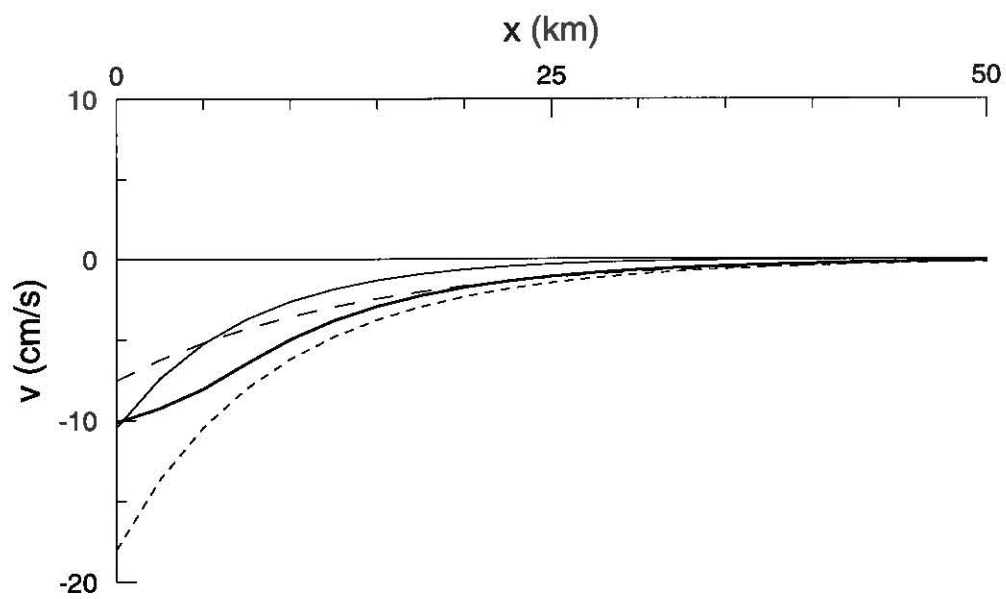
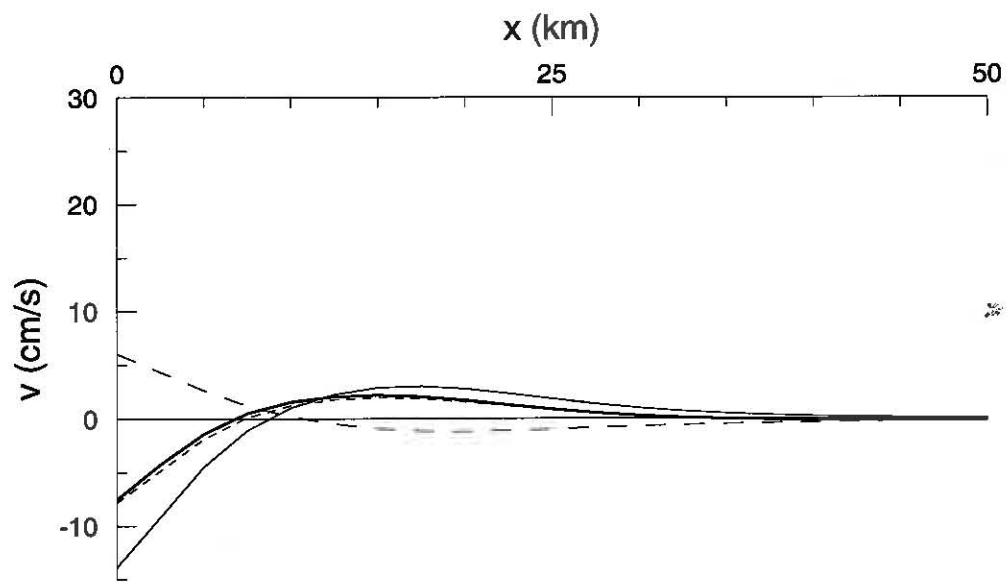
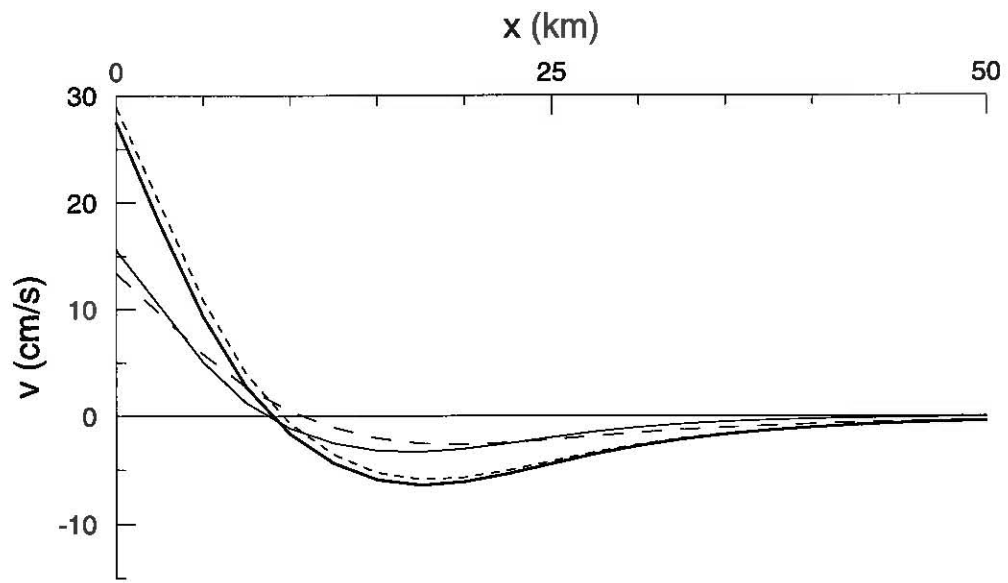


Figure 22c: Similar to Figure 22b, except for the upstream region. The numerical solution is taken along a section at $y = 400$ km after 40 days. As for its downstream counterpart, the mode-2 response dominates the total response for the lower-layer flow, accounting for southward flow near the coast and northward flow offshore.



flow, so that the total lower-layer flow is essentially opposite to that in the upper layer.

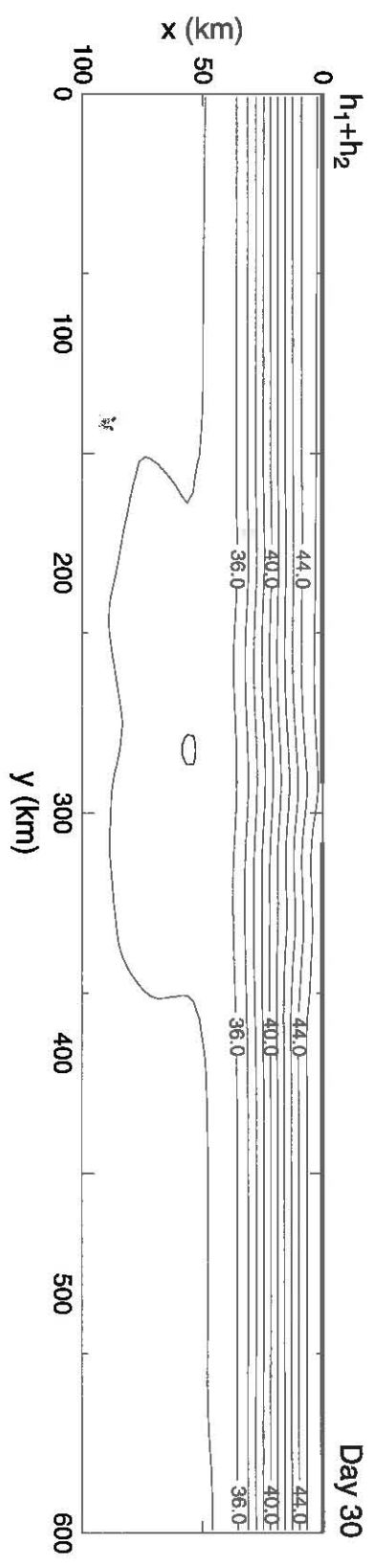
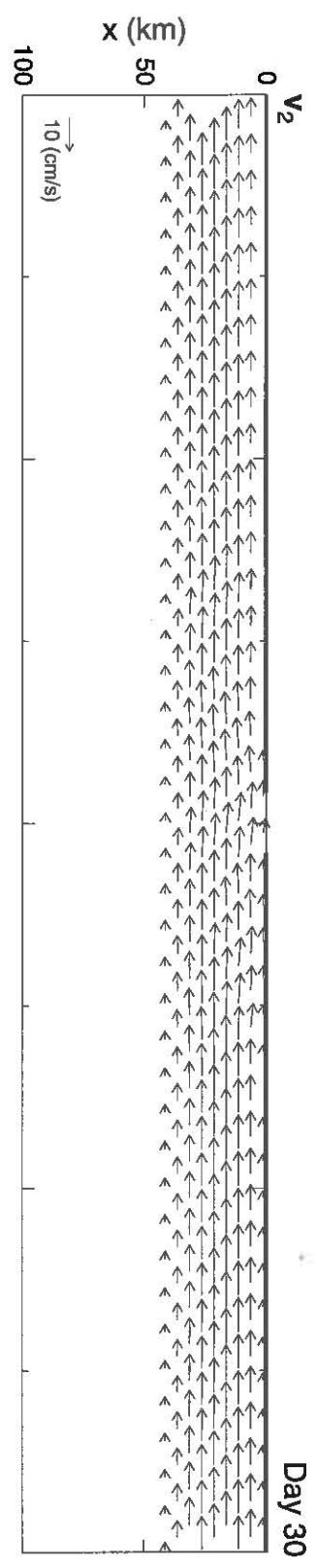
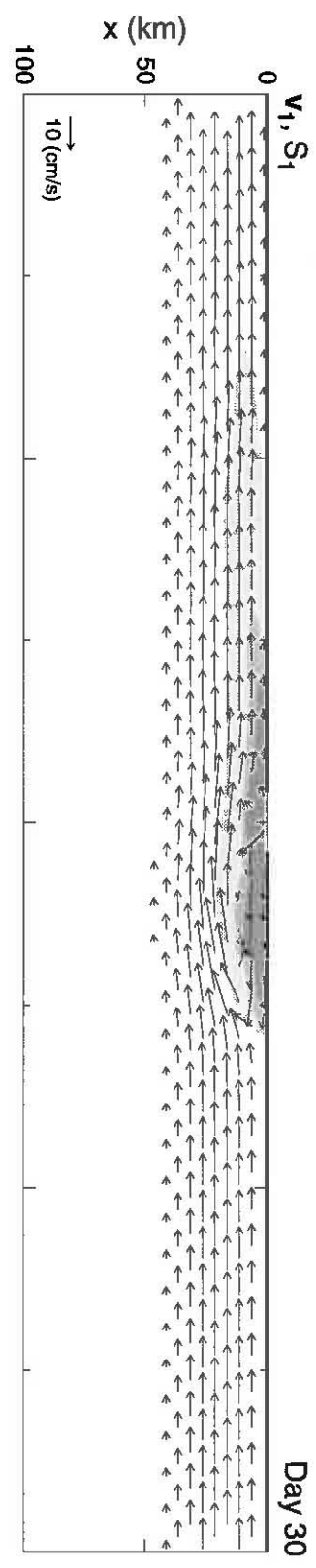
It is noteworthy that the lower layer develops any flow at all, considering that the initial lower-layer pressure $p_2(t = 0)$ is everywhere zero. This property is a consequence of the two modes having different Rossby radii: If $c_1/f = c_2/f$ in equation (68), it follows that $p^2/p^1 = p^2(t = 0)/p^1(t = 0)$, and hence $p_2 = p_2(t = 0) = 0$. When $c_1/f \neq c_2/f$, their responses have different horizontal structures, and therefore can never cancel each other in the lower layer.

5.2 Effect of a background current

In this section, the influence of a background current V_b on the evolution of river plume is investigated. In all the runs, V_b is directed downstream and has no variation in the alongshore direction. Initially, it is uniform within 30 km from the coast and linearly decreases to zero from 30 km to 40 km offshore, as shown by the dashed line in the upper panel of Figure 24 for the case of $V_b = -10$ cm/s. This current is imposed in both layers with the same magnitude. The initial layer thicknesses are prescribed so that the pressures in both layers geostrophically balance V_b . However, because of the no-slip boundary condition and horizontal mixing, this initial state necessarily undergoes adjustment to accommodate these constraints. The solid curves in the same panel show the across-shore profiles of this current at day 10, 20, 30 and 40 during the adjustment under the influence of mixing without forcing by river outflow. Other parameters are those listed in Table 1. As can be seen, the initial adjustment is rapid, and then slows down significantly. For this reason, in all the runs the river outflow is switched on at day 10.

Figure 23 shows the day 30 solution (20 days after the onset of the upper-layer outflow and lower-layer inflow) when V_b is -10 cm/s and other parameters are the same as those for the solution in Figure 21. The plume is trapped in the background current and moves swiftly along the downstream coast. It also advances slowly along the upstream coast (upper panel), but there are no unstable waves. In the lower layer, the flow is uniformly downstream (middle panel) and all the water drawn into the estuary is from the upstream coast, as can also be seen from the curvature of $h_1 + h_2$ contours near the river mouth (lower panel) since

Figure 23: Similar to Figure 21, except for the solution at day 30 (20 days after the onset of river outflow) when a downstream background current $V_b = -10$ cm/s is included. Contour intervals for $h_1 + h_2$ is 1 m. River water flows predominantly downstream, but there is still upstream motion.



contours of $h_1 + h_2$ are streamlines of lower-layer flow.

Solutions for other values of V_b show similar features as in Figure 23, except that plumes move downstream more rapidly and advance upstream more slowly as $|V_b|$ increases. This influence is revealed in Figure 25, which is a latitude-time plot of coastal salinity $S_1(0, y)$ when $V_b = -10$ cm/s (upper panel), -15 cm/s (middle panel) and -20 cm/s (lower panel). When the magnitude of V_b is increased to 20 cm/s, the upstream plume is virtually stopped, as indicated by the nearly vertical slope of $S_1(0, y)$ in the upstream region.

The above results suggest that the speed of upstream motion of the plume is determined by a competition between the strength of upstream motion in the absence of V_b and the ability for the background current to shift it downstream. To demonstrate this point, the difference between these two components, that is, $\bar{v}_1(x) - |V_b|$ where $\bar{v}_1(x)$ is a measure of the strength of upstream motion without any influence of V_b , is plotted in the lower panel of Figure 24. To estimate $\bar{v}_1(x)$, the alongshore velocity behind the upstream plume nose for a well-developed plume is taken to be its average value over a wavelength of unstable wave ($375 \text{ km} < y < 425 \text{ km}$) for the solution in the upper panel of Figure 21. The background current V_b is taken after 30 days adjustment under the influence of mixing. The offshore profiles of $\bar{v}_1(x) - |V_b|$ are shown for $V_b = -10$ cm/s (solid curve), -15 cm/s (thick dashed curve) and -20 cm/s (thin dashed curve), respectively. The positive side on these curves in the nearshore region measures the ability of the northward current generated by the plume to overcome the southward background current, thereby causing upstream motion. Moreover, the magnitude of $\bar{v}_1(x) - |V_b|$ on the positive side is consistent with the speed of upstream motion in solutions with the influence of V_b ; for example, the upstream speed is ≈ 5 cm/s in the solution with $V_b = -10$ cm/s, as measured by the slope of $S_1(0, y)$ on the coast in the upper panel of Figure 25; the magnitude of $\bar{v}_1(x) - |V_b|$ on the positive side is also about 5 cm/s (solid curve in the lower panel of Figure 24).

Unlike solutions with $V_b = 0$, such as those in Figure 15, a large offshore plume together with the offshore jet does not develop for higher transport and hence higher R_o . For example, a solution with $M_r = 3 \times 10^4 \text{ m}^3/\text{s}$ and $V_b = -10$ cm/s has a similar solution to the one in the upper panel of Figure 23, except that the plume moves more rapidly to the south.

Figure 24: The upper panel shows the adjustment of a background current V_b under the influence of no-slip boundary condition and horizontal mixing. Parameters used are those from Table 1, except that no river outflow is imposed. Initially, V_b is imposed in both layers, and it is uniformly -10 cm/s within the region $0 < x < 30$ km and linearly tapers off from 30 km to 40 km (dashed lines). The initial h_1 and h_2 are specified such that pressures in both layers geostrophically balance V_b . The subsequent profiles at day 10, 20, 30 and 40 are represented by solid curves in the order such that $|V_b|$ decreases with time in the near-shore region ($0 < x < 10$ km), respectively. The lower panel shows the offshore structure of $\bar{v}_1(x) - |V_b|$, where $\bar{v}_1(x)$ is the average within a wavelength (375 km $< y < 425$ km) of alongshore flow shown in the upper panel of Figure 23, and $|V_b|$ is 10 cm/s (solid curve), 15 cm/s (thick dashed curve) and 20 cm/s (thin dashed curve), respectively. All the V_b are the results after 30 days adjustment under the influences of no-slip boundary condition and mixing.

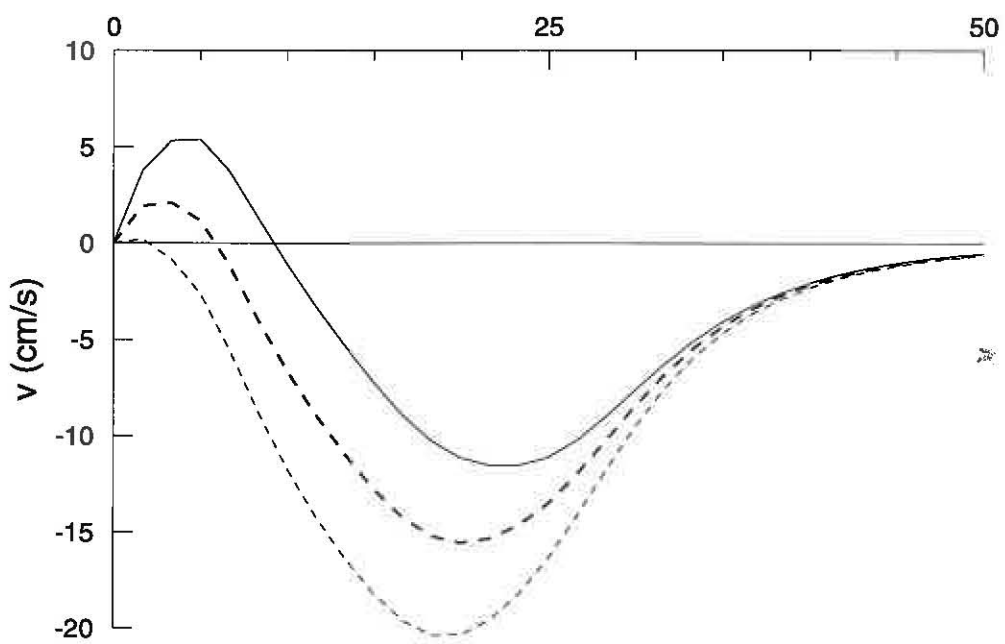
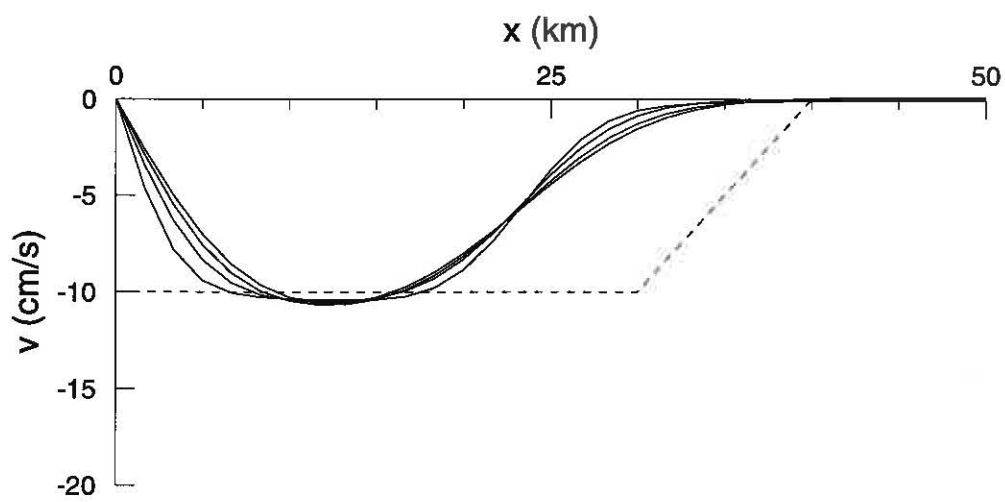
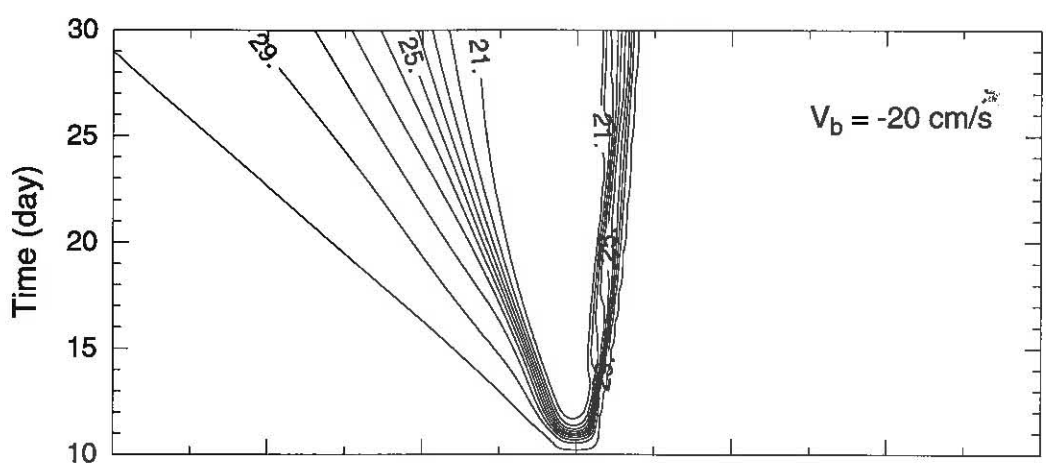
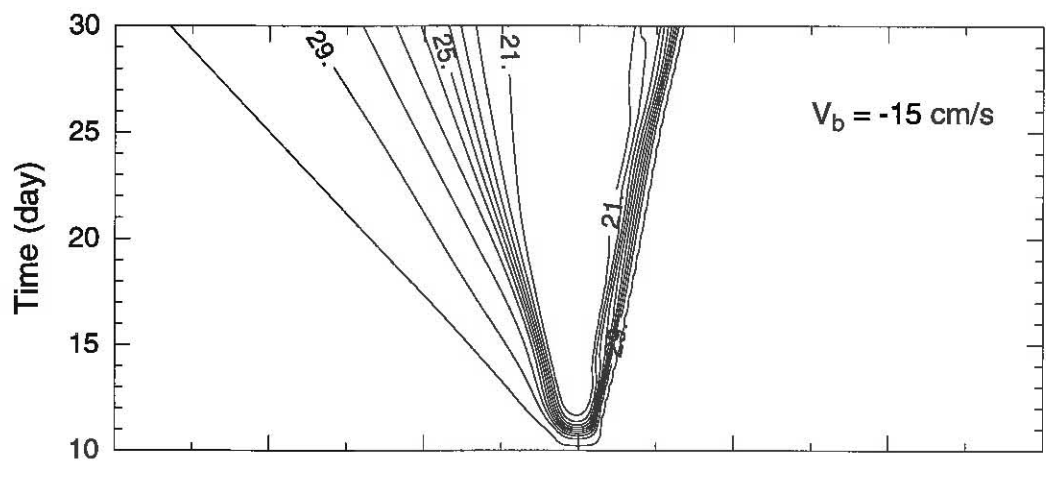
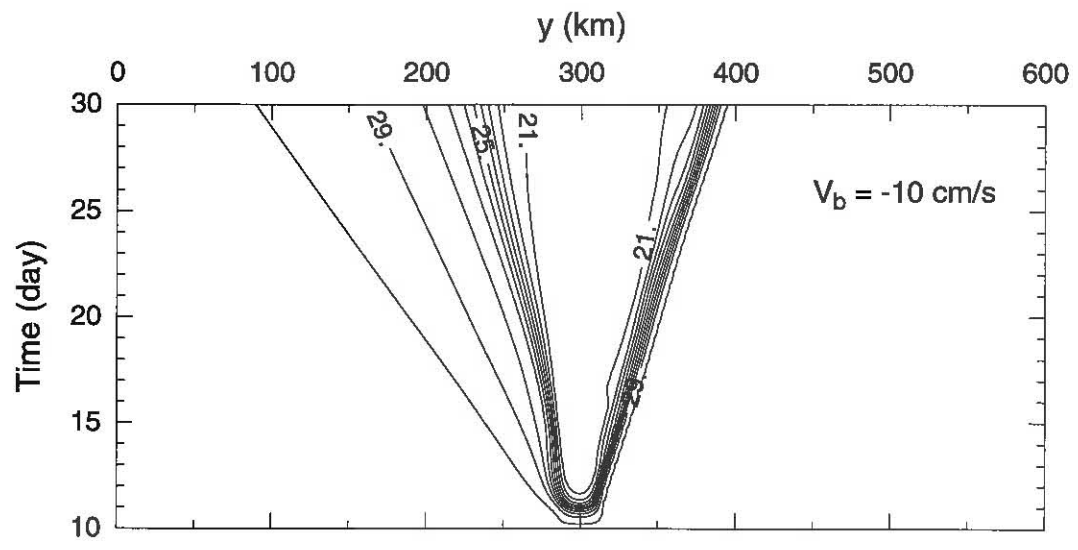


Figure 25: Latitude-time plots of salinity on the coast $S_1(0, y)$ in a sequence of solutions under the influence of V_b . The background currents V_b are -10 cm/s (upper panel), -15 cm/s (middle panel) and -20 cm/s (lower panel), respectively. Note that as $|V_b|$ increases, the upstream motion slows down and even stops when $V_b = -20$ cm/s.



5.3 Effect of wind forcing

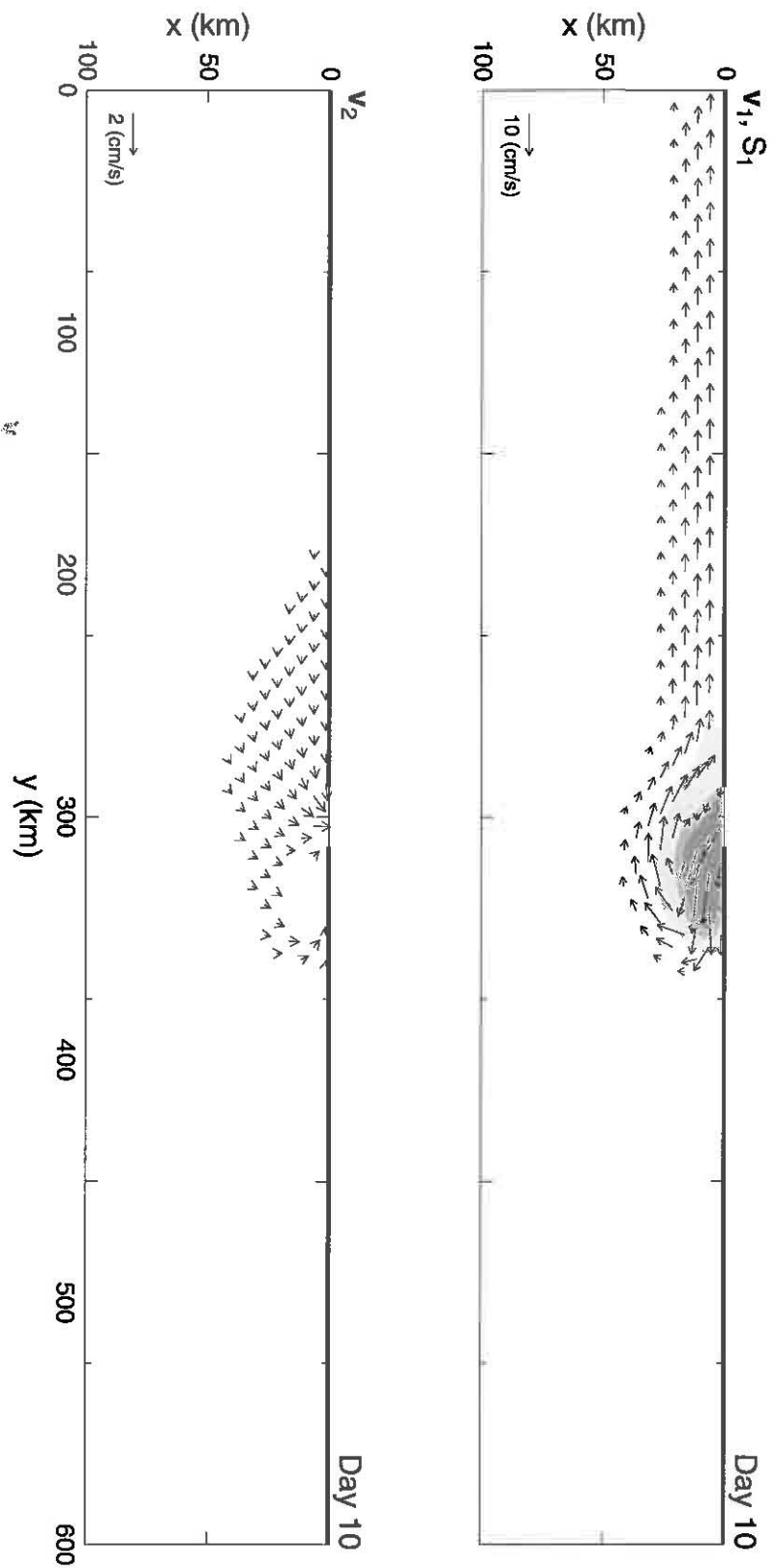
In this section, the influences of both upwelling-favorable and a downwelling-favorable alongshore winds τ^y are investigated. In each case, the river plume is allowed to develop for 10 days, then a uniform wind with magnitude of 0.5 dyn/cm^2 is gradually switched on within 1 day using the ramp defined in equation (17). The use of the ramp significantly subdues inertial oscillations. The wind remains steady for another 9 days, and the responses at day 15 (5 days after the switch-on of wind) and 20 are described and compared with the day-10 solution. In all cases, a lower-layer inflow at the river mouth with a transport specified by equation (66) is imposed. Entrainment or detrainment parameterized by equation (5) is also included.

The drag term $-bh_2\mathbf{v}_2$ is also included in equation (9a). Without this term, the Ekman drift driven by an upwelling-favorable wind (for example) rapidly advects upper-layer water away from the coast, h_2 then decreases at the coast due to entrainment into the upper layer, and the solution eventually blows up when $h_2 \rightarrow 0$. Analogous problems occur when the model is forced by downwelling-favorable wind. As will be seen, the inclusion of drag generates an across-shore flow in the lower layer that largely compensates for the Ekman drift, and as a result it delays the occurrence of h_2 being zero near the coast; this delay allows us to examine wind-driven effects for a longer period of time.

The value of b used for the solutions shown here is $b = 0.5 \times 10^{-4} \text{ s}^{-1}$. Note that this value is of the same order as the Coriolis parameter f , so that the ageostrophic component of lower-layer flow can be as large as the geostrophic one. The physical meaning of b is not clear in a reduced-gravity model. It can be regarded as analogous to bottom stress in a 2-layer system with a drag coefficient of $bh_2 = 0.125 \text{ cm/s}$ when $h_2 = H_2^* = 25 \text{ m}$. This value for bh_2 is consistent with drag coefficients commonly used in modeling studies; for example, in a study of the withdrawal of shelf water into an estuary, Masse (1990) chose a linear drag coefficient of 0.1 cm/s .

Figure 26 shows the solution at day 10, just before the onset of alongshore winds. In this solution, parameters used are those from Table 1, except that a larger horizontal mixing coefficient $\nu = 5 \times 10^5 \text{ cm}^2/\text{s}$ is adopted. The upper-layer circulation (upper panel) is similar

Figure 26: Solutions of the nonlinear, $2\frac{1}{2}$ -layer model with both w_e and a drag term $-bh_2v_2$ included. Parameters used are those in Table 1, except that $\nu = 5 \times 10^5$ cm²/s and $b = 0.5 \times 10^{-4}$ s⁻¹. Solution is shown for \mathbf{v}_1 and S_1 (upper panel) and \mathbf{v}_2 (lower panel) at day 10. The shading scale for S_1 is the same as in Figure 21.



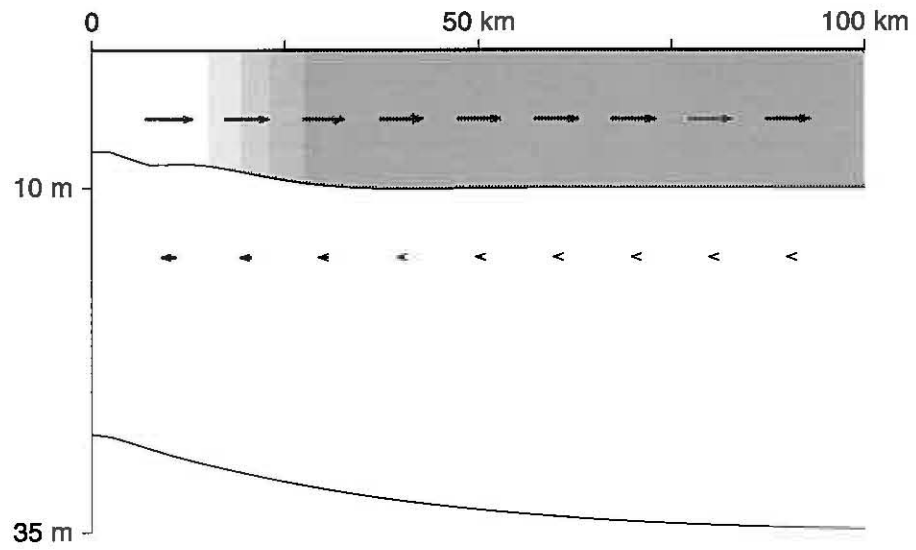
to that in many of the previous solutions (for example, in Figure 8 and 21). At this time, a plume has developed near the river mouth with more fresher water concentrated on the upstream coast (upper panel). In the lower layer (lower panel), water is drawn from all the directions into the estuary, but mostly from the downstream coast.

With the forcing by an upwelling-favorable alongshore wind, an offshore Ekman flow, $u_e = \tau^y/fH_1 = 6.3$ cm/s, is generated in the upper layer. As a result, the upper interface is raised in the nearshore region. The rate at which it is raised can be estimated as $H_1 u_e/R_2$, where R_2 is the Rossby radius associated with the second vertical mode, which is $c_2/f = 7.25$ km (see the value of c_2 and discussion of vertical modes in Appendix B). Using the above values, the value is 0.9×10^{-2} cm/s, implying that it takes only 0.3 days for h_1 to become less than H_e (7.5 m). From then on, entrainment ensures that h_1 remains greater than h_e , as required by equation (5). Figure 27 shows the transverse circulation at $y = 200$ km, a location south of the river mouth where there is no river water at all. As can be seen, a salinity (density) front forms in the upper layer due to the entrainment, and the front advances offshore at a speed consistent with that of the Ekman drift. To avoid confusion, note that this density front exists between the upper-layer ambient water and the entrained lower-layer water, so that it has nothing to do with the river plume. Also note that h_2 continuously thins at the coast; eventually it will become zero there, and the calculation must stop.

A plan view of \mathbf{v}_1 and S_1 is shown in Figure 28 after 15 (upper panel) and 20 days (middle panel), and \mathbf{v}_2 and S_2 (lower panel) at day 20. The upper-layer flow features offshore Ekman flow in the far field. The alongshore flow in the nearshore region is the result of the geostrophic response to the landward decrease of pressure due to offshore Ekman flow. A band of strong alongshore flow develops within the migrating density front; it is caused by the pressure gradient associated with the density front [see equation (10a)]. The river plume is pushed offshore and elongated northward (shaded region). Such a solution is much like the situation during the Mississippi-River flood in 1993 (Walker *et al.*, 1994), when river water flowed eastward along the continental shelf and eventually reached the Florida Strait. In the lower layer, water also flows generally northward, a geostrophic response to the decrease of pressure in the nearshore region. The onshore component to \mathbf{v}_2 results from bottom drag.

Figure 27: Transverse circulation and salinity along a section at day 15 (upper panel) and 20 (lower panel) under an upwelling-favorable wind of $\tau^y = 0.5 \text{ dyn/cm}^2$, which started at day 10 corresponding to the situation shown in Figure 26. The section is taken at $y = 200 \text{ km}$, where no plume is found. Unlike the shading scale for S_1 in Figure 26, the dark-shaded region indicates the initial upper layer water with salinity $S_1^* = 30$, while the unshaded region represents initial lower layer water of salinity $S_2^* = 35$. Due to entrainment, a density front formed in the upper layer, and it migrates offshore at the speed consistent with the Ekman drift.

Day 15



Day 20

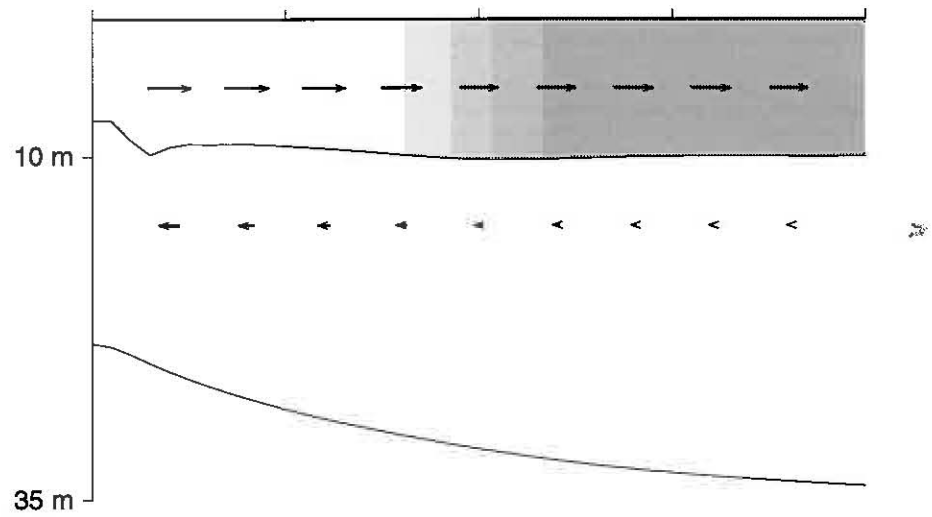
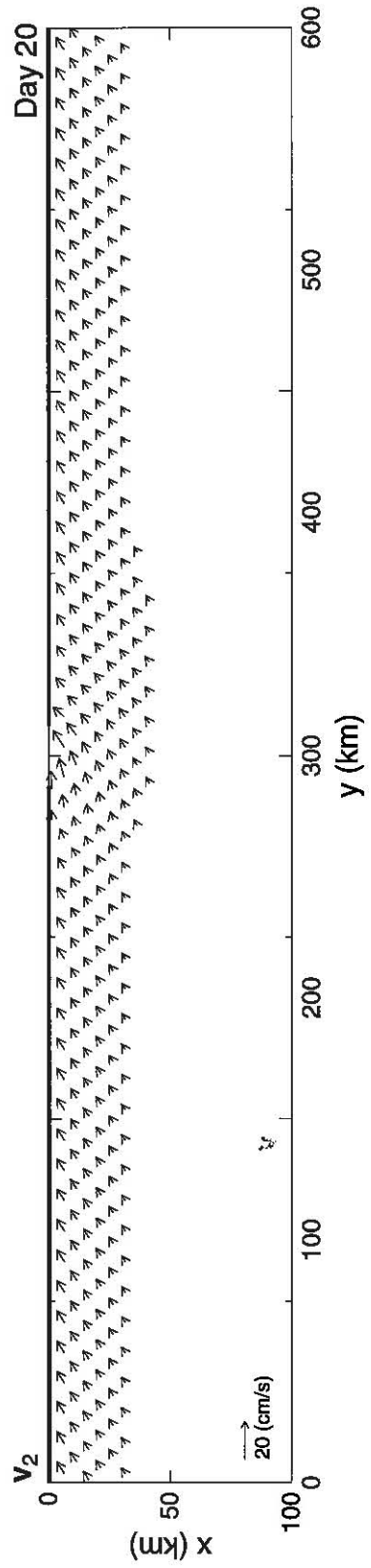
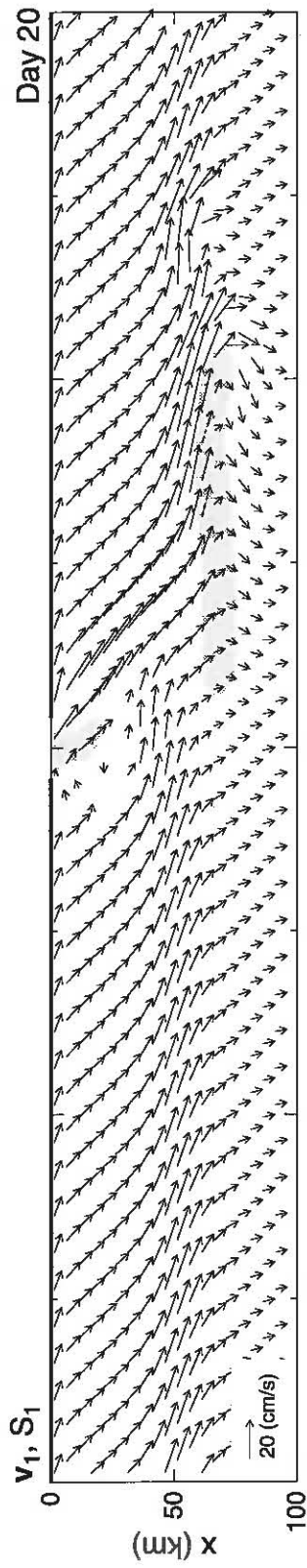
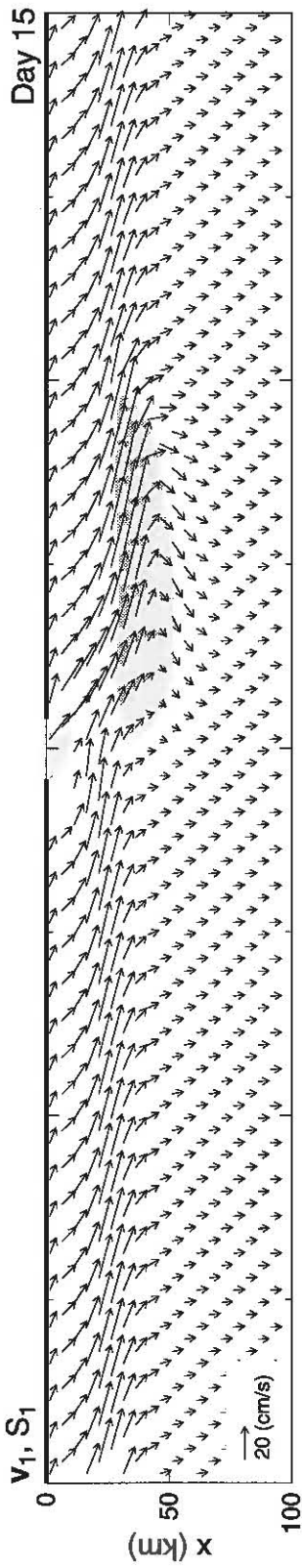


Figure 28: Plane view of the solution in Figure 27, showing velocity \mathbf{v}_1 and salinity S_1 at day 15 (upper panel) and 20 (middle panel) and velocity \mathbf{v}_2 at day 20 (lower panel). The shading scale for S_1 is the same as in Figure 26. Note that river plume is much salty due to the mixing with the entrained lower layer water of salinity S_1^* .



The situation is drastically different under forcing by downwelling-favorable wind (Figure 29). In this case, the transverse circulation reverses because an onshore Ekman flow is generated in the upper layer. As a result, a density front forms in the lower layer and migrates offshore. In the upper layer, water generally flows southward, and the plume is pushed against the coast and downstream (upper and middle panel of Figure 30). In the lower layer, the flow is downstream and offshore (lower panel of Figure 30). Such a solution is similar to the Changjiang River plume during winter (lower panel of Figure 2).

Figure 29: Similar to Figure 27, except for an across-shore section at $y = 350$ km under downwelling-favorable wind $\tau^y = -0.5$ dyn/cm². A density front forms in the lower layer and migrates offshore.

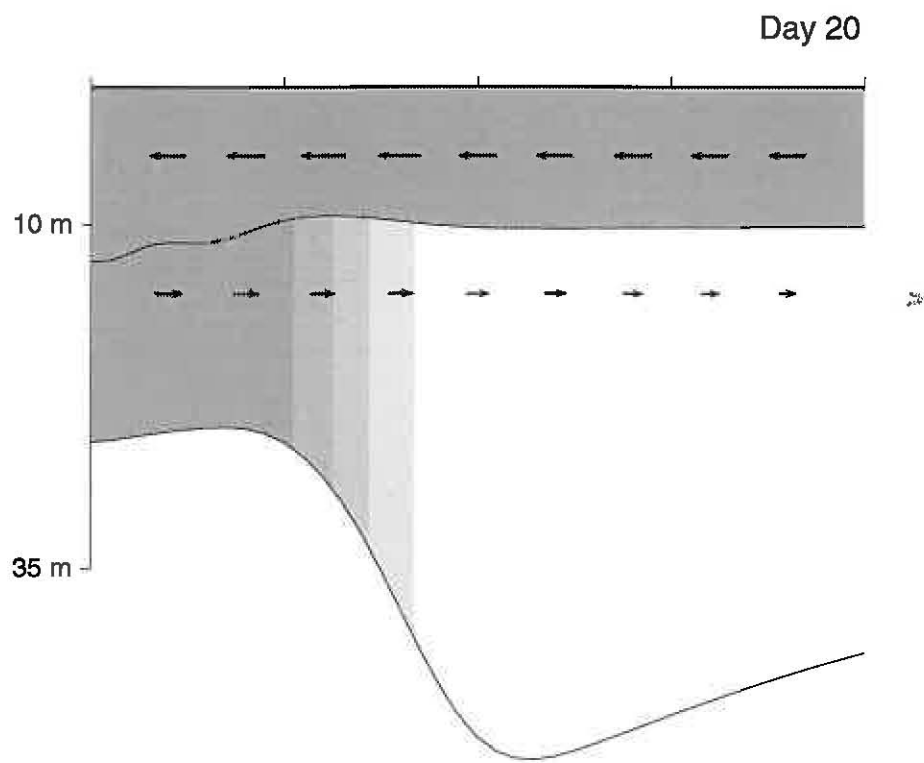
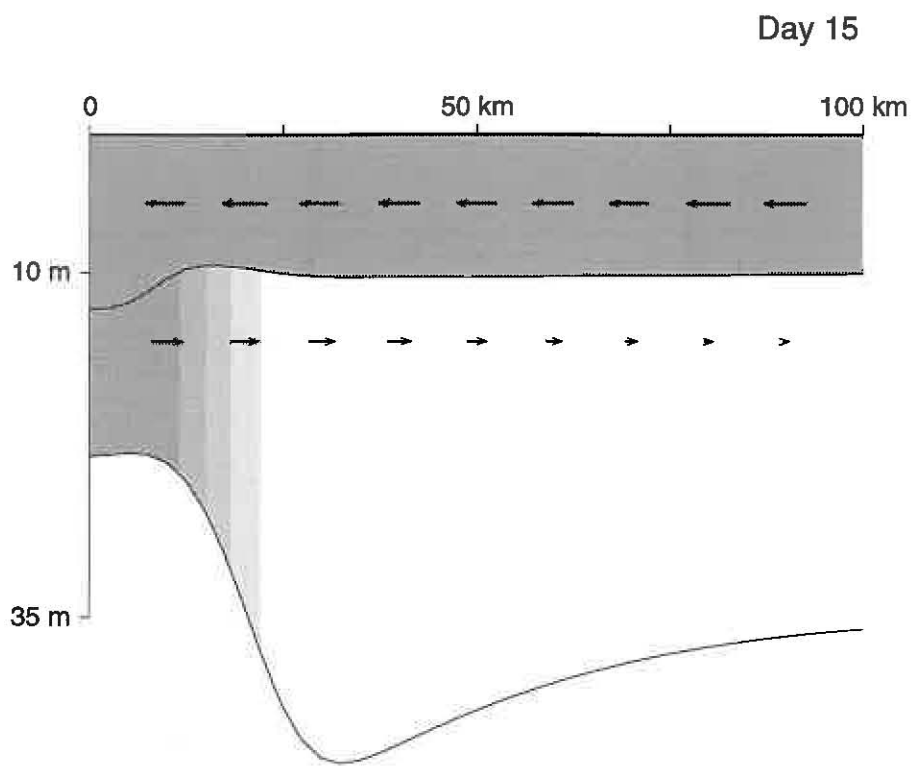
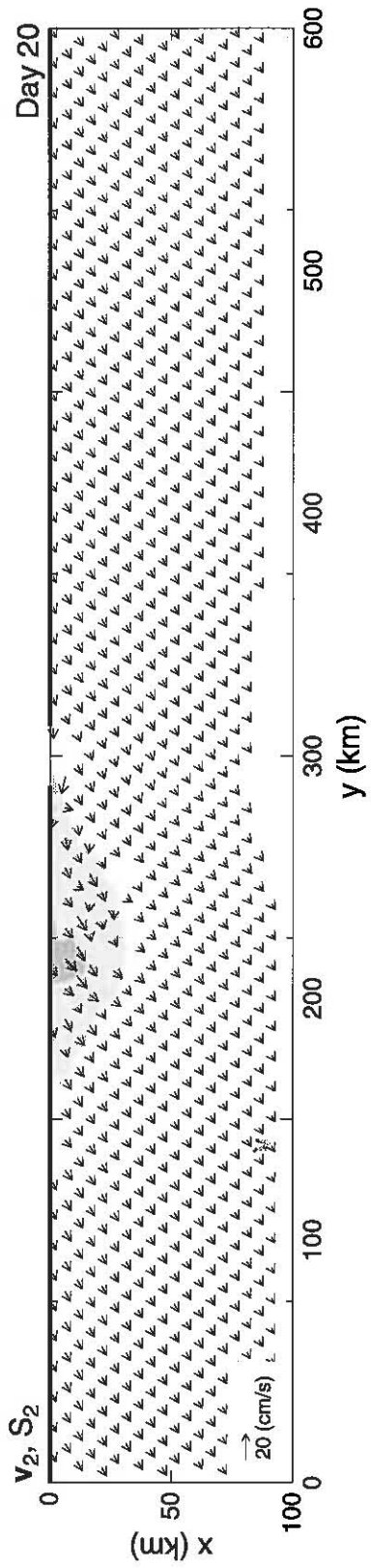
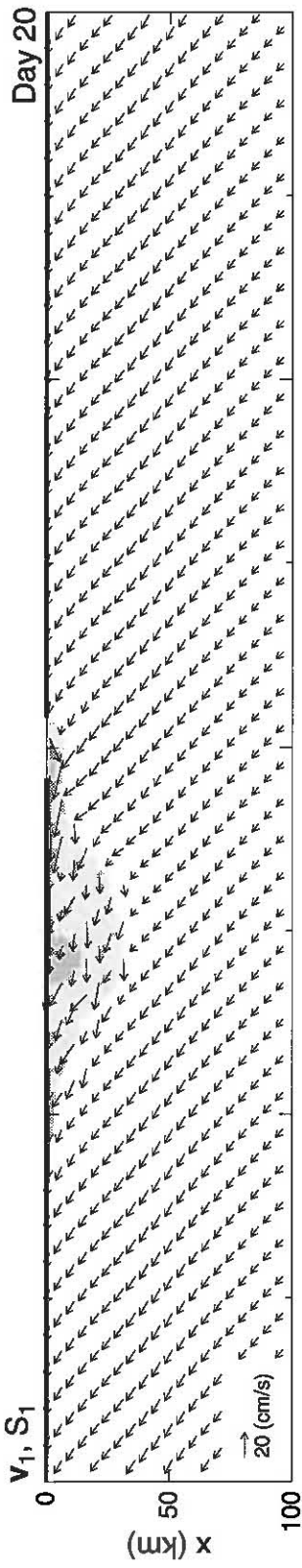
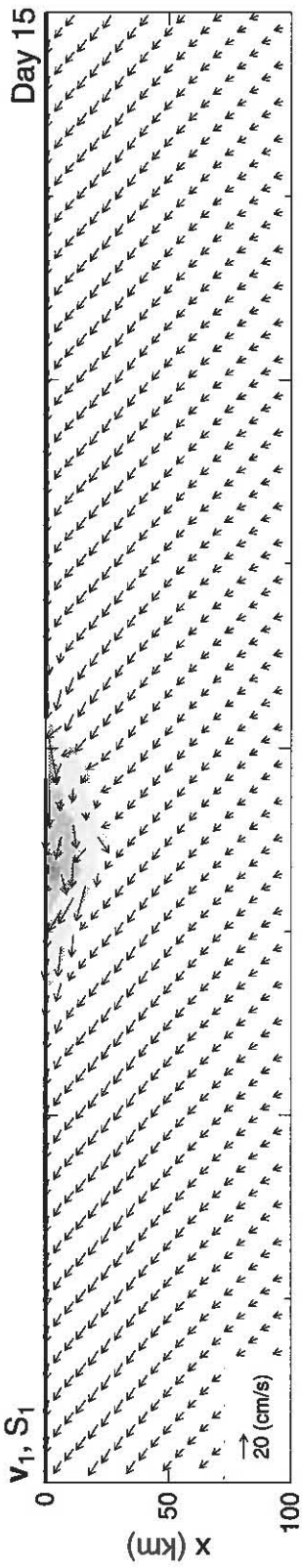


Figure 30: Plane view of the solution in Figure 29, showing \mathbf{v}_1 and S_1 at day 15 (upper panel) and 20 (middle panel), and \mathbf{v}_2 and S_2 at day 20 (lower panel). Shading scales for S_1 and S_2 are the same as in Figure 26.



CHAPTER 6

SUMMARY AND DISCUSSION

In this study, variable-density, $1\frac{1}{2}$ - and $2\frac{1}{2}$ -layer models have been used to examine the behavior of plumes formed by discharging fresher water of transport M_r and salinity S_r from a river mouth into a pre-existing, upper layer (oceanic mixed layer) of initial layer thickness H_1 and salinity $S_1^* > S_r$. The river mouth is always located somewhere along the western boundary of a north-south f -plane channel basin. Solutions exhibit a variety of features depending on conditions of both the river outflow (M_r, S_r) and the oceanic mixed layer (H_1, S_1^*). Pre-existing background currents and forcing by wind stress also affect their behavior significantly. A particularly interesting property is that in most solutions part of the plume moved upstream (northward) without external forcing. Much of the effort of this research was focused on the mechanisms that cause this feature.

In Chapter 3, properties of geostrophy adjustment in the variable-density, $1\frac{1}{2}$ -layer model are investigated. This investigation provides dynamical insights into circulations^{*} driven by horizontal variations of density, and currents driven in this way are an important component of river-outflow-driven solutions discussed in Chapter 4. Specifically, the adjustment to an initially unbalanced y -independent density front generates a frontally-trapped current flowing in the direction with the fresher water to its right. Such a solution is found to be very similar to the one that results from an initial disturbance in layer thickness (*i.e.*, potential vorticity) in a constant-density model. The quantitative relation between salinity anomaly and potential vorticity anomaly in a linear system is found to be $\tilde{g}'_1/g'_0 = -2\tilde{q}_1^*/f$.

In Chapter 4, circulations driven only by river outflow in the $1\frac{1}{2}$ -layer model are discussed.

Properties of solutions in low Rossby number (R_o) regime differ fundamentally from those in high- R_o regime. In the low- R_o regime, the prominent feature of solutions is that the plume advances along both upstream and downstream coasts and expands offshore. If M_r is less than a critical value M_{cr} [see equation (53)] determined by H_1 and $\Delta S = (S_1^* - S_r)$, the offshore expansion eventually stops, and a quasi-equilibrium state is reached. In this quasi-equilibrium state, all the river water first turns northward to flow along the upstream coast, and some of it, together with some ambient sea water, reverses direction near the upstream plume nose to flow southward along the front between the plume and oceanic water. This return flow passes the river mouth and continues to flow along the downstream coast (see Figure 12). In contrast, when M_r is greater than M_{cr} , the plume expands offshore forever and some river water must turn to flow directly southward at the river mouth.

Several dynamical investigations help to reveal the mechanisms that cause upstream plume propagation. In Section 4.1.2, it was demonstrated that the circulation can be split into two distinct parts: a coastal mode and a gyre mode. The coastal mode is a southward-flowing downstream coastal current induced only by the mass input of the outflow and is responsible for the plume to move downstream; the gyre mode is an anticyclonic gyre due to the response to the high pressure associated with the plume, and it is the northward current of this gyre that moves the plume upstream. In Section 4.1.3, it was shown further in a hierarchy of analytic solutions that the geostrophic adjustment generates the return flow along the plume front and that Kelvin waves originating from the plume nose causes the northward coastal current by thinning h_1 near the coast. The upstream motion can also be explained alternatively by appealing to mass conservation of salty and fresher waters: the return flow drains some oceanic water from the upstream region, and hence fresher water *must* move northward to replace it by continuity [see the discussions of equation (56)].

In the high- R_o regime, momentum advection causes river water to flow directly offshore in a narrow jet. The angle at which the jet emerges from the mouth is largely determined by two competing factors: the ability of river water to flow upstream due to the gyre mode and the ability to flow downstream due to the coastal mode. Equation (63) provides a formula which determines the angle in terms of model parameters. The agreement with the numerical results are impressive, but the explanation is still some what empirical. The

underlying dynamics of this result deserve further attention.

When entrainment is included, the upstream propagation is significantly inhibited. This happens because: *i*) the entrainment prevents the shallowing of h_1 near the plume nose, thereby preventing the northward coastal current from being established via Kelvin-wave radiation; and *ii*) it decreases the density variation between the plume and the oceanic water, and hence the strength of plume-driven circulation. In addition, inclusion of entrainment makes the distinction between low- and high- R_o solutions impossible because the entrainment prevents the formation of jet in the latter case.

In Chapter 5, a $2\frac{1}{2}$ -layer model is used to examine the influences of lower-layer inflow into the estuary, a background current V_b , and forcing by alongshore winds. The lower-layer inflow hardly changes the upper-layer response from its $1\frac{1}{2}$ -layer counterpart (compare Figures 21 and 22a with Figures 8 and 10). In the lower layer, it generates flows that generally are directed opposite to the upper-layer currents, owing to the dominant response of the second baroclinic mode. A pre-existing downstream coastal current tends to enhance the downstream motion and to inhibit the upstream motion. In fact, the upstream flow can be completely stopped if V_b is strong enough (see the discussion of lower panel of Figure 24). An upwelling-favorable wind generates a coastal circulation that advects the plume offshore and northward, whereas a downwelling-favorable wind traps it to the coast and advects it southward.

Our solutions have a number of features in common with those in other models. For example, our low- R_o solutions to the $1\frac{1}{2}$ -layer model are similar to Kubokawa's (1991) quasi-geostrophic solution. The dynamical link between them is revealed by equation (22) in which a low salinity (high \tilde{g}'_1) in our variable-density model is demonstrated to be analogous to low potential vorticity in his model. In fact, the governing equation for the plume evolution in our solutions [equation (41d)] has the same form as his does [his equation (2.12)]. Moreover, our non-dimensional transport ϕ (M_r/M_{cr}) is equivalent to his P/h_0 , with our solution for $\phi < 1$ corresponding to his solution for $(P/h_0)^{-1} < 1$, and vice versa (see his Figure 5). The similarity between our solution and Kubokawa's is also shown by the following: when the outflow is assumed to have piece-wise structure in salinity with only the right-hand portion being fresher water but the left-hand portion being as salty as the ambient sea

water, solutions do exist in which all the fresher water flows downstream, consistent with his solutions. In contrast to Kubokawa's solutions, our low- R_o solutions are not sensitive to the outflow structure at the river mouth (see the discussion at the end of Section 4.1.4).

The similarity between our low- R_o solutions and those in Chapman and Lentz's (1994) study suggests that they share some common dynamics. For example, in their model an increase in $\Delta\rho$ enhances the upstream motion (see their Figure 9), a feature consistent with our solutions. Likewise, our high- R_o solutions have features in common with those in some GCM solutions. For example, plumes in solutions reported by Chao and Boicourt (1986; their Figure 6) and by Kourafalou *et al.* (1996; their Figure 2) have large offshore bulges near the river mouth; however, they do not exhibit a distinct offshore jet, possibly because the vertical mixing in GCMs inhibits its formation.

Observed plumes typically flow predominantly downstream or spread offshore, and there is little direct evidence for internally generated upstream propagation of the sort present in our low- R_o solutions. A number of factors can inhibit upstream propagation in the real ocean. For example, the interaction between the river water and the ambient sea water may result in a slanted, rather than a vertically-oriented, density front; this may cause weaker upstream plume propagation because the alongfront geostrophic adjustment in this case involves weaker salty-water flow (see Section 4.1.5 and Appendix A). In addition, if there is no oceanic mixed layer, corresponding to $H_1 = 0$ in our model, $M_{cr} = 0$ [equation (53)], indicating that river water should not go upstream at all. Finally, other factors such as the vertical mixing, downstream background currents and downwelling-favorable winds also tend to inhibit the upstream motion. On the other hand, our high- R_o solutions have features in common with observed outflow circulations (for example, compare the upper panel of Figure 2 with the top panel of Figure 15), suggesting that this is the most realistic dynamical regime for our model.

APPENDIX A

SOLUTION WITH A SLANTED FRONT

Here, solutions are obtained of geostrophic adjustment to a y -independent density front, analogous to the analytic solution in Section 3.2, except that the density front is allowed to slant. The upper panel of Figure 7a illustrates the final structure of the front. Because the front is slanted, there are three distinct regions: fresher-water ($x < \varepsilon_-$) and salty-water ($x \geq \varepsilon_+$) regions where the system is like a $1\frac{1}{2}$ -layer model, and a middle region where fresher water overlies salty water ($\varepsilon_- \leq x < \varepsilon_+$) like a $2\frac{1}{2}$ -layer model. Our method of solution is an extension of the one discussed by Stommel and Veronis (1980), who considered the geostrophic adjustment of a y -independent front in a 2-layer model.

In the fresher-water and salty-water regions, the governing equations simplify to equations (23). In the middle region, the model is essentially a $2\frac{1}{2}$ -layer system, in which the pressures are

$$p_- = g'_- h_- + g'_+ h_+, \quad p_+ = g'_+(h_- + h_+). \quad (\text{A1})$$

Potential-vorticity conservation and geostrophy then yield equations for h_- and h_+ that are coupled together, resulting in the fourth-order equation

$$(1 - \gamma^2)R_-^2 R_+^2 (h_j)_{xxxx} - (R_-^2 + R_+^2) (h_j)_{xx} + h_j = H_1. \quad (\text{A2})$$

for either h_- or h_+ .

The general solution in the fresher-water region is

$$h_- = H_1 + Ae^{(x-\varepsilon_-)/R_-}, \quad (\text{A3})$$

since the term that grows in x must be discarded. Similarly, in the salty-water region, it is

$$h_+ = H_1 + B e^{-(x-\varepsilon_+)/R_+}. \quad (\text{A4})$$

In the middle region, the general solution to equation (A2) for h_- can be written

$$h_- = H_1 + C \sinh \xi_+ + D \cosh \xi_+ + E \sinh \xi_- + F \cosh \xi_-, \quad (\text{A5})$$

where $\xi_{\pm} = \alpha_{\pm} x$, and

$$\alpha_{\pm} = \left(\frac{R_-^2 + R_+^2 \pm \sqrt{(R_-^2 + R_+^2)^2 - 4(1 - \gamma^2)R_-^2 R_+^2}}{2(1 - \gamma^2)R_-^2 R_+^2} \right)^{\frac{1}{2}}. \quad (\text{A6})$$

Similarly, the general solution for h_+ is

$$h_+ = H_1 + S_+(C \sinh \xi_+ + D \cosh \xi_+) + S_-(E \sinh \xi_- + F \cosh \xi_-), \quad (\text{A7})$$

where $S_j = 1 - (R_-^2 - R_+^2)\alpha_j^2$.

There are total of 8 constants to be determined, namely, $A-F$, ε_- and ε_+ . The matching conditions

$$h_+ = 0, \quad h_- \text{ and } v_- \text{ are continuous} \quad @ \quad x = \varepsilon_-, \quad (\text{A8a})$$

$$h_- = 0, \quad h_+ \text{ and } v_+ \text{ are continuous} \quad @ \quad x = \varepsilon_+, \quad (\text{A8b})$$

$$\text{Mass is conserved for both fresher and salty water.} \quad (\text{A8c})$$

provide the 8 constraints needed to find them. To solve for these unknowns, an initial value of ε_+ is given, and then the system can be reduced to a set of 5 linear algebra equations in four unknowns, and any of 4 equations can be used to find them. However, their results may not satisfy the 5th equation unless the initial value of ε_+ is a solution. By guessing ε_+ iteratively, this 5th equation will be eventually satisfied and then the solutions for the four unknowns are found. Finally, the remaining three can be represented by the 5 determined unknowns.

APPENDIX B

VERTICAL MODES

Consider a linear, constant-density, $2\frac{1}{2}$ -layer system which can be driven either by mass input and output near the river mouth in the upper and lower layer, respectively, or by a prescribed initial pressure field. The equations are

$$u_{it} - fv_i + \frac{1}{\rho_i} p_{ix} = 0, \quad (\text{B1a})$$

$$v_{it} + fu_i + \frac{1}{\rho_i} p_{iy} = 0, \quad (\text{B1b})$$

$$h_{it} + H_i(u_{ix} + v_{iy}) = 0, \quad (\text{B1c})$$

where subscript $i = 1, 2$ is the layer index. The relation between h_i and p_i can be expressed as

$$h_1 = \frac{1}{g\Delta\rho_{21}} \left(\frac{\rho_2}{\rho_1} p_1 - p_2 \right) + H_1, \quad (\text{B2a})$$

$$h_2 = \frac{1}{g\Delta\rho_{21}} \left(-p_1 + \frac{\Delta\rho_{31}}{\Delta\rho_{32}} p_2 \right) + H_2, \quad (\text{B2b})$$

where $\Delta\rho_{21}$, $\Delta\rho_{31}$ and $\Delta\rho_{32}$ are density differences between layers as the subscripts indicate. With the replacement of h_1 , h_2 in (B1) by (B2), equation (B1) becomes a coupled set of equations in u_i , v_i and p_i .

Let q be u , v or p . Then, variables q_1 and q_2 can be decomposed into 2 vertical modes according to

$$\begin{pmatrix} q_1 \\ q_2 \end{pmatrix} = q^1 \psi_1 + q^2 \psi_2, \quad (\text{B3})$$

where ψ_1 and ψ_2 define the mode structures, and q^1 and q^2 are their corresponding amplitudes. The mode structures are the eigenfunctions of the matrix

$$A = \begin{pmatrix} a_{11} & a_{12} \\ a_{21} & a_{22} \end{pmatrix} = \begin{pmatrix} \frac{1}{gH_1\Delta\rho_{21}} \frac{\rho_2}{\rho_1} & -\frac{1}{gH_1\Delta\rho_{21}} \\ -\frac{1}{gH_2\Delta\rho_{21}} & \frac{1}{gH_2\Delta\rho_{21}} \frac{\Delta\rho_{31}}{\Delta\rho_{32}} \end{pmatrix}, \quad (\text{B4})$$

yielding

$$\psi_n = \begin{pmatrix} 1 \\ \frac{\lambda_n - a_{11}}{a_{12}} \end{pmatrix}, \quad (\text{B5})$$

where $n = 1, 2$ is a mode index. In the above, λ_n is the eigenvalue and defined as

$$\lambda_n = \frac{1}{2} \left(a_{11} + a_{22} \mp \sqrt{(a_{11} - a_{22})^2 + 4a_{12}a_{21}} \right), \quad (\text{B6})$$

with $n = 1$ corresponding to the minus sign for the term with square root. The eigenvalue λ_n is often written in the alternate form $c_n = \lambda_n^{-1/2}$, which has unit of velocity and is referred to as the characteristic speed for each mode. Equations for the amplitudes, denoted by superscript n , are

$$u_t^n - fv^n + p_x^n = 0, \quad (\text{B7a})$$

$$v_t^n + fu^n + p_y^n = 0, \quad (\text{B7b})$$

$$\frac{1}{c_n^2} p_t^n + u_x^n + v_y^n = 0, \quad (\text{B7c})$$

which have the same form as the linear, shallow-water equation.

Using the parameters in Table 1, the two characteristic speeds are $c_1 = 107$ cm/s and $c_2 = 58$ cm/s. The corresponding eigenfunctions are

$$\psi_1 = \begin{pmatrix} 1 \\ 0.45 \end{pmatrix}, \quad \psi_2 = \begin{pmatrix} 1 \\ -0.89 \end{pmatrix}, \quad (\text{B8})$$

which indicate that flows are in the same direction in both layers for the first mode, whereas they are oppositely directed for the second mode.

REFERENCES

- Arakawa, A. and V. R. Lamb, 1977. Computational design of the basic dynamic processes of the UCLA general circulation model. *Methods in Comp. Phys.*, **17**, J. Chang, Ed., Academic Press, 173-265.
- Arakawa, A. and V. R. Lamb, 1981. A potential enstrophy and energy conserving scheme for the shallow water equations. *Mon. Wea. Rev.*, **109**, 18-36.
- Beardsley, R. C. and J. Hart, 1978. A simple theoretical model for the flow of an estuary onto a continental shelf. *J. Geophys. Res.*, **83**, 873-883.
- Beardsley, R. C., R. Limeburner, D. Hu, K. Le, G. A. Cannon and D. J. Pashinski, 1983. Structure of the Changjiang plume in the East China Sea during June 1980. In: *Proceedings of the International Symposium on Sedimentation on the Continental Shelf with Special Reference to the East China Sea, April 12-16, 1983, Hangzhou, China*. Vol. 1, China Ocean Press, Beijing, pp. 265-284.
- Bleck, R., H. Y. Hanson, D. Hu and E. B. Kraus, 1989. Mixed layer/thermocline interaction in a three dimensional isopycnal model, 1989. *J. Phys. Oceanogr.*, **19**, 1417-1439.
- Boicourt, W. C., 1981. Circulation in the Chesapeake Bay entrance region: Estuary-shelf interaction. In: *Chesapeake Bay plume study, Superflux 1980*, NASA CP-2188, 61-78.
- Bumpus, D. F., 1973. A description of the circulation on the continental shelf of east coast of the United States. *Prog. Oceanogr.*, **6**, 111-159.
- Cannon, G. A., D. J. Pashinski and R. Dong, 1983. Circulation in the Changjiang entrance region: estuary-shelf interactions. In: *Proceedings of the International Symposium on Sedimentation on the Continental Shelf with Special Reference to the East China Sea, April 12-16, 1983, Hangzhou, China*. Vol. 1, China Ocean Press, Beijing, pp. 302-310.
- Chao, S. Y. and W. C. Boicourt, 1986. Onset of estuarine plumes. *J. Phys. Oceanogr.*, **16**, 2137-2149.
- Chao, S. Y., 1988a. River-forced estuarine plume. *J. Phys. Oceanogr.*, **18**, 72-88.
- Chao, S. Y., 1988b. Wind-driven motion of estuarine plumes. *J. Phys. Oceanogr.*, **18**, 1144-1166.
- Chapman, D. C. and S. J. Lentz, 1994. Trapping of a coastal density front by bottom boundary layer. *J. Phys. Oceanogr.*, **24**, 1464-1479.

- Chen, D., L. M. Rothstein and A. J. Busalacchi, 1994. A hybrid vertical mixing scheme and its application to tropical ocean models. *J. Phys. Oceanogr.*, **24**, 2156–2179.
- Csanady, G. T., 1978. The arrested topographic waves. *J. Phys. Oceanogr.*, **8**, 47–62.
- de Szoeke, R. A. and J. G. Richman, 1984. On wind-driven mixed layers with strong horizontal gradients — A theory with applications to coastal upwelling. *J. Phys. Oceanogr.*, **14**, 364–377.
- Fukamachi, Y., J. P. McCreary, and J. A. Proehl., 1995. Instability of density fronts in layered and continuously stratified models. *J. Geophys. Res.*, **100**, 2559–2577.
- Garvine, R. W., 1987. Estuary plumes and fronts in shelf waters: a layer model. *J. Phys. Oceanogr.*, **17**, 1877–1896.
- Garvine, R. W., 1991. Subtidal frequency estuary-shelf interaction: observations near the Delaware Bay. *J. Geophys. Res.*, **96**, 7049–7064.
- Gill, A. E., 1982. Ocean-atmosphere dynamics. Academic press.
- Glendening, J. W., 1993. Nonlinear displacement of the geostrophic velocity jet created by mass imbalance. *J. Atmos. Sci.*, **50**, 1817–1628.
- Hermann, A. J., P. B. Rhines and E. R. Johnson, 1989. Nonlinear Rossby adjustment in a channel: Beyond Kelvin waves. *J. Fluid Mech.*, **205**, 469–502.
- Ikeda, M., 1984. Coastal flows driven by a local density flux. *J. Geophys. Res.*, **89**, 8008–8016.
- Kourafalou, V. H., L.-Y. Oey, J. D. Wang and T. N. Lee, 1996. The fate of river discharge on the continental shelf: 1. Modeling the river plume and the inner shelf coastal current. *J. Geophys. Res.*, **101**, 3415–3434.
- Kubokawa, A., 1991. On the behavior of outflows with low potential vorticity from a sea strait. *Tellus*, **43A**, 168–176.
- Kundu, P. and J. P. McCreary, Jr., 1986. On the dynamics of the throughflow from the Pacific into the India Ocean. *J. Phys. Oceanogr.*, **16**, 2191–2198.
- Limeburner, R. and R. C. Beardsley, 1982. Hydrographic data obtained in the East China Sea, August, 1981. Woods Hole Oceanogr. Inst. Tech. Rep. No. WHOI-82-39.
- Masse, A. K., 1990. Withdrawal of shelf water into an estuary: a barotropic model. *J. Geophys. Res.*, **95**, 16,085–16,096.

- McCreary, J. P. and P. K. Kundu, 1989. A numerical investigation of the sea surface temperature variability in the Arabian Sea. *J. Geophys. Res.*, **94**, 16,097–16,114.
- McCreary, J. P., S. Zhang and S. R. Shetye. Coastal circulation driven by river outflow in a variable-density $1\frac{1}{2}$ -layer model. Submitted to *J. Geophys. Res.*.
- Minato, S., 1983. Geostrophic response near the coast. *J. Oceanogr. Soc. Japan*, **39**, 141–149.
- Münchow, A. and R. W. Garvine, 1993. Buoyancy and wind forcing of a coastal current. *J. Mar. Res.*, **51**, 293–322.
- Murty, V. S. N., Y. V. B. Sarma, D. P. Rao and C. S. Murty, 1992. Water characteristics, mixing and circulation in the Bay of Bengal during southwest monsoon. *J. Mar. Res.*, **50**, 207–228.
- Nof, D., 1978. On geostrophic adjustment in sea straits and wide estuaries: Theory and laboratory experiments. Part II — Two-layer system. *J. Phys. Oceanogr.*, **8**, 861–872.
- Nocross, J. J. and E. M. Stanley, 1967. Inferred surface and bottom drift. June, 1963 through October, 1964, Prof. Pap. 3(2) Env. Sci. Serv. Admin., Washington, D.C.
- O'Donnell, J., 1990. The formation and fate of a river plume: A numerical model. *J. Phys. Oceanogr.*, **20**, 551–569.
- Pape, E. H., III, and R. W. Garvine, 1982. The subtidal circulation in Delaware Bay and adjacent shelf waters. *J. Geophys. Res.*, **87**, 7955–7970.
- Qin, Y., Y. Zhao, L. Chen and S. Zhao, 1990. Submarine sediments and sedimentation. In: *Geology of Bohai Sea*. China Ocean Press, Beijing, pp. 79–121.
- Schopf, P. S. and M. A. Cane, 1983. On equatorial dynamics, mixed layer physics and sea surface temperature. *J. Phys. Oceanogr.*, **13**, 917–938.
- Schopf, P. S. and A. Loughe, 1995. A reduced gravity isopycnal model: hindcasts of El Niño. *Mon. Wea. Rev.*, **123**, 2839–2863.
- Shetye, S. R., A. D. Gouveia, S. S. C. Shenoi, D. Sundar, G. S. Michael and G. Nampoothiri, 1993. The western boundary current of the seasonal subtropical gyre in the Bay of Bengal. *J. Geophys. Res.*, **98**, 945–954.
- Stommel, H. and G. Veronis, 1980. Barotropic response to cooling. *J. Geophys. Res.*, **85**, 6661–6666.

- Walker, N. D., G. S. Fargion, L. J. Rouse and D. C. Biggs, 1994. The great flood of summer 1993: Mississippi River discharge studied. *Trans. Amer. Geo. Union*, **75**, No. 36.
- Wang, W., 1988. Yangtze brackish water plume—circulation and diffusion. *Prog. Oceanogr.*, **21**, 373–385.
- Young, W. R., 1994. The subinertial mixed layer approximation. *J. Phys. Oceanogr.*, **24**, 1812–1826.
- Zhang, Q., G. S. Janowitz and L. T. Pietrafesa, 1987. The interaction of estuarine and shelf waters: A model and applications. *J. Phys. Oceanogr.*, **17**, 455–469.